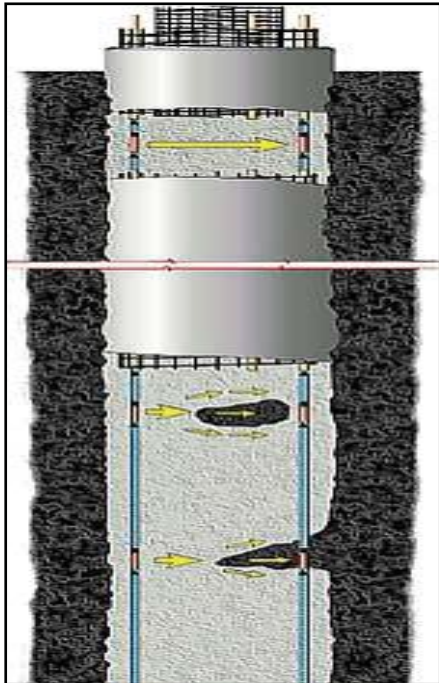


DRILLED SHAFT AXIAL CAPACITY

Effects Due to Anomalies

Publication No. FHWA-CFL/TD-08-008

September 2008



U.S. Department
of Transportation
**Federal Highway
Administration**



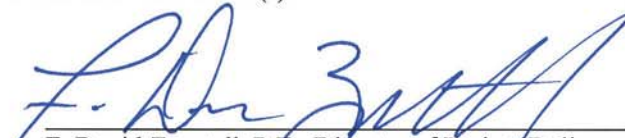
Central Federal Lands Highway Division
12300 West Dakota Avenue
Lakewood, CO 80228

FOREWORD

The Federal Lands Highway (FLH) of the Federal Highway Administration (FHWA) promotes development and deployment of applied research and technology applicable to solving transportation related issues on Federal Lands. The FLH provides technology delivery, innovative solutions, recommended best practices, and related information and knowledge sharing to Federal agencies, Tribal governments, and other offices within the FHWA.

The objective of this study was to produce guidelines for assessing the importance of defects on the drilled shaft capacity in different soils and also priority for remediation effort. The study included a literature search on earlier research, enhancement of a finite element code, PSI for use in this study, results of a comprehensive finite element analysis program with varying factors including defect location and sizes, soil types, and concrete strength. The following are the recommendations for the remediation guidelines:

- A proper construction quality monitoring program including sonic wave survey, tomographic imaging, and temperature, moisture, and density measurements are recommended for all critical drilled shafts,
- Once defects are located remediation measures must be implemented to fill the defect voids with concrete,
- If prioritization is necessary in fixing the defects, the shallow, non-concentric defects must receive first attention because of its experience of a higher pile loads than a deeper defects,
- The effects of soil types and strengths must be properly assessed from the pile load transfer and structural capacity curves to assess the critical nature of a defect(s).



F. David Zanetell, P.E., Director of Project Delivery
Federal Highway Administration
Central Federal Lands Highway Division

Notice

This document is disseminated under the sponsorship of the U.S. Department of Transportation in the interest of information exchange. The U.S. Government assumes no liability for the use of the information contained in this document. This report does not constitute a standard, specification, or regulation.

The U.S. Government does not endorse products or manufacturers. Trademarks or manufacturers' names appear in this report only because they are considered essential to the objective of the document.

Quality Assurance Statement

The FHWA provides high-quality information to serve Government, industry, and the public in a manner that promotes public understanding. Standards and policies are used to ensure and maximize the quality, objectivity, utility, and integrity of its information. FHWA periodically reviews quality issues and adjusts its programs and processes to ensure continuous quality improvement.

Technical Report Documentation Page

1. Report No. FHWA-CFL/TD-08-008	2. Government Accession No.	3. Recipient's Catalog No.	
4. Title and Subtitle <i>Drilled Shaft Axial Capacities Effects Due to Anomalies</i>		5. Report Date September 2008	
		6. Performing Organization Code	
7. Author(s) Nien-Yin Chang, Ph.D., P.E., Principal Investigator (P.I.) Hien Nghiem, Research Assistant (R.A.)		8. Performing Organization Report No. CGES 001-08	
9. Performing Organization Name and Address Center for Geotechnical Engineering Science, University of Colorado, Denver, 1200 Larimer Street, Denver, CO 80217-3364		10. Work Unit No. (TRAVIS)	
		11. Contract or Grant No. DTFH68-06-X-00033	
12. Sponsoring Agency Name and Address Federal Highway Administration Central Federal Lands Highway Division 12300 West Dakota Avenue, Suite 210 Lakewood, CO 80228		13. Type of Report and Period Covered Final Report August 2006 – April 2008	
		14. Sponsoring Agency Code HFTS-16.4	
15. Supplementary Notes COTR: Khamis Y. Haramy, FHWA-CFLHD. Advisory Panel Members: Roger Surdahl, FHWA-CFLHD; Scott Anderson and Barry Siel, FHWA-RC; and Matt Greer, FHWA-CO Division. This project was funded under the FHWA Federal Lands Highway Technology Deployment Initiatives and Partnership Program (TDIPP).			
16. Abstract Drilled shafts are increasingly being used in supporting critical structures, mainly because of their high-load supporting capacities, relatively low construction noise, and technological advancement in detecting drilled shaft anomalies created during construction. The critical importance of drilled shafts as foundations makes it mandatory to detect the size and location of anomalies and assess their potential effect on drilled shaft capacity. Numerical analysis was conducted using Pile-Soil Interaction (PSI), a finite element analysis program to assess the effect of different anomalies on the axial load capacities of drilled shafts in soils ranging from soft to extremely stiff clay and loose to very dense sand. The investigation included the affect of anomalies of various sizes and lengths on both structural and geotechnical capacities. The analysis results indicate that the drilled shaft capacity is affected by the size and location of the anomaly and the strength of the surrounding soil. Also, nonconcentric anomalies significantly decrease the structural capacity of a drilled shaft under axial load. The resulting drilled shaft capacity then equals the smaller one of the two capacities: structural or geotechnical.			
17. Key Words DRILLED SHAFTS, GEOTECHNICAL, STRUCTURAL, DRILLED SHAFT CAPACITIES, ANOMALIES, FINITE ELEMENT ANALYSIS, PSI		18. Distribution Statement No restriction. This document is available to the public from the sponsoring agency at their website http://www.cflhd.gov .	
19. Security Classif. (of this report) Unclassified	20. Security Classif. (of this page) Unclassified	21. No. of Pages 148	22. Price

SI* (MODERN METRIC) CONVERSION FACTORS

APPROXIMATE CONVERSIONS TO SI UNITS

Symbol	When You Know	Multiply By	To Find	Symbol
LENGTH				
in	inches	25.4	millimeters	mm
ft	feet	0.305	meters	m
yd	yards	0.914	meters	m
mi	miles	1.61	kilometers	km
AREA				
in ²	square inches	645.2	square millimeters	mm ²
ft ²	square feet	0.093	square meters	m ²
yd ²	square yard	0.836	square meters	m ²
ac	acres	0.405	hectares	ha
mi ²	square miles	2.59	square kilometers	km ²
VOLUME				
fl oz	fluid ounces	29.57	milliliters	mL
gal	gallons	3.785	liters	L
ft ³	cubic feet	0.028	cubic meters	m ³
yd ³	cubic yards	0.765	cubic meters	m ³
NOTE: volumes greater than 1000 L shall be shown in m ³				
MASS				
oz	ounces	28.35	grams	g
lb	pounds	0.454	kilograms	kg
T	short tons (2000 lb)	0.907	megagrams (or "metric ton")	Mg (or "t")
TEMPERATURE (exact degrees)				
°F	Fahrenheit	5 (F-32)/9 or (F-32)/1.8	Celsius	°C
ILLUMINATION				
fc	foot-candles	10.76	lux	lx
fl	foot-Lamberts	3.426	candela/m ²	cd/m ²
FORCE and PRESSURE or STRESS				
lbf	poundforce	4.45	newtons	N
lbf/in ²	poundforce per square inch	6.89	kilopascals	kPa

APPROXIMATE CONVERSIONS FROM SI UNITS

Symbol	When You Know	Multiply By	To Find	Symbol
LENGTH				
mm	millimeters	0.039	inches	in
m	meters	3.28	feet	ft
m	meters	1.09	yards	yd
km	kilometers	0.621	miles	mi
AREA				
mm ²	square millimeters	0.0016	square inches	in ²
m ²	square meters	10.764	square feet	ft ²
m ²	square meters	1.195	square yards	yd ²
ha	hectares	2.47	acres	ac
km ²	square kilometers	0.386	square miles	mi ²
VOLUME				
mL	milliliters	0.034	fluid ounces	fl oz
L	liters	0.264	gallons	gal
m ³	cubic meters	35.314	cubic feet	ft ³
m ³	cubic meters	1.307	cubic yards	yd ³
MASS				
g	grams	0.035	ounces	oz
kg	kilograms	2.202	pounds	lb
Mg (or "t")	megagrams (or "metric ton")	1.103	short tons (2000 lb)	T
TEMPERATURE (exact degrees)				
°C	Celsius	1.8C+32	Fahrenheit	°F
ILLUMINATION				
lx	lux	0.0929	foot-candles	fc
cd/m ²	candela/m ²	0.2919	foot-Lamberts	fl
FORCE and PRESSURE or STRESS				
N	newtons	0.225	poundforce	lbf
kPa	kilopascals	0.145	poundforce per square inch	lbf/in ²

*SI is the symbol for the International System of Units. Appropriate rounding should be made to comply with Section 4 of ASTM E380. (Revised March 2003)

TABLE OF CONTENTS

CHAPTER 1 - INTRODUCTION.....	1
CHAPTER 2 - LITERATURE REVIEW.....	3
2.1 LITERATURE REVIEW OF CAPACITY OF DRILLED SHAFTS WITH ANOMALIES	3
2.2. DESIGN METHOD FOR AXIAL CAPACITY.....	11
2.2.1 Design for axial capacity in cohesive soil.....	11
2.2.1.1 <i>Side resistance in cohesive soils</i>	11
2.2.1.2 <i>End bearing in cohesive soils</i>	13
2.2.2 Design for axial capacity in cohesionless soil	13
2.2.2.1 <i>Side resistance in cohesionless soil</i>	13
2.2.2.2 <i>End bearing in cohesionless soil</i>	18
2.3. LOAD TRANSFER CURVES	19
2.3.1 Theoretical load transfer curve	19
2.3.1.1 <i>Elasto-perfect plastic model</i>	19
2.3.1.2 <i>Hyperbolic mode</i>	20
2.3.1.3 <i>Determination of parameters for nonlinear spring</i>	22
2.3.1.3.1 Initial shear modulus.....	22
2.3.1.3.2 Spring stiffness.....	23
2.3.1.3.3 Ultimate force	24
2.3.2 Load transfer curves from field test studies.....	25
CHAPTER 3 - STRUCTURAL CAPACITY OF DRILLED SHAFTS.....	31
3.1 AXIAL LOAD	31
3.2 AXIAL LOAD AND BENDING MOMENT.....	31
CHAPTER 4 - PILE-SOIL INTERACTION (PSI) FINITE ELEMENT CODE.....	35
4.1 INTRODUCTION	35
4.2 FINITE ELEMENTS	35
4.3 ELASTO-PLASTIC RATE INTEGRATION OF DIFFERENTIAL PLASTIC MODELS.....	36
4.4 CONSTITUTIVE MODELS OF SOILS	37
4.4.1 Mohr-Coulomb Model.....	37
4.4.2 Cap Model.....	38
4.5 ELASTO-PERFECT PLASTIC MODEL FOR BAR ELEMENT.....	40
4.6 CONVERGENCE CRITERIA	40
4.7 PSI CALIBRATION AND VALIDATION	41
4.7.1 Case histories for calibration	41
4.7.2 Comparative study between PSI and LS-DYNA codes.....	49
CHAPTER 5 - CAPACITIES OF DRILLED SHAFTS WITH ANOMALIES.....	57
5.1. STRUCTURAL CAPACITY OF DRILLED SHAFTS	57
5.1.1 Concrete	57
5.1.2 Structural capacity of drilled shafts without anomalies via ACI Code.....	58

DRILLED SHAFT AXIAL CAPACITY, EFFECTS DUE TO ANOMALIES - TABLE OF CONTENTS

5.2. STRUCTURAL CAPACITY OF DRILLED SHAFTS WITH ANOMALIES59
 5.2.1 Size, location, and properties of anomalies59
 5.2.2 Structure capacity of drilled shafts with anomalies63
5.3. SOIL PROPERTIES64
5.4. SHAFT MODEL.....67
5.5. DEFINE THE EFFECT OF ANOMALIES68
5.6. CAPACITIES OF DRILLED SHAFTS IN COHESIVE SOILS69
5.7. CAPACITIES OF DRILLED SHAFTS IN COHESIONLESS SOILS81
5.8. CAPACITIES OF DRILLED SHAFTS IN COHESIVE SOIL WITH
 BEDROCK AT SHAFT TIP90

CHAPTER 6 - SUMMARY, CONCLUSIONS, AND RECOMMENDATIONS93
 6.1. SUMMARY93
 6.2. CONCLUSIONS.....93
 6.3. RECOMMENDATIONS FOR REMEDIATION94
 6.4. FUTURE STUDY95

APPENDIX A – FIGURES97

REFERENCES131

LIST OF FIGURES

Figure 1. Defective drilled shaft with multiple types of anomalies (DiMaggio, 2008).....1

Figure 2. Drilled shaft profile in varved clay and legend for planned and predicted anomalies (Iskander, et al., 2003)4

Figure 3. Planned and predicted anomalies in Shaft #2 (Iskander, et al., 2003).....4

Figure 4. Planned and predicted anomalies in Shaft #4 (Iskander, et al., 2003).....5

Figure 5. Parameter of void flaws (after O’Neill, et al., 2003).....7

Figure 6. Moment deflection curves for flexural tests (after O’Neill, et al., 2003).....7

Figure 7. Moment deflection curves for combined loading tests (after O’Neill, et al., 2003)8

Figure 8. Asymmetric anomaly (Jung, et al., 2006).....9

Figure 9. Normalized axial stress across defective section (Jung, et al., 2006).....9

Figure 10. Typical cylindrical anomaly in a drilled shaft (Haramy, 2006)10

Figure 11. Variation of α with c_u/p_a (Kulhawy and Jackson, 1989)12

Figure 12. Back-calculated lateral earth pressure coefficient K versus depth for load tests along with boundaries for $(K_0)_{NC}$ and K_p (Rollins, et al., 2005)15

Figure 13. Back-calculated β versus depth from load tests in (Rollins, et al., 2005)16

Figure 14. Predicted and actual f_s values for sands, sand gravels, and gravels (Harraz, et al., 2005).....16

Figure 15. Back-calculated Horizontal stress to Vertical stress ratio, K , vs. % Gravel (Harraz, et al., 2005).....17

Figure 16. Back-calculated Horizontal stress to Vertical stress ratio, K , vs. Depth to Mid-layer (Harraz, et al., 2005)17

Figure 17. Initial empirical model (Harraz, et al., 2005)18

Figure 18. Predicted and actual f_s values for sands, sand gravels, and gravels using the initial empirical model (Harraz, et al., 2005)18

Figure 19. Numerical model of an axially loaded shaft and load transfer curve19

Figure 20. Elasto-perfect plastic model20

Figure 21. Hyperbolic model20

Figure 22. Variation of tangent shear modulus for hyperbolic and modified hyperbolic models22

Figure 23. Shearing of concentric cylinders (Kraft, et al., 1981)23

Figure 24. Shaft base load and shaft base displacement curve (API 1993).....25

Figure 25. Normalized side load transfer for drilled shafts in cohesive soil (after O’Neill and Reese, 1999)27

Figure 26. Normalized base load transfer for drilled shafts in cohesive soil (after O’Neill and Reese, 1999)27

Figure 27. Shaft Normalized side load transfer for drilled shafts in cohesionless soil (after O’Neill and Reese, 1999)28

Figure 28. Normalized base load transfer for drilled shafts in cohesionless soil (after O’Neill and Reese, 1999)28

Figure 29. Normalized base load transfer for drilled shafts in cohesionless soil (after Rollins, et al., 2005)29

Figure 30. Strain distributions corresponding to point on the P-M interaction diagram (McGregor and Wight, 2005)32

DRILLED SHAFT AXIAL CAPACITY, EFFECTS DUE TO ANOMALIES - TABLE OF CONTENTS

Figure 31. Nonconcentric anomaly.....	32
Figure 32. Stress strain curve for concrete (O'Neill and Reese, 1999)	33
Figure 33. Stress strain curve for steel (O'Neill and Reese, 1999).....	34
Figure 34. Finite strips of cross section	34
Figure 35. Finite element types.....	35
Figure 36. Mohr-Coulomb failure criteria	38
Figure 37. Yield surface for cap model (Desai and Siriwardane, 1984).....	39
Figure 38. Nonlinear model of bar element.....	40
Figure 39. Side view and 3D view of finite element mesh.....	42
Figure 40. Comparison the result between PSI, PLAXIS, BEM, and test results	42
Figure 41. Effect of finite element mesh	43
Figure 42. Side view and 3D view of finite element mesh.....	44
Figure 43. Comparison of the result between PSI, ABAQUS, and test data.....	45
Figure 44. Socketed shaft (Brown, et al., 2001)	46
Figure 45. Comparison of shaft head displacement for single socketed shaft.....	46
Figure 46. C_u and K_0 profiles (Wang and Sita, 2004).....	47
Figure 47. Comparison of the result between PSI, OPENSEES, and test data.....	48
Figure 48. Schematics of numerical shaft-load test.....	50
Figure 49. Finite element mesh for the numerical shaft-load test (axisymmetric condition).....	50
Figure 50. Numerical unconfined compression test for concrete	52
Figure 51. Numerical triaxial compression tests of sand used in the comparative study	53
Figure 52. Numerical static shaft-load test comparison between LS-DYNA and PSI with perfect shaft and without contact interface.....	53
Figure 53. Location of anomaly near the shaft top.....	54
Figure 54. Numerical static shaft-load test comparison between LS-DYNA and PSI with anomaly at top of shaft and without contact interface.....	54
Figure 55. Numerical static shaft-load test comparison between LS-DYNA and PSI with contact interface between shaft and soil	55
Figure 56. Stress strain curves for concrete cylinders	57
Figure 57. Load-displacement curves of four concrete drilled shafts.....	59
Figure 58. Anomaly locations.....	61
Figure 59. Anomaly sizes and shapes (shaded areas are anomaly zones)	62
Figure 60. Structural capacity and interaction diagram of nonconcentric anomaly section.....	64
Figure 61. Dilatancy angles for sands (Bolton, 1986)	66
Figure 62. Plane and 3-D views of a drilled shaft with symmetric anomaly.....	67
Figure 63. Plane and 3-D views of a drilled shaft with nonconcentric anomaly	67
Figure 64. Effect definition of anomaly.....	68
Figure 65. Load-settlement curves for 1-m diameter drilled shaft in clay, various stiffness	70
Figure 66. Load-settlement curves for 2-m diameter drilled shaft in clay, various stiffness	70
Figure 67. Shaft-load transfer and structural capacity curves for 1-m drilled shafts with 3,000 psi concrete constructed in clay	71
Figure 68. Shaft-load transfer and structural capacity curves for 1-m drilled shafts with 4,500 psi concrete constructed in clay	71
Figure 69. Shaft-load transfer and structural capacity curves for 2-m drilled shafts with 3,000 psi concrete constructed in clay.....	72

DRILLED SHAFT AXIAL CAPACITY, EFFECTS DUE TO ANOMALIES - TABLE OF CONTENTS

Figure 70. Shaft-load transfer and structural capacity curves for 2-m drilled shafts with 4,5000 psi concrete constructed in clay	72
Figure 71. Neck-in anomaly Type 1 and cylindrical anomaly at 1-m depth, D = 2 m	74
Figure 72. Neck-in anomaly Type 1 and cylindrical anomaly at 11-m depth, D = 2 m	74
Figure 73. Comparison of short and long anomalies	75
Figure 74. Load-settlement curves for drilled shafts of 1-m diameter in sand	82
Figure 75. Load-settlement curves for drilled shafts of 2-m diameter in sand	82
Figure 76. Shaft-load transfer curves for drilled shafts of 1-m diameter in sand	83
Figure 77. Shaft-load transfer curves for drilled shafts of 1-m diameter in sand	83
Figure 78. Shaft-load transfer curves for drilled shafts of 2-m diameter in sand	84
Figure 79. Shaft-load transfer curves for drilled shafts of 2-m diameter in sand	84
Figure 80. Load-settlement curves for drilled shafts of 1-m diameter in clay (Concrete strength 3000 psi, 1-m length cylindrical anomaly at 1-m depth)	97
Figure 81. Load-settlement curves for drilled shafts of 1-m diameter in clay (Concrete strength 4500 psi, 1-m length cylindrical anomaly at 1-m depth)	97
Figure 82. Load-settlement curves for drilled shafts of 1-m diameter in clay (Concrete strength 4500 psi, 1-m length cylindrical anomaly at 11-m depth)	98
Figure 83. Load-settlement curves for drilled shafts of 1-m diameter in clay (Concrete strength 4500 psi, 1-m length cylindrical anomaly at 11-m depth)	98
Figure 84. Load-settlement curves for drilled shafts of 1-m diameter in clay (Concrete strength 4500 psi, 1.2-m length cylindrical anomaly at 19-m depth)	99
Figure 85. Load-settlement curves for drilled shafts of 1-m diameter in clay (Concrete strength 4500 psi, 1.2-m length cylindrical anomaly at 19-m depth)	99
Figure 86. Load-settlement curves for drilled shafts of 1-m diameter in clay (Concrete strength 3000 psi, 1-m length neck-in anomaly type 2 at 1-m depth)	100
Figure 87. Load-settlement curves for drilled shafts of 1-m diameter in clay (Concrete strength 4500 psi, 1-m length neck-in anomaly type 2 at 1-m depth)	100
Figure 88. Load-settlement curves for drilled shafts of 1-m diameter in clay (Concrete strength 3000 psi, 1-m length neck-in anomaly type 2 at 11-m depth)	101
Figure 89. Load-settlement curves for drilled shafts of 1-m diameter in clay (Concrete strength 4500 psi, 1-m length neck-in anomaly type 2 at 11-m depth)	101
Figure 90. Load-settlement curves for drilled shafts of 1-m diameter in clay (Concrete strength 3000 psi, 1-m length neck-in anomaly type 3 at 1-m depth)	102
Figure 91. Load-settlement curves for drilled shafts of 1-m diameter in clay (Concrete strength 4500 psi, 1-m length neck-in anomaly type 3 at 1-m depth)	102
Figure 92. Load-settlement curves for drilled shafts of 1-m diameter in clay (Concrete strength 3000 psi, 1-m length neck-in anomaly type 3 at 11-m depth)	103
Figure 93. Load-settlement curves for drilled shafts of 1-m diameter in clay (Concrete strength 4500 psi, 1-m length neck-in anomaly type 3 at 11-m depth)	103
Figure 94. Load-settlement curves for drilled shafts of 1-m diameter in clay (Concrete strength 3000 psi, 1-m length neck-in anomaly type 3 at 19-m depth)	104
Figure 95. Load-settlement curves for drilled shafts of 1-m diameter in clay (Concrete strength 4500 psi, 1-m length neck-in anomaly type 3 at 19-m depth)	104
Figure 96. Load-settlement curves for drilled shafts of 2-m diameter in clay (Concrete strength 3000 psi, 1-m length neck-in anomaly type 2 at 1-m depth)	105
Figure 97. Load-settlement curves for drilled shafts of 2-m diameter in clay	

DRILLED SHAFT AXIAL CAPACITY, EFFECTS DUE TO ANOMALIES - TABLE OF CONTENTS

(Concrete strength 4500 psi, 1-m length neck-in anomaly type 2 at 1-m depth)	105
Figure 98. Load-settlement curves for drilled shafts of 2-m diameter in clay	
(Concrete strength 3000 psi, 1-m length neck-in anomaly type 2 at 11-m depth)	106
Figure 99. Load-settlement curves for drilled shafts of 2-m diameter in clay	
(Concrete strength 4500 psi, 1-m length neck-in anomaly type 2 at 11-m depth)	106
Figure 100. Load-settlement curves for drilled shafts of 2-m diameter in clay	
(Concrete strength 3000 psi, 1.2-m length neck-in anomaly type 2 at 19-m depth)	107
Figure 101. Load-settlement curves for drilled shafts of 2-m diameter in clay	
(Concrete strength 4500 psi, 1.2-m length neck-in anomaly type 2 at 19-m depth)	107
Figure 102. Load-settlement curves for drilled shafts of 2-m diameter in clay	
(Concrete strength 3000 psi, 1-m length neck-in anomaly type 3 at 1-m depth)	108
Figure 103. Load-settlement curves for drilled shafts of 2-m diameter in clay	
(Concrete strength 4500 psi, 1-m length neck-in anomaly type 3 at 1-m depth)	108
Figure 104. Load-settlement curves for drilled shafts of 2-m diameter in clay	
(Concrete strength 3000 psi, 1-m length neck-in anomaly type 3 at 11-m depth)	109
Figure 105. Load-settlement curves for drilled shafts of 2-m diameter in clay	
(Concrete strength 4500 psi, 1-m length neck-in anomaly type 3 at 11-m depth)	109
Figure 106. Load-settlement curves for drilled shafts of 2-m diameter in clay	
(Concrete strength 3000 psi, 1.2-m length neck-in anomaly type 3 at 19-m depth)	110
Figure 107. Load-settlement curves for drilled shafts of 2-m diameter in clay	
(Concrete strength 4500 psi, 1.2-m length neck-in anomaly type 3 at 19-m depth)	110
Figure 108. Load-settlement curves for drilled shafts of 1-m diameter in sand	
(Concrete strength 3000 psi, 1-m length cylindrical anomaly at 1-m depth)	111
Figure 109. Load-settlement curves for drilled shafts of 1-m diameter in sand	
(Concrete strength 4500 psi, 1-m length cylindrical anomaly at 1-m depth)	111
Figure 110. Load-settlement curves for drilled shafts of 1-m diameter in sand	
(Concrete strength 3000 psi, 1-m length cylindrical anomaly at 11-m depth)	112
Figure 111. Load-settlement curves for drilled shafts of 1-m diameter in sand	
(Concrete strength 4500 psi, 1-m length cylindrical anomaly at 11-m depth)	112
Figure 112. Load-settlement curves for drilled shafts of 1-m diameter in sand	
(Concrete strength 3000 psi, 1-m length cylindrical anomaly at 11-m depth)	113
Figure 113. Load-settlement curves for drilled shafts of 1-m diameter in sand	
(Concrete strength 4500 psi, 1-m length cylindrical anomaly at 11-m depth)	113
Figure 114. Load-settlement curves for drilled shafts of 1-m diameter in sand	
(Concrete strength 3000 psi, 1.2-m length cylindrical anomaly at 191-m depth)	114
Figure 115. Load-settlement curves for drilled shafts of 1-m diameter in sand	
(Concrete strength 4500 psi, 1.2-m length cylindrical anomaly at 19-m depth)	114
Figure 116. Load-settlement curves for drilled shafts of 1-m diameter in sand	
(Concrete strength 3000 psi, 1-m length neck-in anomaly type 2 at 1-m depth)	115
Figure 117. Load-settlement curves for drilled shafts of 1-m diameter in sand	
(Concrete strength 4500 psi, 1-m length neck-in anomaly type 2 at 1-m depth)	115
Figure 118. Load-settlement curves for drilled shafts of 1-m diameter in sand	
(Concrete strength 3000 psi, 1-m length neck-in anomaly type 2 at 11-m depth)	116
Figure 119. Load-settlement curves for drilled shafts of 1-m diameter in sand	
(Concrete strength 4500 psi, 1-m length neck-in anomaly type 2 at 11-m depth)	116
Figure 120. Load-settlement curves for drilled shafts of 1-m diameter in sand	

DRILLED SHAFT AXIAL CAPACITY, EFFECTS DUE TO ANOMALIES - TABLE OF CONTENTS

(Concrete strength 3000 psi, 1.2-m length neck-in anomaly type 2 at 19-m depth)	117
Figure 121. Load-settlement curves for drilled shafts of 1-m diameter in sand	
(Concrete strength 4500 psi, 1.2-m length neck-in anomaly type 2 at 19-m depth)	117
Figure 122. Load-settlement curves for drilled shafts of 1-m diameter in sand	
(Concrete strength 3000 psi, 1-m length neck-in anomaly type 3 at 1-m depth)	118
Figure 123. Load-settlement curves for drilled shafts of 1-m diameter in sand	
(Concrete strength 4500 psi, 1-m length neck-in anomaly type 3 at 1-m depth)	118
Figure 124. Load-settlement curves for drilled shafts of 1-m diameter in sand	
(Concrete strength 3000 psi, 1-m length neck-in anomaly type 3 at 11-m depth)	119
Figure 125. Load-settlement curves for drilled shafts of 1-m diameter in sand	
(Concrete strength 4500 psi, 1-m length neck-in anomaly type 3 at 11-m depth)	119
Figure 126. Load-settlement curves for drilled shafts of 1-m diameter in sand	
(Concrete strength 3000 psi, 1.2-m length neck-in anomaly type 3 at 19-m depth)	120
Figure 127. Load-settlement curves for drilled shafts of 1-m diameter in sand	
(Concrete strength 4500 psi, 1.2-m length neck-in anomaly type 3 at 19-m depth)	120
Figure 128. Load-settlement curves for drilled shafts of 2-m diameter in sand	
(Concrete strength 3000 psi, 1-m length cylindrical anomaly at 1-m depth)	121
Figure 129. Load-settlement curves for drilled shafts of 2-m diameter in sand	
(Concrete strength 4500 psi, 1-m length cylindrical anomaly at 1-m depth)	121
Figure 130. Load-settlement curves for drilled shafts of 2-m diameter in sand	
(Concrete strength 3000 psi, 1-m length cylindrical anomaly at 11-m depth)	122
Figure 131. Load-settlement curves for drilled shafts of 2-m diameter in sand	
(Concrete strength 4500 psi, 1-m length cylindrical anomaly at 11-m depth)	122
Figure 132. Load-settlement curves for drilled shafts of 2-m diameter in sand	
(Concrete strength 3000 psi, 1.2-m length cylindrical anomaly at 19-m depth)	123
Figure 133. Load-settlement curves for drilled shafts of 2-m diameter in sand	
(Concrete strength 4500 psi, 1.2-m length cylindrical anomaly at 19-m depth)	123
Figure 134. Load-settlement curves for drilled shafts of 2-m diameter in sand	
(Concrete strength 3000 psi, 1-m length neck-in anomaly type 2 at 1-m depth)	124
Figure 135. Load-settlement curves for drilled shafts of 2-m diameter in sand	
(Concrete strength 4500 psi, 1-m length neck-in anomaly type 2 at 1-m depth)	124
Figure 136. Load-settlement curves for drilled shafts of 2-m diameter in sand	
(Concrete strength 3000 psi, 1-m length neck-in anomaly type 2 at 11-m depth)	125
Figure 137. Load-settlement curves for drilled shafts of 2-m diameter in sand	
(Concrete strength 4500 psi, 1-m length neck-in anomaly type 2 at 11-m depth)	125
Figure 138. Load-settlement curves for drilled shafts of 2-m diameter in sand	
(Concrete strength 3000 psi, 1-m length neck-in anomaly type 2 at 19-m depth)	126
Figure 139. Load-settlement curves for drilled shafts of 2-m diameter in sand	
(Concrete strength 4500 psi, 1-m length neck-in anomaly type 2 at 19-m depth)	126
Figure 140. Load-settlement curves for drilled shafts of 2-m diameter in sand	
(Concrete strength 3000 psi, 1-m length neck-in anomaly type 3 at 1-m depth)	127
Figure 141. Load-settlement curves for drilled shafts of 2-m diameter in sand	
(Concrete strength 4500 psi, 1-m length neck-in anomaly type 3 at 1-m depth)	127
Figure 142. Load-settlement curves for drilled shafts of 2-m diameter in sand	
(Concrete strength 3000 psi, 1-m length neck-in anomaly type 3 at 11-m depth)	128

DRILLED SHAFT AXIAL CAPACITY, EFFECTS DUE TO ANOMALIES - TABLE OF CONTENTS

Figure 143. Load-settlement curves for drilled shafts of 2-m diameter in sand (Concrete strength 4500 psi, 1-m length neck-in anomaly type 3 at 11-m depth)	128
Figure 144. Load-settlement curves for drilled shafts of 2-m diameter in sand (Concrete strength 3000 psi, 1-m length neck-in anomaly type 3 at 19-m depth)	129
Figure 145. Load-settlement curves for drilled shafts of 2-m diameter in sand (Concrete strength 4500 psi, 1-m length neck-in anomaly type 3 at 19-m depth)	129

LIST OF TABLES

Table 1. The comparison capacity of Shafts #2 and #4	5
Table 2. Values of I_r and N_c^* (Reese, et al., 2006).....	13
Table 3. β for Gravelly sands and gravels (Rollins, et al., 2005).....	15
Table 4. Exponent M for shear modulus (Hardin and Drnevich, 1972)	23
Table 5. Empirical load transfer curves	26
Table 6. Material parameter for soil data (Brinkgreve, 2004)	41
Table 7. Soil parameters from triaxial test results	42
Table 8. Adjusted soil parameter for match case.....	43
Table 9. Material parameter for soil data (Brown, et al., 2001)	46
Table 10. Material parameters used in the comparative study.....	51
Table 11. Concrete material.....	57
Table 12. Structural capacity of concrete without reduction	58
Table 13. Structural capacity of drilled shafts with 2% reinforcement	58
Table 14. Anomaly sizes.....	60
Table 15. Anomaly locations	60
Table 16. Structural capacities of drilled shafts with anomalies	63
Table 17. Strength properties of soil.....	65
Table 18. Geotechnical capacity of drilled shafts in cohesive soil.....	69
Table 19. Drilled shaft capacity reduction for the case of concrete strength 3000 psi, shaft in clay, shaft diameter $D = 1$ m, anomaly length 1-1.2 m.....	76
Table 20. Drilled shaft capacity reduction for the case of concrete strength 4500 psi, shaft in clay, shaft diameter $D = 1$ m, anomaly length 1-1.2 m.....	77
Table 21. Drilled shaft capacity reduction for the case of concrete strength 3000 psi, shaft in clay, shaft diameter $D = 2$ m, anomaly length 1-1.2 m.....	78
Table 22. Drilled shaft capacity reduction for the case of concrete strength 4500 psi, shaft in clay, shaft diameter $D = 2$ m, anomaly length 1-1.2 m.....	79
Table 23. Drilled shaft capacity reduction for nonconcentric anomaly, concrete strength 3000 psi, diameter $D = 2$ m, shaft in clay, anomaly length 1-1.2 m	80
Table 24. Drilled shaft capacity reduction for nonconcentric anomaly, concrete strength 4500 psi, diameter $D = 2$ m, shaft in clay, anomaly length 1-1.2 m	80
Table 25. Capacity of drilled shafts in sandy soil.....	81
Table 26. Drilled shaft capacity reduction for the case of concrete strength 3000 psi, shaft in sand, shaft diameter $D = 1$ m, anomaly length 1-1.2 m	85
Table 27. Drilled shaft capacity reduction for the case of concrete strength 4500 psi, shaft in sand, shaft diameter $D = 1$ m, anomaly length 1-1.2 m	86
Table 28. Drilled shaft capacity reduction for the case of concrete strength 3000 psi, shaft in sand, shaft diameter $D = 2$ m, anomaly length 1-1.2 m	87
Table 29. Drilled shaft capacity reduction for the case of concrete strength 4500 psi, shaft in sand, shaft diameter $D = 2$ m, anomaly length 1-1.2 m	88
Table 30. Drilled shaft capacity reduction for nonconcentric anomaly, concrete strength 3000 psi, diameter $D = 2$ m, soil in sand, anomaly length 1-1.2 m.....	89
Table 31. Drilled shaft capacity reduction for nonconcentric anomaly, concrete strength 4500 psi, diameter $D = 2$ m, soil in sand, anomaly length 1-1.2 m.....	89

DRILLED SHAFT AXIAL CAPACITY, EFFECTS DUE TO ANOMALIES - TABLE OF CONTENTS

Table 32. Drilled shaft capacity reduction for the case of concrete strength 3000 psi, shaft in clay with bedrock at shaft tip, shaft diameter $D = 1$ m, anomaly length 1-1.2 m.	90
Table 33. Drilled shaft capacity reduction for the case of concrete strength 4500 psi, shaft in clay with bedrock at shaft tip, shaft diameter $D = 1$ m, anomaly length 1-1.2 m.	91
Table 34. Drilled shaft capacity reduction for the case of concrete strength 3000 psi, shaft in clay with bedrock at shaft tip, shaft diameter $D = 2$ m, anomaly length 1-1.2 m.	91
Table 35. Drilled shaft capacity reduction for the case of concrete strength 4500 psi, shaft in clay with bedrock at shaft tip, shaft diameter $D = 2$ m, anomaly length 1-1.2 m.	92

CHAPTER 1 – INTRODUCTION

Drilled shafts have gained in popularity to support heavy superstructures, including high rises and large bridges. This is attributed to minimal construction noise, high load-bearing capacity, advancement in construction and anomaly detection technologies, etc., (O'Neill and Reese, 1999; Haramy, 2006; Haramy, etc., 2007). Anomalies (or anomalies) as shown in Figure 1 include necking, bulbing, soft-bottom (or gap at the base of drilled shafts), voids or soil intrusions, poor quality concrete, debonding, lack of concrete cover over reinforcement, honey-combing defined as the void or cavity created during the concrete placement, and empty or filled with soft soils or low grade concrete (Jerry A. DiMaggio, 2008). They may occur during shaft drilling, casing, slurring, rebar cage installing, and concreting. Nondestructive evaluation (NDE) methods, such as cross-hole sonic logging (CSL), gamma-gamma testing, pulse echo testing, and sonic mobility, that can be used to detect anomalies are described in detail in the recent comprehensive works (Wightman, etc., 2004; Haramy, 2006; Haramy, 2006, 2007). Anomalies may significantly reduce the drilled shaft capacity. Therefore, it is critical to evaluate the capacity of a shaft with an anomaly to assure the Factors of Safety of the structure are met. For the purpose of this study, all anomalies are assumed to be voids; and their effects on drilled shaft capacities are evaluated using finite element analyses.

The shape, size, orientation, and radial and longitudinal locations of an anomaly with a drilled shaft can influence drilled shaft capacity in different manners. A comprehensive, finite element analysis program was carried out to evaluate the effects of various anomaly locations, size, shape, and orientation on drilled shaft capacity. A Pile-Soil Interaction (PSI) program was completed in December 2008 as a partial fulfillment of a doctoral study at the Center for Geotechnical Engineering Science (CGES) at the University Colorado, Denver. Based on PSI, another program, PSI-VA, was developed specifically for the evaluation of the effects of anomalies on drilled shaft capacity under axial load.

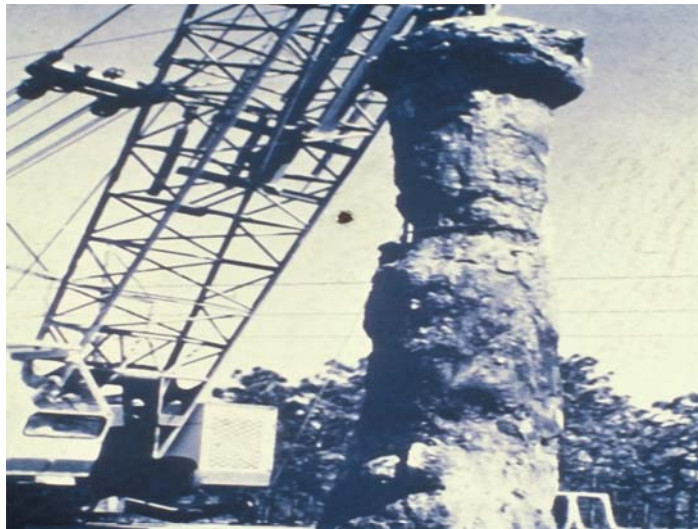


Figure 1. Defective drilled shaft with multiple types of anomalies (DiMaggio, 2008).

Chapter 2 of this report covers the review of previous literatures, contemporary design methods, and the load transfer relationship. In Chapter 3 the methods of computation for the structural capacity of drilled shafts is discussed. Presented in Chapter 4 is the theoretical basis of the PSI-VA computer program (including the integration scheme and the different constitutive material models implemented in the program) and the validation and calibration of the PSI-VA program. Case histories were used to calibrate the computation results and validate the effectiveness of PSI-VA as an effective computation tool. The many constitutive models of geomaterials provide users the choice of model alternatives and also the tool for studying the model sensitivity on the deep foundation performance prediction and simulation. Finite analysis results of the effects of anomalies are presented and discussed in Chapter 5. Chapter 6 provides the summary and conclusions of this study.

A finite element analysis program, PSI-VA (Pile-Soil Interaction under vertical load with anomalies), was used to assess the effect of different anomalies on the axial load capacities of drilled shafts in soils of various properties ranging from soft to extremely stiff clay and loose to very dense sand. Drilled shaft capacity was determined based on the lesser of structural vs. geotechnical capacity. The results indicated that anomalies affect axial structural capacity, and is highly dependent on the size, concentric location, and depth of the anomaly, and the strength of the surrounding soils. Nonconcentric anomalies decrease the structural capacity of a drilled shaft even under axial load alone.

The future development of PSI-VA will include the capability of importing the results of tomographic imaging and the analysis of effect of anomalies on drilled shaft capacity under combined vertical and lateral loads. Once completed, the PSI-VA program will become a powerful design and research tool for the investigation of effects of anomalies on drilled shaft capacity.

CHAPTER 2 – LITERATURE REVIEW

The performance of drilled shafts with anomalies requires an understanding of the design of drilled shafts without anomalies and then the impact of anomalies on the structural and geotechnical capacities. This study focuses on the effects of anomalies on the drilled shaft capacity under axial load. This chapter includes a comprehensive review of the effects of anomalies on drilled shaft capacity, design methods for drilled shaft axial capacity, and load transfer curves for drilled shaft axial capacity computation.

2.1 LITERATURE REVIEW OF CAPACITY OF DRILLED SHAFTS WITH ANOMALIES

A literature review on shafts with anomalies revealed that the studies were all recent. The following is a brief discussion from these existing studies.

Petek, et al. (2002), studied the effect of anomalies on drilled shaft axial capacity using the finite element program, PLAXIS. The drilled shafts were modeled as two-dimensional with weak layer and neck-in type anomalies in three different cohesive soil profiles. The soil properties used in analyses were modified to fit the test results. The anomalies were located at different depths within the shaft, near the top, at the middle, and near the bottom. The rectangular-shaped neck-in anomalies produced the greatest effect on drilled shaft capacity. The weak layer anomaly was modeled by low quality concrete. The study also found that the anomalies in the drilled shafts in strong soils imposed a greater effect on the drilled shaft capacity than those in weaker soils. The results showed that the effect of anomalies is dependant on their locations within the shaft. The anomalies located near the top have more effect on the drilled shaft capacity than those located at the middle and near the bottom.

Iskander, et al. (2003), studied drilled shafts constructed with anomalies located in various areas within the shaft as shown in Figures 2, 3, and 4. The purpose of the study was to assess the effect of anomalies on the axial capacity of drilled shafts in varved clay. Six drilled shafts were installed with spacing greater than five times the shaft diameter. A 1-m diameter shaft was augured to a depth of approximately 6 m with a temporary protective steel casing, and a 0.9-m diameter shaft was then augured to the final depth of 14.3 m without slurry. The reinforcing steel cage with 10 #9 steel and #4 stirrups were installed before concrete placement. Four, 52-mm inside diameter, steel pipes were installed in all shafts except for Shaft #3, which had only three pipes for the cross-hole sonic logging to study the effect of tube on test results. Concrete with 28-day strength of 28 kPa was placed using both the free fall and tremie-tube methods.

The shafts were numbered from #1 through #6, and shafts #2 and #6 were constructed with no built-in anomalies. Shafts #1, #3, #4, and #5 were constructed with built-in anomalies representing necking, voids, caving soils, and soft bottoms. The anomalies were made of a variety of materials, and some anomalies were filled with in situ soils to replicate inclusions on side walls as shown in Figures 3 and 4. The void size varies from 5 to 11% of the cross-sectional area and 0.3 to 1.5 m in length. Soil inclusions vary from 5 to 17% of the cross-sectional area. Necking was built into the shaft using 100 mm corrugated flexible plastic tubing; the occupancy

of necks was approximately 45% of the cross-sectional area and 10% for external necks. None of the shaft bottoms were cleaned but appeared to be clean prior to concrete placement. The shafts were tested using various NDT testers, with the results show in Figures 3 and 4.

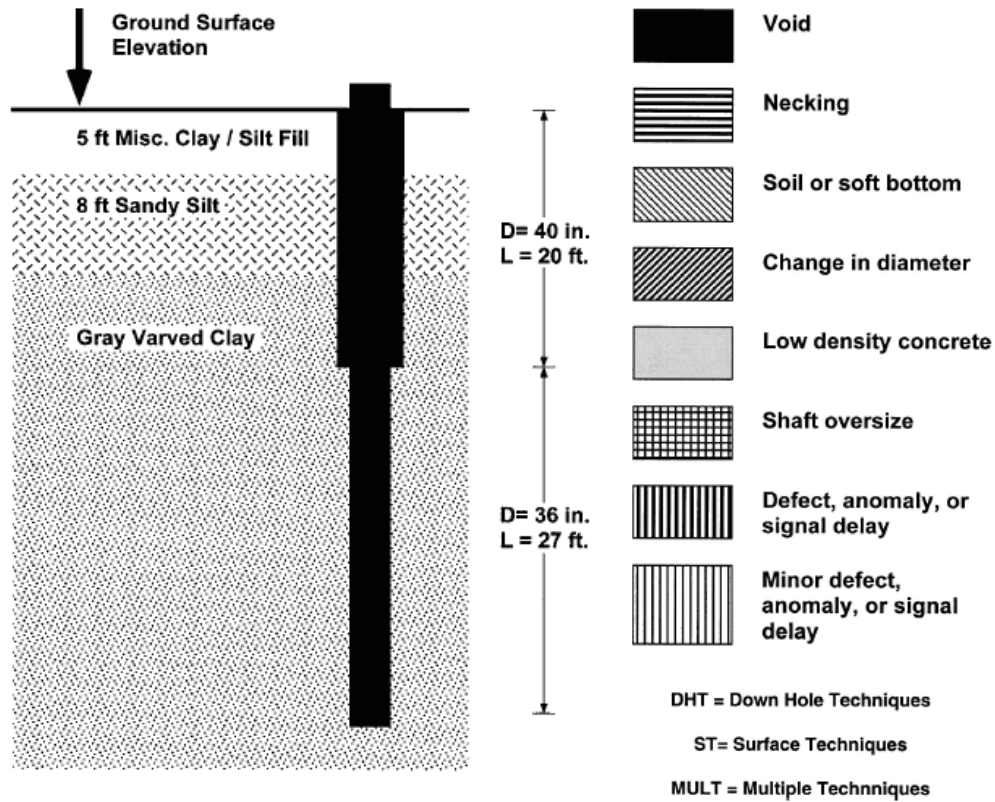


Figure 2. Drilled shaft profile in varved clay and legend for planned and predicted anomalies (Iskander, et al., 2003).

Shaft 2 Depth, m (ft)	As Built		NDT Testers - Testing Technique						
	No.	Legend	1 ST	2 DHT	3 ST	4 DHT	5 DHT	6 MULT	7 DHT
1.5 (5)									
3.0 (10)									
4.6 (15)									
6.1 (20)									
7.7 (25)									
9.2 (30)									
10.7 (35)									
12.2 (40)									
13.7 (45)									
15.2 (50)									

Figure 3. Planned and predicted anomalies in Shaft #2 (Iskander, et al., 2003).

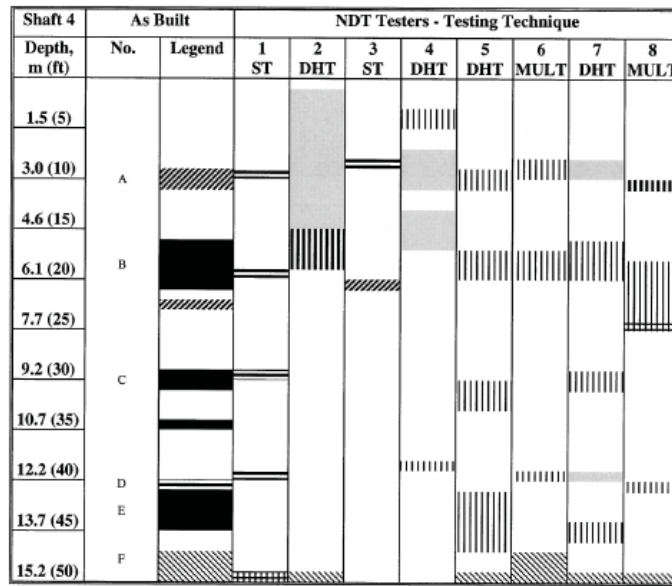


Figure 4. Planned and predicted anomalies in Shaft #4 (Iskander, et al., 2003)

Load tests on Shaft #2, which was 1.2 m shorter than the other shafts, with no planned structural anomalies and soft bottom and Shaft #4 with planned structural anomalies as shown in Figure 4, and sound bottom were performed. Both shafts were loaded to reach failure load in which Shaft #4 was loaded twice. The comparison of the capacity of two shafts is shown in Table 1. The cohesion-bearing capacity factor for the end bearing capacity of both shafts was assumed to be equal to 9, and the mobilized undrained shear strength of clay was back calculated.

Table 1. The comparison capacity of Shafts #2 and #4.

Shaft #	Davisson's Failure Criteria (kN)	Load Test Capacity (kN)	Load Test End Bearing Capacity (kN)	Undrained Shear Strength at Shaft Base (kPa)
2	1000	1200	≤ 200	34.0
4 (loading)	950	1060	300	51.0
4 (reloading)	880	1000	250	42.5

The capacity of the drilled shaft with no planned structural anomalies but with soft bottom was 5% to 10% higher than the shaft with a sound bottom and some structural anomalies. The increase of strength was insignificant, so the difference between the two drilled shafts was not recorded during construction. The mobilized undrained shear strength of 34 kPa at Shaft #2 with soft bottom was 33% lower than the virgin end bearing one at Shaft #4.

O'Neill, et al. (2003), studied the effect of undetectable structural flaws on the axial and lateral capacity of drilled shafts. Eleven scaled drilled shaft samples were tested in the lab to study the structural behavior of reinforced concrete drilled shafts with minor flaws under flexural and axial

compression loadings. Tests were performed to determine the effects of 1) shape and size of voids on the shaft's structural capacity, 2) stress concentration near the void location, 3) buckling of longitudinal reinforcement in compression within the void, and 4) strength of variations of defective shafts.

All of the shaft specimens were about one-third scale of a real shaft with 305 mm diameter; 2,260 mm length for the laterally loaded tests; and 1,830 mm length for the axially loaded tests. The specimens were tested under three different loadings: pure flexural, pure axial compression, and combined flexural and axial compression. Areas of reinforcement in specimens were 2.12% with No. 4, Grade 60, $f_y = 414$ MPa steel bars arranged in equal space around the perimeter.

The smooth wire spirals with 25.8 mm^2 of the cross-sectional area, $f_y = 448$ MPa are spaced at 25.4 mm. The concrete cover around the case was 25.4 mm. Figure 5 shows the two shapes of voids (Type 1 and Type 3), which closely simulate voids typically observed in real shafts. The voids were 15% of the gross cross-sectional area of the specimens. In all tests, voids were located in the middle on the compression side of the specimens.

Concrete cylinder tests showed that the 28-day strength of concrete, f'_c , varies from 41.3 to 45.9 MPa. In flexural tests, behaviors of defective specimens and perfect specimens are similar before yielding of reinforcement. The void significantly affected the reinforcement strength after yielding, and the Type 2 void shape imposed a more significant effect than the Type 1 void shape. The effect of void length is insignificant on strength and ductility. Failure criterion of flexural tests was chosen at a mid-span deflection of 40 mm, equivalent to concrete strain of 0.003 on top of most specimens. The moment capacity reductions of Type 1 and Type 2 specimens were about 16.5% and 33%, respectively. In axial compression tests, Figure 6 shows that voids significantly affected the shaft capacity, especially for the Type 2 void, mainly due to the lack of concrete confinement and reinforcement buckling. The axial compressive strengths were reduced by 3.5% and 7.2% for a Type 1 void with lengths of 153 mm and 305 mm, respectively, and 8.3% for a Type 2 void. The analytical strengths using ACI 318 and AASHTO Bridge Design Specification for spirally reinforced concrete under pure axial compression are 9% higher than the test results. For the combined loading test, before the yielding of reinforcement, the stiffness of the intact shaft specimen was lightly greater than the defective shaft one. Both capacity and ductility reductions are significant for the Type 2 void as shown in Figure 7. O'Neill, et al., indicated that their analytical results differed from test results by 17% due to the limitations of their computational methods attributed to the omission of factors, including strain hardening of steel, the buckling of steel rebar in the presence of a void, the longitudinal length of the void, the effect of transverse steel and the void on concrete confinement, the stress concentration in the void, and the potential steel-concrete debonding.

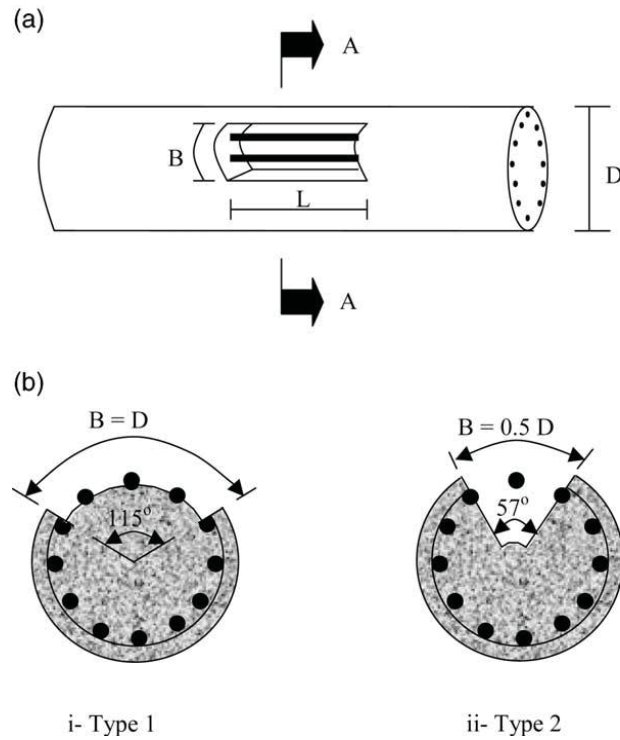


Figure 5. Parameter of void flaws: a) three dimension view; b) Section A-A (after O’Neill, et al., 2003).

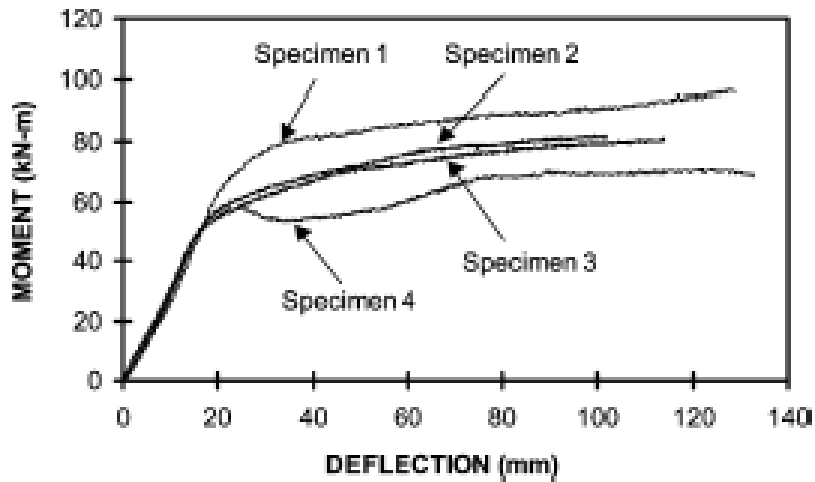


Figure 6. Moment deflection curves for flexural tests (after O’Neill, et al., 2003).

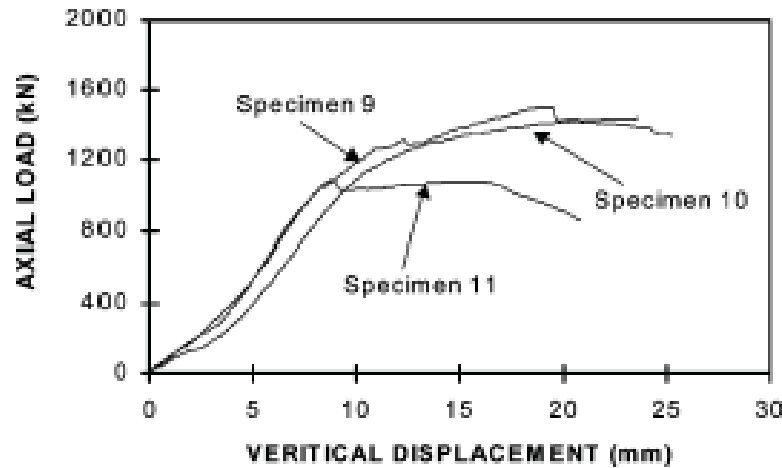


Figure 7. Moment deflection curves for combined loading tests (after O'Neill, et al., 2003).

Mullins and Ashmawy (2005) reported the findings of an experimental study on factors affecting anomaly formation in drilled shafts. The most interesting finding was that, even at the most frequently specified rebar clear spacing to aggregate diameter ratio of 3 to 5, a substantial build-up of material inside the cage was observed before enough pressure was developed to push concrete mix through the reinforcing cage into the annular region outside the cage. This allows the formation of anomalies in the annular area outside the cage. The rate of concreting was also observed to significantly affect the anomaly formation in the annular region of the drilled shaft outside the cage.

Jung G., et al. (2006), evaluated the effect of anomalies in drilled shafts on capacity. Four full-scale drilled shafts with artificial anomalies and one sound drilled shaft were constructed and tested. The artificial anomalies included soft bottom, concrete segregation, honeycomb, and contractions of cross sections by 10% to 20% as shown in Figure 8, respectively. During the static load test, load-settlement curves and load transfer curves were recorded. The numerical analyses using the finite difference program, FLAC 3D were performed to simulate the axial resistance behavior of drilled shafts.

From the analyses, the load-settlement and load transfer curves of drilled Shaft #4 with 10% contraction anomalies and Shaft #5 with 20% contraction anomalies were in good agreement with the test results. In comparison to the same curves of drilled shafts with anomalies of 10% to 20% cross section contraction, there was little difference. The measured values of normalized axial stress in each drilled shaft were both less than those of numerical analyses. For drilled Shaft #4, the difference was 7%; and, for drilled Shaft #5, the difference was 30% as shown in Figure 9.

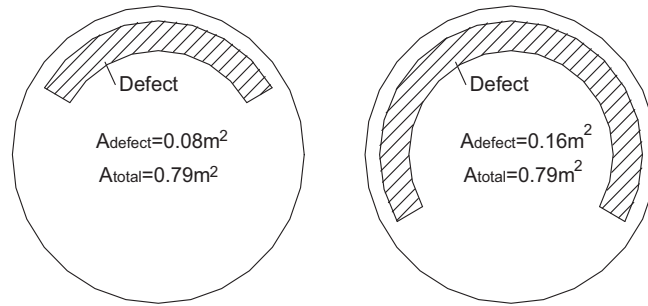


Figure 8. Asymmetric anomaly (Jung, et al., 2006).

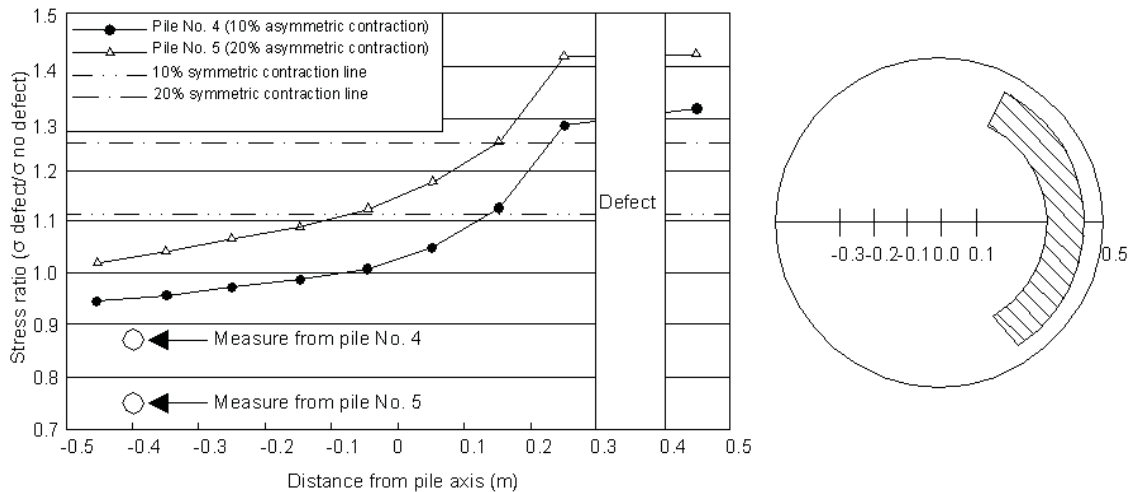


Figure 9. Normalized axial stress across defective section (Jung, et al., 2006).

Haramy (2006) presented a timely comprehensive study on the performance monitor of concrete mix during its hydration process, CSL detection of anomaly locations, tomographic imaging of the anomaly, and the effects of anomalies on drilled shaft capacity. Subsequently, two articles (Haramy, et al., 2007a and b) were published in the proceedings of the DFI 32nd Annual Conference on the related topics. Quality assurance and quality control of drilled shafts has become a concern due to difficulties in accurately locating construction anomalies, such as shown in Figure 9, and determining load bearing capacity of defected drilled shafts. Various non-destructive evaluation techniques have been developed to estimate the integrity of the concrete in drilled shafts. While these techniques have been widely accepted, variables and unknowns can affect the measurement results. Results are typically difficult to interpret, leading to unnecessary construction delays and possible litigation over shaft integrity. In addition, influences of surrounding ground materials, stress states under different load conditions, and crack and residual stress development during concrete hydration further complicate determination of shaft performance.



Figure 10. Typical cylindrical anomaly in a drilled shaft (Haramy, 2006).

Haramy, et al. (2007a), showed that 1) the curing environment could greatly affect the concrete strength and required close monitoring during construction; and 2) the NDE technology could effectively monitor curing temperature, density, and moisture, which could significantly affect the velocity measured in the cross-hole sonic logging, the rate of strength gain, and the final strength of concrete in drilled shafts and, thereby, affect their structure capacities. To understand the mechanism by which a drilled shaft cures under field conditions, three newly constructed drilled shafts were monitored for up to 7 days, immediately following concrete placement. The shaft curing rate was found to vary with depth, shaft diameter, surrounding geo-material types, and the depth of groundwater.

CSL logging showed that the sonic velocity increased with curing time until 4 to 7 days; and, at a specific time, the velocity appeared to be inversely correlated to curing temperatures. The gamma-gamma density log (GDL) showed that the average density increased with curing time but decreased slightly in 3 to 5 days. At a given time the GDL density curves seemed to correlate with the neutron moisture logging (NML) curve. The moisture was highest when surrounded by bedrock, then clay, then sand due to different hydration rates. It was found that NDE monitoring was effective in monitoring concrete curing temperature, density, velocity, and moisture; the concrete curing strength in drilled shafts is a function of time, thermal conductivity, the permeability of the surrounding soil/rock, and the depth of groundwater table.

Haramy, et al. (2007b), focused on the evaluation of load bearing capacity of drilled shafts with anomalies under various conditions by 3-D numerical analysis and modeling to evaluate the serviceability of a defected drilled shaft. Study results showed that friction angles of

surrounding geo-materials, soil density, and percentage of consolidation influence the stress concentration around anomalies and that such stress concentration can trigger crack propagation and worsen the corrosion process. When anomalies occur, the NDE methods can assist in detecting their locations and sizes. The anomaly near the top of a drilled shaft will significantly affect the structural capacity of drilled shafts. When lacking concrete confinement for reinforcement, the effect of an anomaly on a drilled shaft is more significant because of the potential for buckling.

In summary, while much research has been done on the subject of the effect of anomalies on a drilled shaft's behavior, none has comprehensively studied the effect of anomalies on a drilled shaft's capacity in different geomaterial environments, which this study aims to examine. To effectively study the subject matter, an effective computational program is needed. **PSI-VA (Pile-Soil interaction program for vertical loaded drilled shafts with anomalies)** was used. Some characteristics of PSI-VA are presented in Chapters 3 and 4, and the analysis results are presented in the subsequently chapters.

2.2 DESIGN METHOD FOR AXIAL CAPACITY

2.2.1 Design for axial capacity in cohesive soil

2.2.1.1 Side resistance in cohesive soils

The following equation gives the α method for the evaluation of the skin (side or frictional) resistance of drilled shafts in cohesive soils at depth z :

$$f_s = \alpha c_u \quad (\text{Eq. 1})$$

where

f_s = ultimate skin resistance at depth z

c_u = undrained shear strength (cohesion) at depth z

α = empirical adhesion factor dependant upon undrained cohesion.

Kulhawy and Jackson (1989) reported 65 uplift and 41 compression field tests of drilled shafts and obtained the values of α area as shown in Figure 11. The values of α varies from 0.3 to 1.0. The following best-fit functional relationship (Eq. 2) shows that the α values decrease with the increasing undrained shear strength:

$$\alpha = 0.21 + 0.25 \frac{p_a}{c_u} \quad (\text{Eq. 2})$$

where p_a = atmospheric pressure. In other words, the soft, normally consolidated clay has a higher α value than the hard, overconsolidated clay.

O'Neill and Reese (1999) collected data from many case histories to develop a correlation between c_u and f_s .

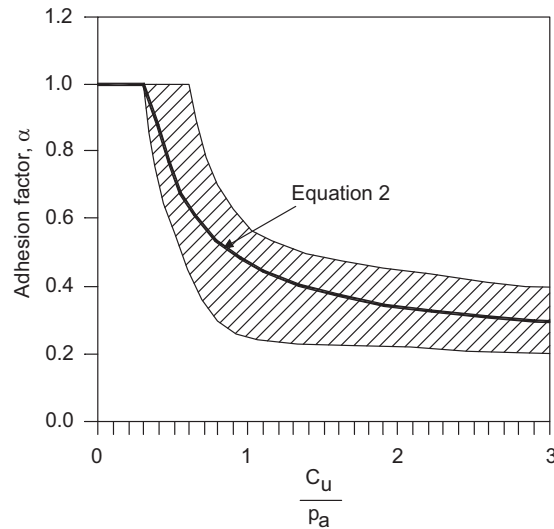


Figure 11. Variation of α with c_u/p_a (Kulhawy and Jackson, 1989).

The database was based on shafts in clay with $c_u \geq 50$ kPa and the following drilled shaft dimensions of $0.7 \leq D \leq 1.83$ m, $L \geq 7$ m. O'Neill and Reese (1999) recommended the following equation for the average value of α :

$$\alpha = 0.55 \quad \text{for } \frac{c_u}{p_a} \leq 1.5 \quad (\text{Eq. 3})$$

and

$$\alpha = 0.55 - 0.1 \left(\frac{c_u}{p_a} - 1.5 \right) \quad \text{for } 1.5 \leq \frac{c_u}{p_a} \leq 2.5 \quad (\text{Eq. 4})$$

For the case of $c_u/p_a > 2.5$, skin resistance should be calculated as the method for cohesive intermediate geomaterials (O'Neill and Reese, 1999). If the shaft length from ground surface to a depth of about 1.5 m is excluded in calculating shaft resistance to account for soil shrinkage in the zone of seasonal moisture change, then $\alpha = 0$ at depth $z \leq 1.5$ m. The lower part of the drilled shaft is also excluded because, in compression loads, the displacement of the soil at the shaft tip will generate tensile stresses in the soil that will be relieved by cracking of soil; and pore water suction will be relieved by inward movement of groundwater (O'Neill and Reese, 1999). If the length of this portion is equal to D above the shaft base, then $\alpha = 0$ at depth $z \geq L - D$.

The total skin resistance, Q_s , is equal to the peripheral area of the shaft multiplied by the unit side resistance shown as follows:

$$Q_s = \pi D \sum \alpha^i c_u^i L^i \quad (\text{Eq. 5})$$

where D = shaft diameter; L^i = thickness of layer i ; and where the values of α and c_u are constants.

2.2.1.2 End bearing in cohesive soils

The prediction of end bearing capacity of drilled shafts in clays is much less uncertain than is the prediction of skin resistance (Reese, et al., 2006). The equation below is used for calculating the net base resistance, Q_p :

$$Q_p = A_p c_u N_c^* \quad (\text{Eq. 6})$$

where A_p = the area of the base; c_u = an average undrained shear strength of clay calculated over a depth of two times the diameter below the base (Reese, et al., 2006); and N_c^* = the bearing capacity factor (usually taken to be 9) when the ratio L/D_b is ≥ 4 (Das, 1999).

According to O'Neill and Reese (1999), for the straight shaft the full value of $N_c^* = 9$ is obtained when the base movement is about 20% of D . If the base movement is unknown, the bearing capacity factor N_c^* can be calculated by (Reese, et al., 2006):

$$N_c^* = 1.33(\ln I_r + 1) \quad (\text{Eq. 7})$$

where I_r is the rigidity index of saturated clay under undrained condition:

$$I_r = \frac{E_s}{3c_u} \quad (\text{Eq. 8})$$

where E_s is undrained Young's modulus. If E_s is not measured, N_c^* and I_r can be estimated from Table 2.

Table 2. Values of I_r and N_c^* (Reese, et al., 2006).

c_u	$E_s/3c_u$	N_c^*
24 kPa (500 lb/ft ²)	50	6.5
48 kPa (1000 lb/ft ²)	150	8.0
≥ 96 (2000 lb/ft ²)	250-300	9.0

2.2.2 Design for axial capacity in cohesionless soil

2.2.2.1 Skin resistance in cohesionless soil

Meyerhoff (1976) gives the unit skin resistance based on an SPT test:

$$f_s = \frac{N}{100} \text{ (tsf)} \quad (\text{Eq. 9})$$

where N is the average SPT value, not corrected for overburden pressure.

The following equation is used to calculate the ultimate unit skin resistance in sand at depth z :

$$f_{sz} = K \sigma'_z \tan \delta \quad (\text{Eq. 10})$$

where K = a parameter that includes the effect of the lateral pressure coefficient and a correlation factor; σ'_z = the vertical effective stress in soil at depth z ; and δ = the friction angle at the interface of the shaft surface and soil.

The total side resistance calculated from the summation of each layer of the unit side resistance multiplied by the perimeter and the layer thickness is shown as follows:

$$Q_s = \pi D \sum K^i \sigma_z'^i \tan \phi_c^i L_i \quad (\text{Eq. 11})$$

Kulhawy (1991) suggested that the value of the interface friction angle, δ , was smaller than the soil friction angle, ϕ , and was affected by construction. For drilled shafts, δ/ϕ is equal to 1.0 for good construction techniques and 0.8 or smaller with poor slurry construction (Rollin, et al., 2005). The coefficient of lateral pressure, K , is a function of the coefficient of lateral pressure at rest, K_0 , and the stress changes caused by construction, loading, and desiccation. The analysis of field load tests shows that the value of K ranges from 0.1 to over 5.0 and the K/K_0 ratio varies from 0.67 to 1.0 (Rollin, et al., 2005).

O'Neill and Reese (1999) suggested the expression for the ultimate unit skin resistance in sand:

$$f_{sz} = \beta \sigma'_z \leq 200 \text{ kPa} \quad (\text{Eq. 12})$$

and

$$Q_s = \pi D \sum \beta^i \sigma_z'^i L_i \quad (\text{Eq. 13})$$

where

in sands use

$$\beta = 1.5 - 0.245z^{0.5}; \quad (0.25 \leq \beta \leq 1.20) \text{ for SPT } N_{60} \geq 15 \text{ B}/0.3 \text{ m or}$$

$$\beta = (N_{60}/15)(1.5 - 0.245z^{0.5}) \text{ for SPT } N_{60} < 15 \text{ B}/0.3 \text{ m.}$$

in gravelly sands or gravels, use the method for sands if $N_{60} < 15 \text{ B}/0.3 \text{ m}$ (O'Neill and Reese, 1999).

Rollins, et al. (2005), studied a total of 28 axial tension (uplift) tests performed at eight different sites in Northern Utah to determine the values of K and β for gravelly sand and gravel. The back-calculated K values varied with depth as shown in Figure 12, where the values of lateral earth pressure at rest $(K_0)_{NC}$ and Rankine passive pressure coefficient K_p for a range of friction angles are also shown. The back-calculated K values reach K_p near the ground surface and decrease to $(K_0)_{NC}$ at some depth. The high K values observed could be caused by the increase in lateral pressure during shearing due to dilation of granular soils. Near the ground surface with low confining pressure, the soil would dilate during shearing, causing a significant increase in lateral pressure. At greater depth, the increase in lateral pressure is less severe because of reduced chance of dilation under a higher confining (or overburden) pressure. From the above observations and other references, Rollins, et al. (2005), concluded that it may be inappropriate to determine K based on the normal stress prior to the test. The back-calculated β values from the tests both from and outside Utah are plotted in Figure 13. The data point scatter might be due to the differences in gradation, particle angularity, fines content, geologic age, OCR, and construction methods. The mean curve for gravels is significantly greater than the mean curve for gravelly sand, and both curves show the k values greater than those values from the design curve for sand from O'Neill and Reese (1999). The equations for evaluation of β values for gravelly sands and gravels are summarized in Table 3.

Table 3. β for Gravelly sands and gravels (Rollins, et al., 2005).

Percentage Gravel	β
Less than 25%	$\beta = 1.5 - 0.135z^{0.5}$; $0.25 \leq \beta \leq 1.20$
Between 25% and 50%	$\beta = 2.0 - 0.0615z^{0.75}$; $0.25 \leq \beta \leq 1.80$
Greater than 50%	$\beta = 3.4e^{-0.0265z}$; $0.25 \leq \beta \leq 3.0$

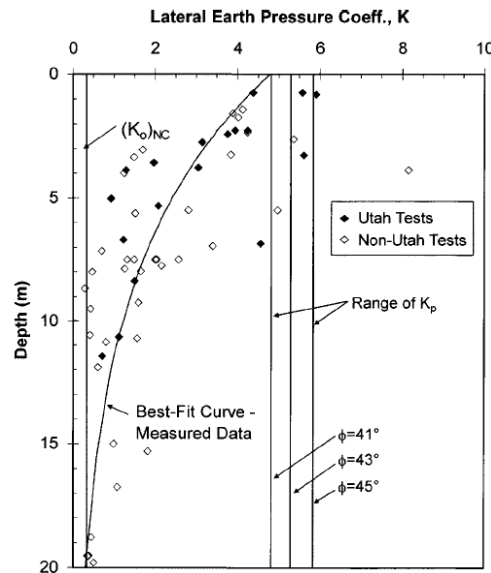


Figure 12. Back-calculated lateral earth pressure coefficient K versus depth for load tests along with boundaries for $(K_0)_{NC}$ and K_p (Rollins, et al., 2005).

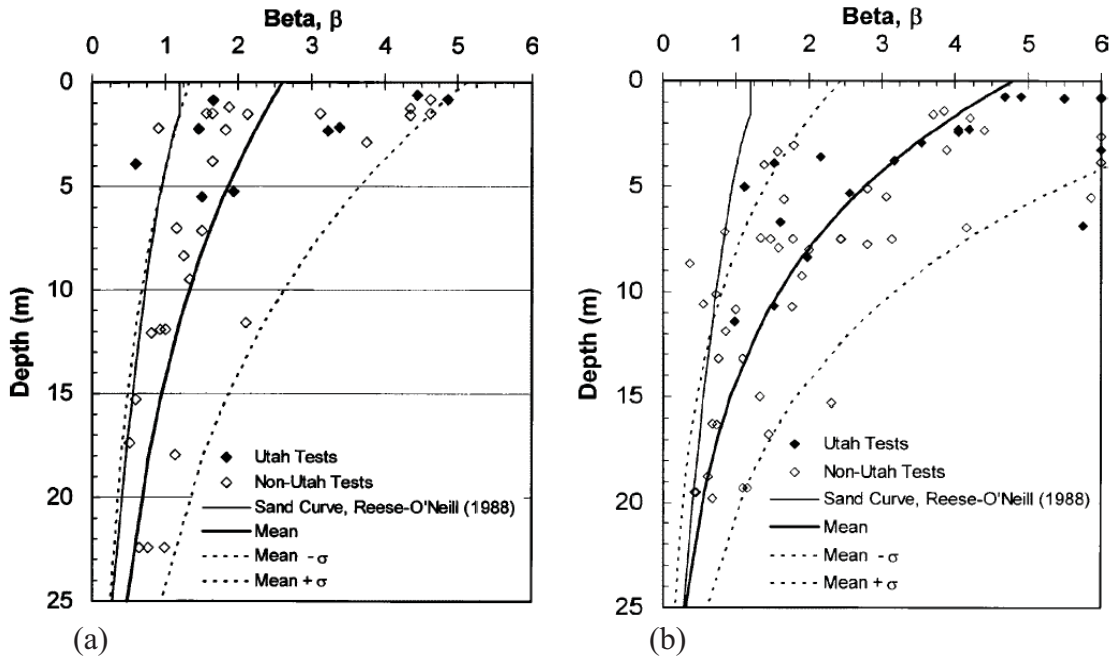


Figure 13. Back-calculated β versus depth from load tests in (a) gravelly sands and (b) gravels along with best fit curves and the curves for the upper and lower bound curves with plus and minus one standard deviation σ (Rollins, et al., 2005).

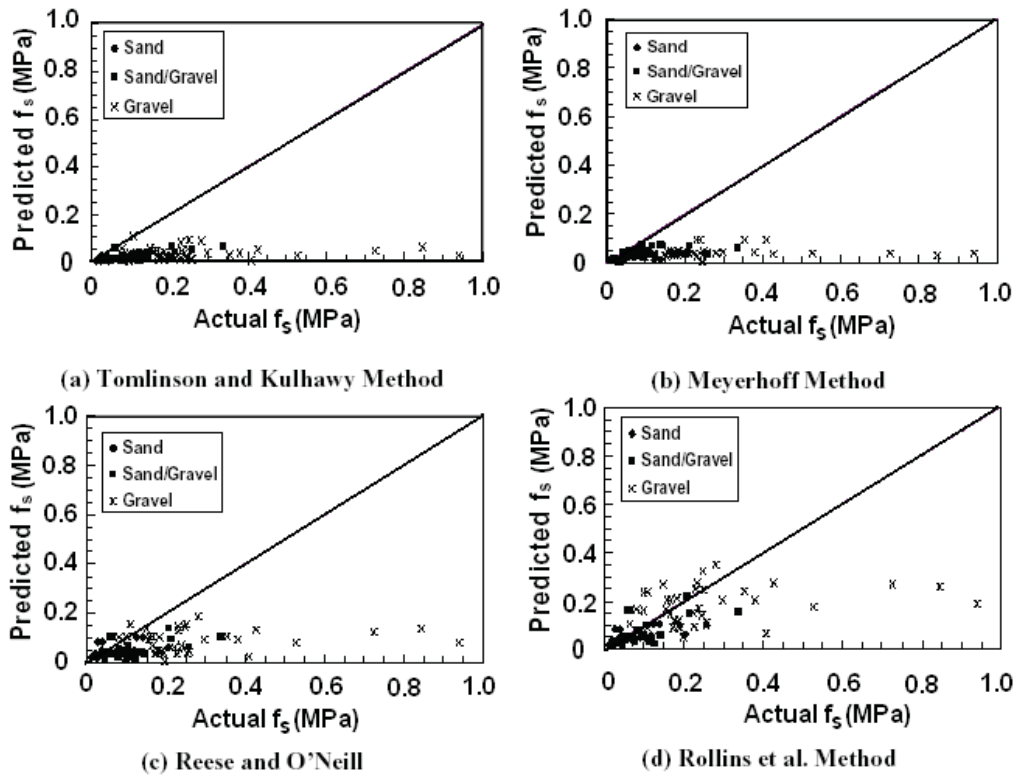


Figure 14. Predicted and actual f_s values for sands, sandy gravels, and gravels (Harraz, et al., 2005).

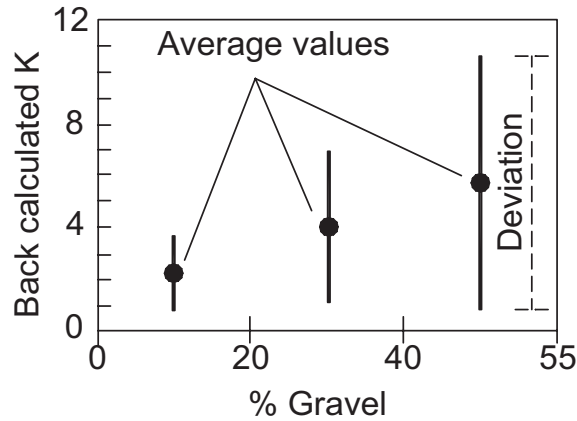


Figure 15. Back-calculated Horizontal stress to Vertical stress ratio, K , vs. % Gravel (Harraz, et al., 2005).

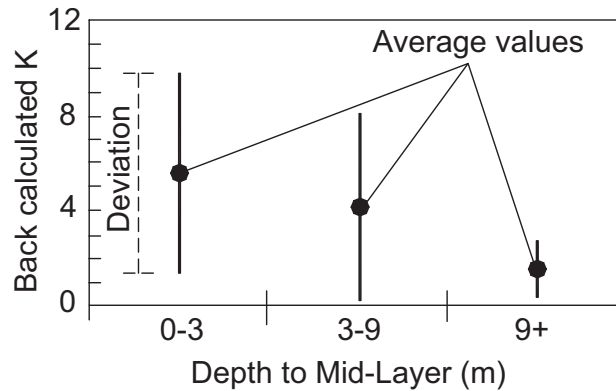


Figure 16. Back-calculated Horizontal stress to Vertical stress ratio, K , vs. Depth to Mid-layer (Harraz, et al., 2005).

Harraz, et al. (2005), evaluated 56 drilled shafts to determine the skin resistance intensity, f_s . The values of f_s derived from field measurements were compared to the values of f_s predicted using different methods. The SPT N-values were provided in almost all of the tests, and these values were correlated to the friction angle of the soils. The soil shaft interface friction angle was assumed to be equal to the friction angle of the soils. The comparisons for sands, sandy gravels, and gravels are shown in Figure 14. The Rollins, et al. (2005), method provides a reasonable prediction for sandy gravels; but the prediction for gravels is still too conservative. The Tomlinson (2001), Kulhawy (1989), Meyerhoff (1976), and Reese and O'Neill (1999) methods under predict the skin resistance for all soil types, especially gravels. To match the predicted values of f_s with the measured values of f_s , the measurement results were used in the back calculation of K values shown in Figure 15 and Figure 16. The trend of variation of K with depth is the same as that observed in the study of Rollins, et al., (2005). The initial empirical model to evaluate K values is shown in Figure 17. This model, shown in Figure 18, gives a better prediction of f_s than any of the other methods mentioned above.

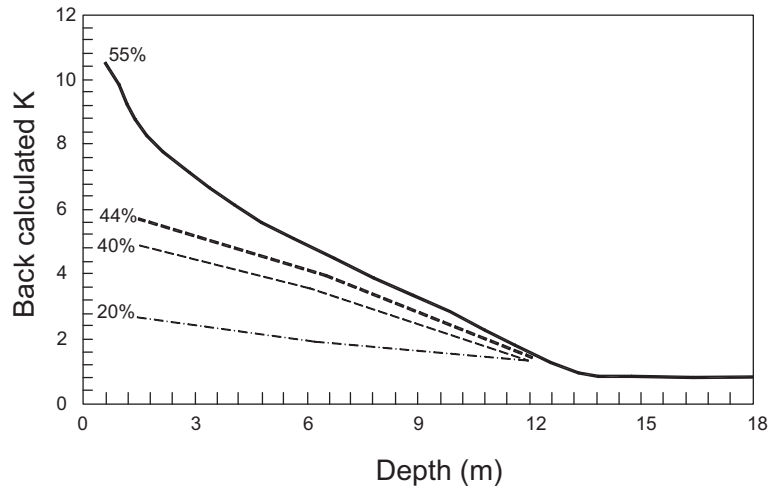


Figure 17. Initial empirical model (Harraz, et al., 2005).

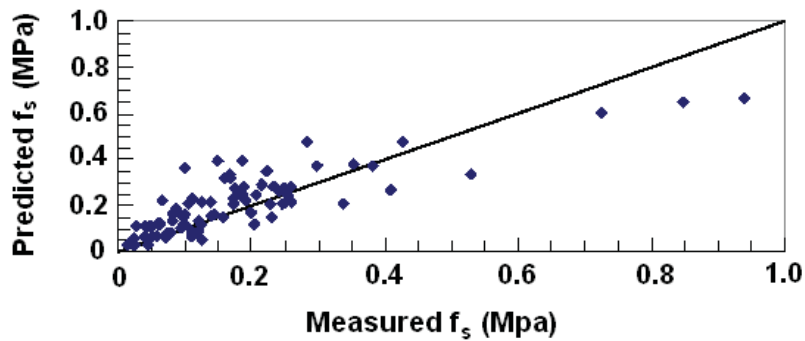


Figure 18. Predicted and actual f_s values for sands, sand gravels, and gravels using the initial empirical model (Harraz, et al., 2005).

2.2.2.2 End bearing in cohesionless soil

According to O’Neill and Reese (1999), tip resistance for cohesionless soil with blow count $N_{SPT} \leq 50$ B/0.3 m can be found by following equation:

$$q = 57.5N_{SPT} \text{ kPa} \leq 2.9 \text{ MPa} \quad (\text{Eq. 13})$$

when $N_{SPT} > 50$ B/0.3 m, q should be calculated according to the equations for intermediate geomaterials (IMGs) (O’Neill and Reese, 1999).

The above-discussed methods are also adopted by the Federal Highway Administration in its drilled design manual (O’Neill and Reese, 1999).

2.3 LOAD TRANSFER CURVES

The effect of anomalies on drilled shaft capacity depends on the anomaly location, size, and load transfer characteristics along the soil shaft interface. The effect of an anomaly occurs at a particular depth where the axial structural capacity is less than the magnitude of the load on the shaft depicted by the load transfer curve at that depth. This will be discussed in more details in Chapter 5. The Winkler concept-based load transfer assumes that the load transfer at a certain depth and at the shaft base is independent of the shaft displacement at other locations (Reese, et al., 2005). The finite element method can more realistically model and analyze the performance of a drilled shaft-soil system, where a drilled shaft is modeled by beam-column elements and soil is modeled by spring elements as shown in Figure 19. The load versus displacement relationship is nonlinear for side (skin) and base resistances as shown in Figure 19. The properties of spring elements are depicted by its soil properties, such as shear modulus, Poisson's ratio, and the strength of its soils.

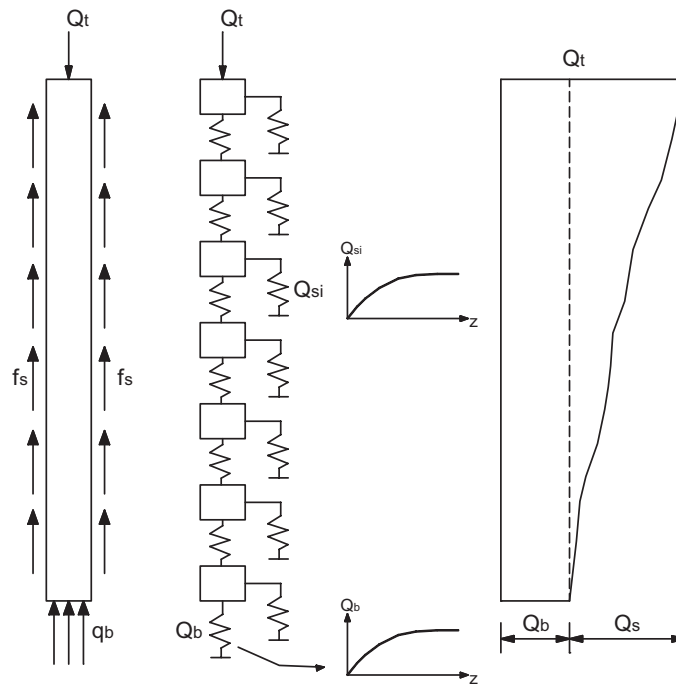


Figure 19. Numerical model of an axially loaded shaft and load transfer curve.

2.3.1 Theoretical load transfer curve

2.3.1.1 Elasto-perfect plastic model

The shear stress (τ) increases linearly with shear strain (γ) at a load smaller than the ultimate load. The relationship becomes perfectly plastic when the ultimate load is reached as shown in Figure 20. The model parameters are shear modulus (G_{max}) and ultimate shear stress (τ_{ult}).

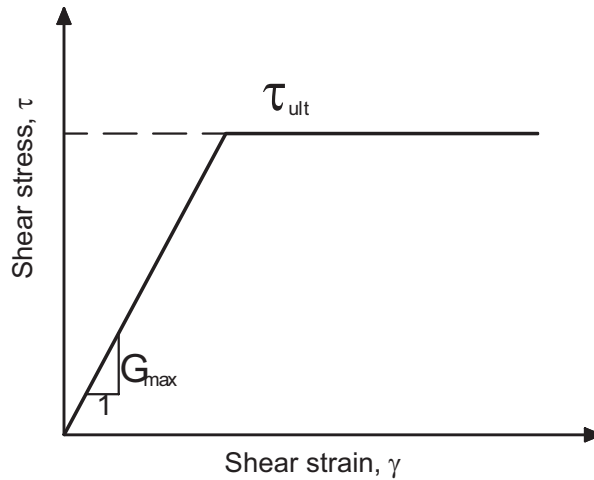


Figure 20. Elasto-perfect plastic model.

2.3.1.2 Hyperbolic model

Duncan and Chang (1970) developed the hyperbolic model to simulate the nonlinear stress-strain behavior of soils. Subsequently, it was also used to model the nonlinear load-settlement relationship of drilled shafts by several researchers, such as Kraft, et al. (1981), and Mosher (1984). The following hyperbolic equation depicts the shear stress versus the shear strain relationship for skin resistance along the perimeter of drilled shafts:

$$\tau = \frac{\gamma}{\frac{1}{G_{\max}} + \frac{\gamma}{\tau_{ult}}} \tag{Eq. 14}$$

where

γ = shear strain

G_{\max} = initial shear modulus

τ_{ult} = ultimate shear stress that the hyperbola merges asymptotically

τ = shear stress corresponding to shear strain γ

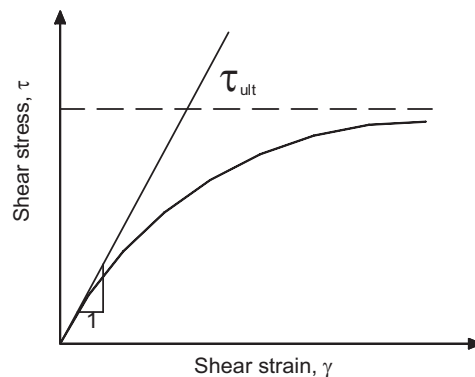


Figure 21. Hyperbolic model.

The tangent shear modulus can be calculated by differentiating Eq. (14):

$$G_t = \frac{\partial \tau}{\partial \gamma} = G_{\max} \left(1 - \frac{\tau}{\tau_{ult}} \right)^2 \quad (\text{Eq. 15})$$

The maximum shear stress, τ_{\max} , approaches asymptotically the ultimate shear stress, τ_{ult} , by a factor R_f : $\tau_{\max} = \tau_{ult} R_f$ in which R_f is a constant that varies from 0.75 to 1.0 depending on soil type (Duncan and Chang, 1970), and the failure is reached at a finite strain. Fahey and Carter (1993) proposed another form of hyperbolic model with two curve fitting parameters, f and g , to make it easier to change the shape of the stress strain curve:

$$\frac{G_s}{G_{\max}} = 1 - f \left(\frac{\tau}{\tau_{\max}} \right)^g \quad (\text{Eq. 16})$$

where G_s = secant shear modulus

f and g = curve fitting parameters with values ranging from 0 to 1.0.

The shear stress versus shear strain relationship is expressed as Eq. 17:

$$\frac{\tau}{\gamma} = G_{\max} \left[1 - f \left(\frac{\tau}{\tau_{\max}} \right)^g \right] \quad (\text{Eq. 17})$$

The tangent shear modulus is given as:

$$G_t = G_{\max} \frac{\left[1 - f \left(\frac{\tau}{\tau_{\max}} \right)^g \right]^2}{\left[1 - f(1-g) \left(\frac{\tau}{\tau_{\max}} \right)^g \right]} \quad (\text{Eq. 18})$$

Figure 22 shows the variation of tangent shear modulus for hyperbolic and modified hyperbolic models. The figure shows that the reduction of tangent shear modulus of a modified hyperbolic model is faster than hyperbolic model at a low ratio of τ and τ_{\max} .

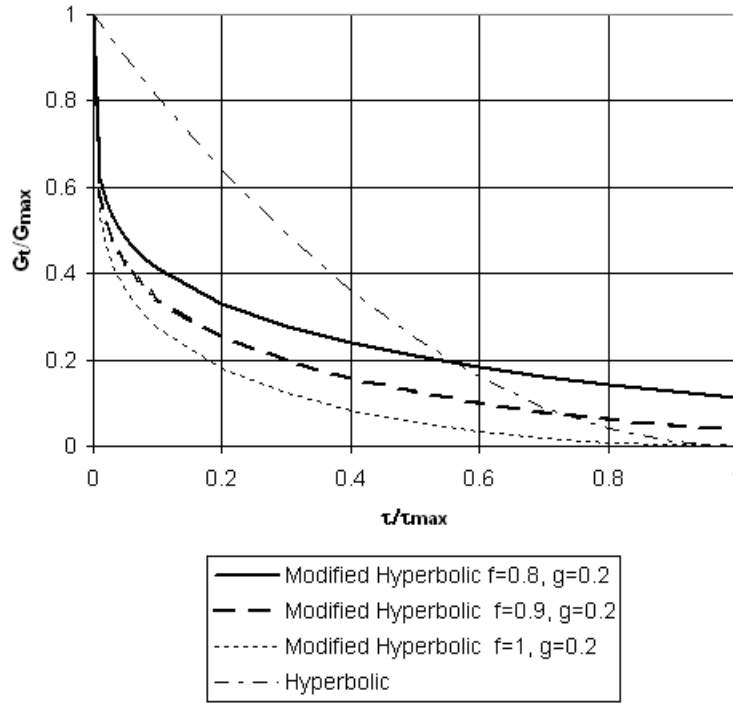


Figure 22. Variation of tangent shear modulus for hyperbolic and modified hyperbolic models.

2.3.1.3 Determination of parameters for nonlinear spring

2.3.1.3.1 Initial shear modulus

The initial shear modulus of a soil, G_{\max} , is related to its shear wave velocity, V_s , and mass density, ρ , through the following equation:

$$G_{\max} = \rho V_s^2 \quad (\text{Eq. 19})$$

In the laboratory, resonant column tests (Hardin and Drnevich, 1972) were performed to measure the shear wave velocity and formulate the following equation to evaluate the values of G_{\max} at low shear strain:

$$G_{\max}/p_a = 321 \frac{(2.97 - e)}{1 + e} OCR^M (\bar{\sigma}_0/p_a)^{0.5} \quad (\text{Eq. 20})$$

where e is the void ratio (≤ 2); $\bar{\sigma}_0$ is the mean principal effective stress; and the M exponent is related to PI as given in Table 4. p_a is atmospheric pressure, $p_a = 101.4$ kPa.

Table 4. Exponent M for shear modulus (Hardin and Drnevich, 1972)

Plasticity index, PI	Exponent, M
0	0
20	0.18
40	0.30
60	0.41
80	0.48
≥ 100	0.50

2.3.1.3.2 Spring stiffness

The parameters for nonlinear spring can be determined by soil properties such as shear modulus and Poisson’s ratio. Randolph and Wroth (1978) derived an expression for stiffness, K_s , of spring using a concentric cylinder approach as shown in Figure 23 with some assumptions:

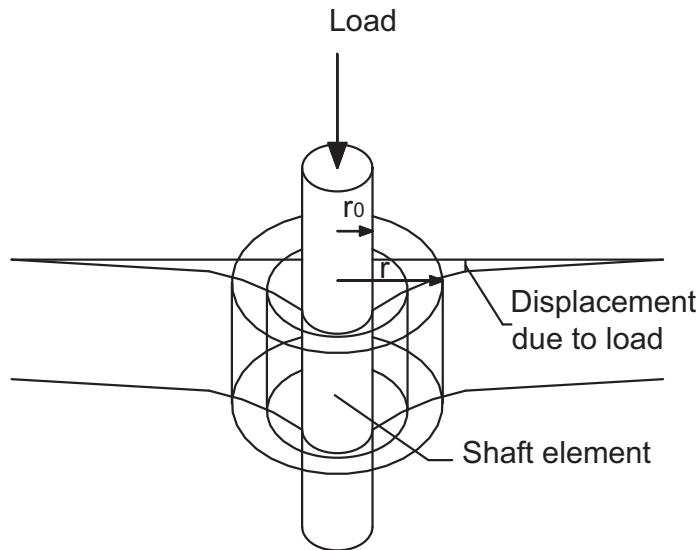


Figure 23. Shearing of concentric cylinders (Kraft, et al., 1981).

- Soil radial displacements are negligible compared to the vertical displacement. Therefore, simple shear conditions prevail.
- Shear stress decreases linearly with the distance from the shaft center such as $\tau = \tau_0 r_0 / r$ where τ is the shear stress at distance r ; τ_0 is the shear stress at the shaft soil interface; and r_0 is the shaft radius.
- Shear stress in the soil becomes negligible at the radial distance r_m .

The load-displacement relation can be written as follows:

$$z_s = \tau_0 r_0 \int_{r_0}^{r_m} \frac{dr}{Gr} \tag{Eq. 21}$$

where z_s is the shaft element displacement.

For a constant G value, Eq. 21 reduces to:

$$z_s = \frac{\tau_0 r_0}{G} \ln \left(\frac{r_m}{r_0} \right) \quad (\text{Eq. 22})$$

The spring stiffness is:

$$K_s = \frac{\tau_0}{z_s} = \frac{G}{r_0 \ln \left(\frac{r_m}{r_0} \right)} \quad (\text{Eq. 23})$$

where r_0 = shaft radius

G = shear modulus

r_m = the radial distance at which the shear stress in the soil becomes negligible. This value for r_m can be estimated by the following equation (Randolph and Wroth, 1979):

$$r_m = 2.5L\rho(1-\nu) \quad (\text{Eq. 24})$$

where

L = shaft embedment depth

ρ = factor of vertical homogeneity of soil stiffness: $\rho = G_M/G_T$ (G_M is the shear modulus at the shaft mid-depth, and G_T is the shear modulus at the shaft base)

ν = Poisson's ratio of the soil.

Guo and Randolph (1997) proposed a more general form of Eq. (24):

$$r_m = A \frac{1-\nu_s}{1+n} L + Br \quad (\text{Eq. 25})$$

where A and B are factors depending on shaft geometry, shaft soil stiffness, and various thicknesses of the finite soil layer.

The base stiffness can be approximated using Boussinesq's solution for a rigid footing resting on elastic half-space (Poulos and Davis, 1990):

$$K_b = \frac{4Gr_0}{1-\nu} \quad (\text{Eq. 26})$$

2.3.1.3.3 Ultimate force

The ultimate force can be calculated by the method shown in the above section. For side resistance of drilled shafts in cohesive soil use:

$$f_{s\max} = \pi D(\alpha c_u) \quad (\text{Eq. 27})$$

For end bearing resistance of drilled shafts in cohesive soil use:

$$Q_{b\max} = A_p c_u N_c^* \quad (\text{Eq. 28})$$

For side resistance of drilled shafts in cohesionless soil use:

$$f_{s\max} = \pi D \beta \sigma'_{vz} \quad (\text{Eq. 29})$$

For end bearing resistance of drilled shafts in cohesionless soil use:

$$Q_{b\max} = A_p \sigma'_{vz} N_q \quad (\text{Eq. 30})$$

2.3.2 Load transfer curves from field test studies

Empirically-based load transfer curves were proposed to fit the experimental data. Table 5 below summarizes the empirical load transfer function proposed by API (1993) and Vijayvergiya (1977). Figure 24 is the shaft base load versus the shaft base displacement plotted from data given in Table 5 recommended by API (1993). The mobilized bearing capacity, Q , is equal to the ultimate bearing capacity, Q_b , at the shaft base displacement equal to or greater than 0.1 multiplied by the of shaft diameter, D .

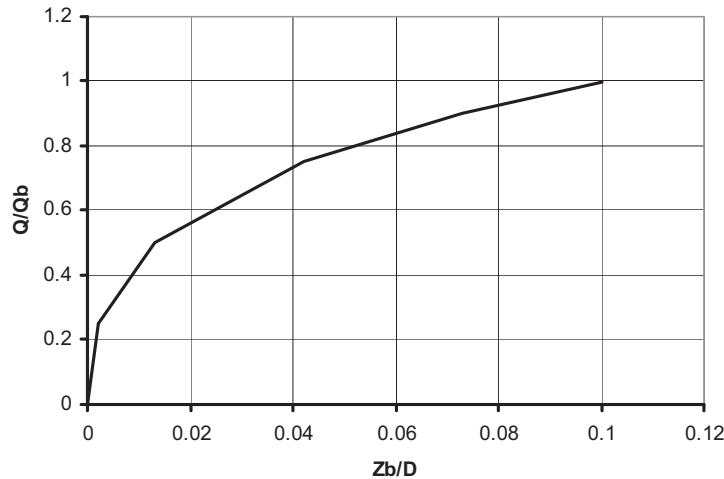


Figure 24. Shaft base load and shaft base displacement curve (API 1993).

O'Neill and Reese (1999) developed the normalized curves for side-shear and end-bearing resistances by evaluating the results of several field load tests of instrumented drilled shafts in cohesive and cohesionless soils as shown in Figure 25 to Figure 28. Rollins, et al. (2005), also represented the normalized load versus displacement curves and compared it to the similar curves developed by O'Neill and Reese (1999) for slightly cemented sands as shown in Figure 29 for gravelly sands and gravels. These curves can be used to determine the load displacement

behavior by using either the elasto-plastic or the hyperbolic model if the ultimate load and the drilled shaft diameter are known.

Table 5. Empirical load transfer curves.

Author	T-Z curve for side spring	$Q_b - Z$ curve for base spring												
API (1993)	$\tau_s = \tau_{\max} \frac{z_s}{z_c} \text{ for } z_s \leq z_c$ $\tau_s = \tau_{\max} \text{ for } z_s > z_c$	Tabulated curve <table border="1"> <thead> <tr> <th>Z_b/D</th> <th>$Q_b/Q_{b\max}$</th> </tr> </thead> <tbody> <tr> <td>0.0020</td> <td>0.25</td> </tr> <tr> <td>0.1300</td> <td>0.50</td> </tr> <tr> <td>0.0420</td> <td>0.75</td> </tr> <tr> <td>0.0730</td> <td>0.90</td> </tr> <tr> <td>0.1000</td> <td>1.00</td> </tr> </tbody> </table>	Z_b/D	$Q_b/Q_{b\max}$	0.0020	0.25	0.1300	0.50	0.0420	0.75	0.0730	0.90	0.1000	1.00
Z_b/D	$Q_b/Q_{b\max}$													
0.0020	0.25													
0.1300	0.50													
0.0420	0.75													
0.0730	0.90													
0.1000	1.00													
Vijayvergiya (1977)	$\tau_s = \tau_{\max} \left(2 \sqrt{\frac{z_s}{z_c} - \frac{z_s}{z_c}} \right) \text{ for } (z_s \leq z_c)$ $\tau_s = \tau_{\max} \text{ for } z_s > z_c$	$Q_b = Q_{b\max} \left(\frac{z_b}{z_c} \right)^{\frac{1}{3}} \text{ for } z_s \leq z_c$ $Q_b = Q_{b\max} \text{ for } z_s > z_c$												

where

- τ_s = shear stress at soil shaft interface
- τ_{\max} = maximum shear stress at soil shaft interface
- z_s = shaft segment displacement
- z_c = displacement at failure
- z_b = base displacement
- Q_b = base resistance
- $Q_{b\max}$ = ultimate base resistance

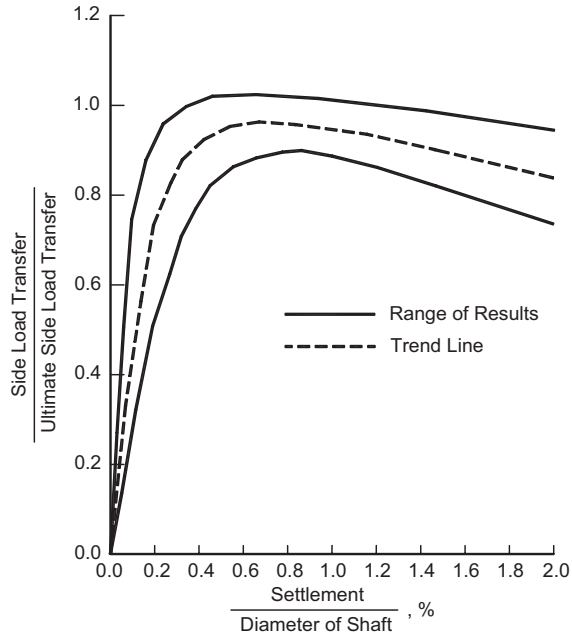


Figure 25. Normalized side load transfer for drilled shafts in cohesive soil (after O’Neill and Reese, 1999).

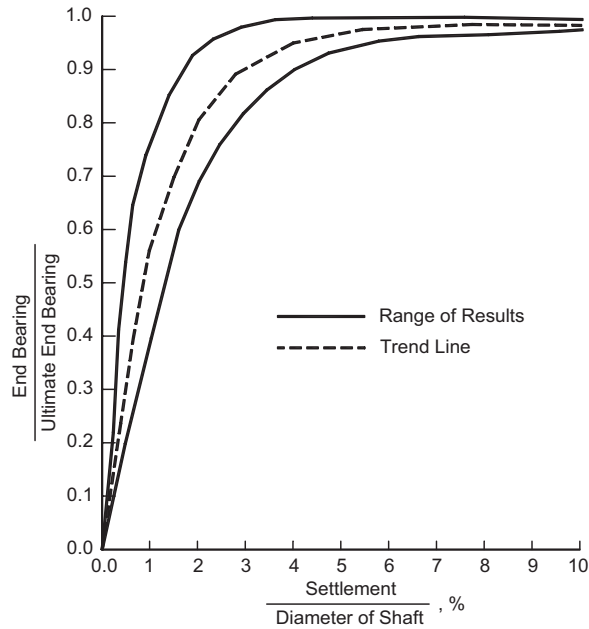


Figure 26. Normalized base load transfer for drilled shafts in cohesive soil (after O’Neill and Reese, 1999).

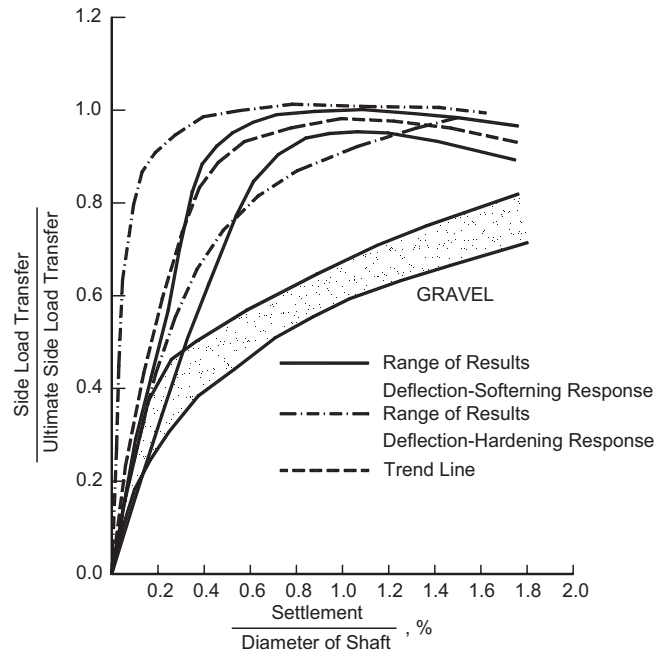


Figure 27. Normalized side load transfer for drilled shafts in cohesionless soil (after O'Neill and Reese, 1999).

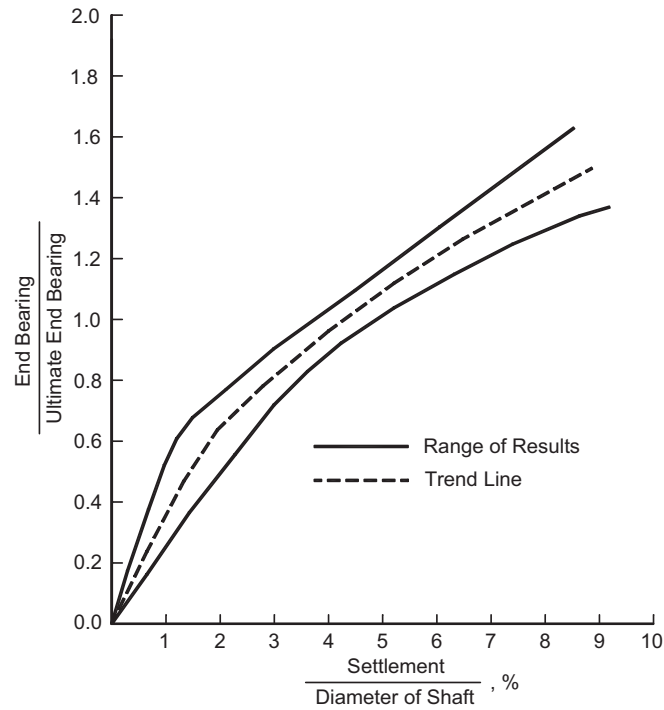


Figure 28. Normalized base load transfer for drilled shafts in cohesionless soil (after O'Neill and Reese, 1999).

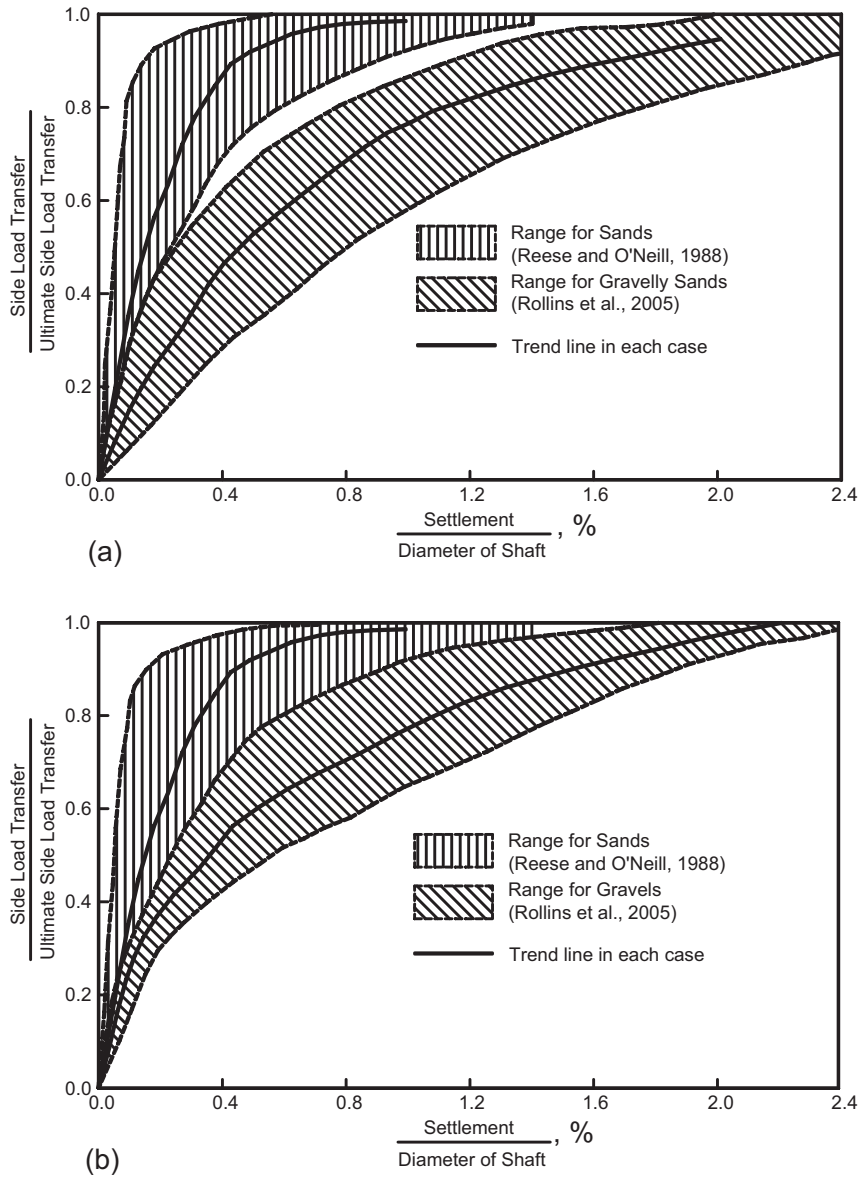


Figure 29. Normalized base load transfer for drilled shafts in cohesionless soil (after Rollins, et al., 2005).

CHAPTER 3 – STRUCTURAL CAPACITY OF DRILLED SHAFTS

3.1 AXIAL LOAD

Procedures for evaluating the structural capacity of drilled shafts by Reese and O’Neill and in ACI 318-05 are outlined in this section. For a concrete column subjected only to compressive axial load, the maximum load allowed based on ACI Section 10.3.6.2 is given by (ACI Eq. 10-2):

$$\phi P_n = \beta \phi \left[(0.85 f'_c) (A_g - A_s) + f_y A_s \right] \quad (\text{Eq. 31})$$

where

- ϕP_n = factored load applied to the column that is computed from structure analysis
- P_n = nominal strength of the column cross section
- ϕ = strength-reduction factor
- β = reduction factor to account for the possibility of small eccentricities of the axial load,
- $\beta = 0.85$ for spiral columns and $\beta = 0.8$ for tied columns
- f'_c = compressive strength of the concrete cylinder
- A_g = gross cross-sectional area of the concrete section
- A_s = cross-sectional area of the longitudinal reinforcement
- f_y = yield strength of the longitudinal reinforcement

In the case of the concentric anomalies in which the reinforcement is not embraced in concrete, the structural capacity is computed from the concrete with the anomaly alone by ignoring the capacity contribution from reinforcements for their minimal contribution due to buckling for reinforcement bars.

3.2 AXIAL LOAD AND BENDING MOMENT

In a drilled shaft with nonconcentric anomalies, the axial compressive force at a defective section will produce an eccentric moment. This reduces the axial structural capacity as a result of the interaction between the axial compressive force and the bending moment. The bending moment leads to extra flexural stresses beyond the stresses from the axial load. The interaction diagrams shown in Figure 30 can be calculated by using a series of strain distributions, each corresponding to a particular point on the axial force, P, versus the moment, M, diagram with a specific pair of axial load, P_n , and moment, M_n , (MacGregor and Wight, 2005).

The nonconcentric anomaly is assumed to have the shape shown in Figure 31. The structural capacity of this anomaly can be calculated according to ACI 318-05, by the finite element method, or by the stress strain curves for concrete and steel (O’Neill and Reese, 1999).

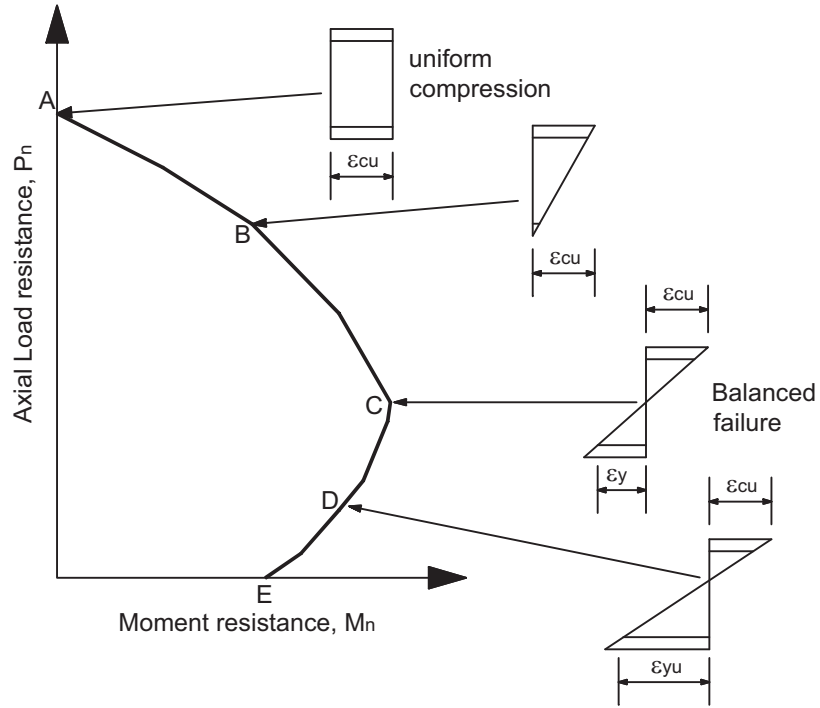


Figure 30. Strain distributions corresponding to the point on the P-M interaction diagram (McGregor and Wight, 2005).

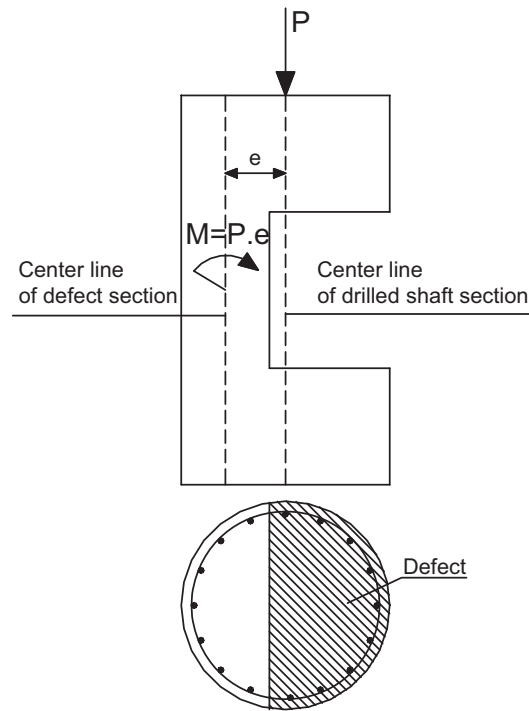


Figure 31. Nonconcentric anomaly.

The stress strain curve for concrete in Figure 32 is defined as follows:

$$f_c'' = 0.85 f_c' \quad (\text{Eq. 32})$$

$$f_c = f_c'' \left[2(\varepsilon/\varepsilon_0) - (\varepsilon/\varepsilon_0)^2 \right]; \quad \varepsilon < \varepsilon_0 \quad (\text{Eq. 33})$$

$$\varepsilon_0 = 1.7 f_c' / E_c \quad (\text{Eq. 34})$$

Young's modulus:

$$E_c = 151000 \sqrt{f_c'} \quad (\text{Eq. 35})$$

Tensile strength:

$$f_r = 19.7 \sqrt{f_c'} \quad (\text{Eq. 36})$$

where E_c , f_c' , f_c'' , and f_r are in kPa.

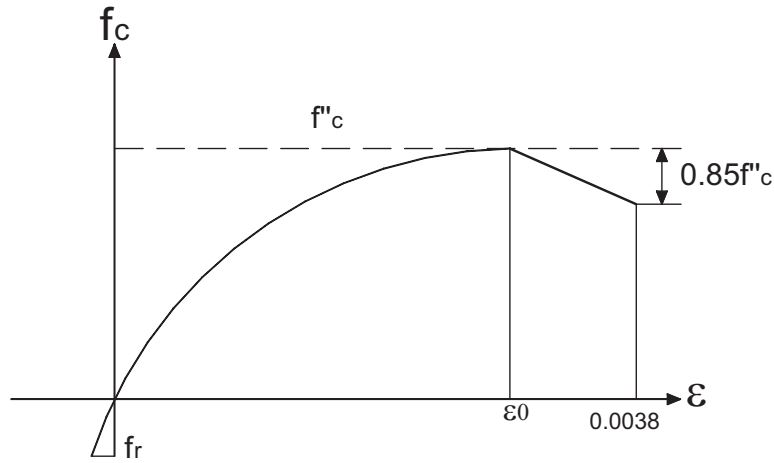


Figure 32. Stress strain curve for concrete (O'Neill and Reese, 1999).

The stress strain curve for reinforcement in Figure 33 is defined as follows:

$$\varepsilon_y = \frac{f_y}{E_y} \quad (\text{Eq. 37})$$

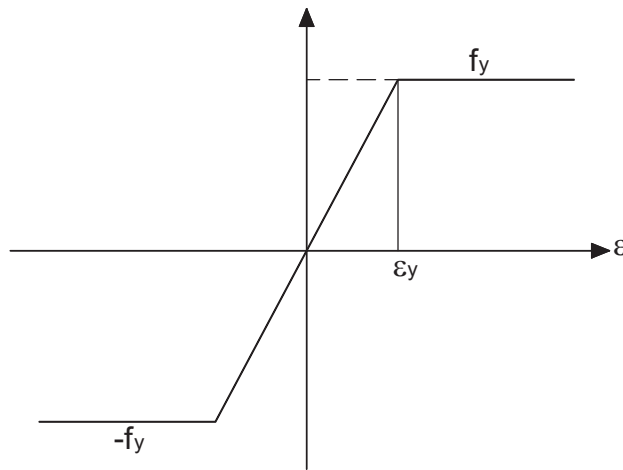


Figure 33. Stress strain curve for steel (O’Neill and Reese, 1999).

The following procedures as presented by O’Neill and Reese (1999) are used to compute the axial load and the moment on the interaction diagram:

- Cross section is divided into the finite strips shown in Figure 34.
 - Apply the rotation, r , and the axial strain, ε , representing the moment and the axial load.
 - Assume the position of the neutral axis and then the strain of each strip can be calculated by: $\varepsilon_i = \varepsilon + rd_i$, where d_i is the distance from the center of a strip to the neutral axis.
- From the value of these strains, the forces in each strip are calculated. The sum of these forces must be equal to the applied axial force. If this condition is not satisfied, the process is repeated by moving the position of the neutral axis.
- The bending moment is then computed by summing the moments from all of the normal forces from all of the strips about the neutral axis.

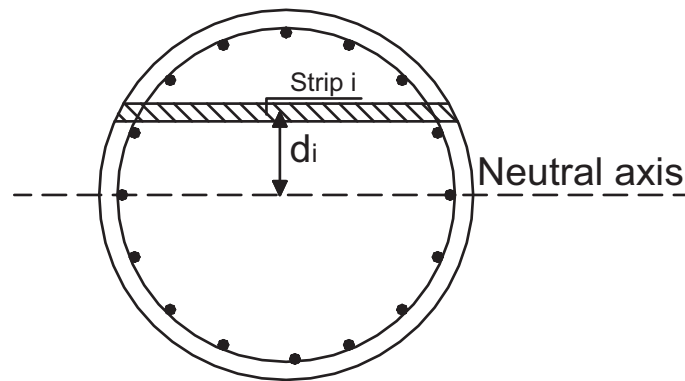


Figure 34. Finite strips of cross section.

CHAPTER 4 – PILE-SOIL INTERACTION (PSI) FINITE ELEMENT CODE

4.1 INTRODUCTION

PSI (Pile-Soil Interaction) is a 3-D finite element program for analyzing single shafts and shaft groups under vertical, lateral, torsional, and combined loads. The program was developed as a partial fulfillment of a doctoral degree requirement. The Pile-Soil system is modeled as an assemblage of solid elements. The rebar in reinforcement concrete shafts is modeled as a nonlinear bar element; concrete as an elastic, Mohr-Coulomb, or cap model material; and soils are modeled as elastic, Mohr-Coulomb, Hyperbolic, Modified Cam-Clay, Ramberg-Osgood, or cap model materials. The Pile-Soil interface is modeled by the interface element with Mohr-Coulomb or Hyperbolic models. The shaft shape can be square, circular, or H shape; and the dimensions of shafts may vary as a function of depth. The results of an analysis include deformation, stresses, axial force in nonlinear bar element, p-y curve and t-z curve at any depth along a shaft, and shear and moment distribution along the length of a shaft. The stiffness of the equivalent spring for the Pile-Soil system can be formulated from the results of analysis. After the input of geometrical dimensions, a finite element mesh is automatically generated.

4.2 FINITE ELEMENTS

Finite element types used in PSI include 6-node, 8-node, 15-node, and 20-node solid elements for modeling soil and shaft and 8-node and 16-node for modeling the interface between soil and shaft as shown in Figure 35. There are three stiffness components of an interface element: two are for shear stiffness and one for normal stiffness. For modeling the reinforcement, the nonlinear bar element is used. The program automatically creates the model with 8-node or 20-node elements for a structured mesh and 6-node or 15-node elements for an unstructured mesh.

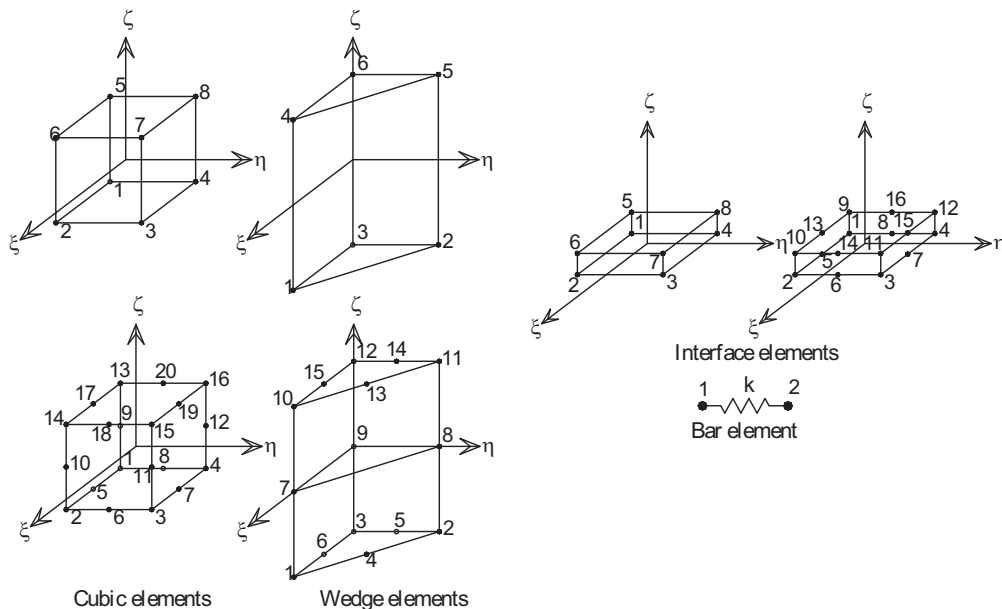


Figure 35. Finite element types.

4.3 ELASTO-PLASTIC RATE INTEGRATION OF DIFFERENTIAL PLASTICITY MODELS

Material characteristic is a critical element of numerical analysis. It can greatly influence the outcome of a numerical prediction. Many constitutive models are available to simulate the soil behavior, and selected ones are presented and implemented in PSI to investigate the model sensitivity. Generally, the associated flow rule is used, unless other wise specified, in the elasto-plasticity ratio to simplify the incremental plasticity computational process and to decrease the CPU time. According to the classical theory of plasticity, the total strain can be decomposed into elastic and plastic parts when stress state reaches yield surface:

$$\begin{aligned} \{d\varepsilon\} &= \{d\varepsilon^e\} + \{d\varepsilon^p\} \\ \{d\varepsilon^e\} &= \{d\varepsilon\} - \{d\varepsilon^p\} \end{aligned} \quad (\text{Eq. 38})$$

The Hooke's law relates the stress and elastic strain increments as follows:

$$\begin{aligned} \{d\sigma\} &= [E^e] \{d\varepsilon^e\} \\ \{d\sigma\} &= [E^e] (\{d\varepsilon\} - \{d\varepsilon^p\}) \end{aligned} \quad (\text{Eq. 39})$$

In general, the plastic strain increment is written as following the normality rule:

$$\{d\varepsilon^p\} = \lambda \left\{ \frac{\partial g}{\partial \sigma} \right\} \quad (\text{Eq. 40})$$

where λ is a scalar plastic multiplier that can be calculated by Forward Euler's method or Backward Euler's method (Smith and Griffiths, 1997) and g is the plastic potential function. According to Forward Euler's method:

$$\lambda = \frac{\left[\frac{\partial f}{\partial \sigma} \right] [E^e]}{\left[\frac{\partial f}{\partial \sigma} \right] [E^e] \left\{ \frac{\partial g}{\partial \sigma} \right\} + h} \{d\varepsilon\} \quad (\text{Eq. 41})$$

Substitute Eq. 41 and Eq. 40 to Eq. 39:

$$\{d\sigma\} = \left([E^e] - \frac{[E^e] \left\{ \frac{\partial g}{\partial \sigma} \right\} \left[\frac{\partial f}{\partial \sigma} \right] [E^e]}{\left[\frac{\partial f}{\partial \sigma} \right] [E^e] \left\{ \frac{\partial g}{\partial \sigma} \right\} + h} \right) \{d\varepsilon\} \quad (\text{Eq. 42})$$

According to Backward Euler's method:

$$\lambda = \frac{f_{(\sigma)}}{\left[\frac{\partial f}{\partial \sigma} \right] [E^e] \left\{ \frac{\partial g}{\partial \sigma} \right\} + h} \quad (\text{Eq. 43})$$

Substitute Eq. 43 and Eq. 40 to Eq. 39:

$$\{d\sigma\} = [E^e] \{d\varepsilon\} - \frac{f_{(\sigma)} [E^e] \left\{ \frac{\partial g}{\partial \sigma} \right\}}{\left[\frac{\partial f}{\partial \sigma} \right] [E^e] \left\{ \frac{\partial g}{\partial \sigma} \right\} + h} \quad (\text{Eq. 44})$$

where f is yield function, g is plastic potential function, and h denotes the hardening parameter that equals to zero for perfectly-plastic materials and constant for an elasto-plastic material with a linear hardening model.

4.4 CONSTITUTIVE MODELS OF SOILS

Six different constitutive models are implemented in PSI, and their use is strictly at the discretion of a user. Two of six models, besides the elastic model, are outlined in the subsequent sections.

4.4.1 Mohr-Coulomb Model

Mohr-Coulomb is the first failure criterion which considered the effects of stresses on the strength of soil. The failure occurs when the state of stresses at any point in the material satisfies the equation below, Chen and Mizuno (1990):

$$|\tau| + \sigma \tan \varphi - c = 0 \quad (\text{Eq. 45})$$

where φ and c denote the cohesion and friction angle, respectively. The Mohr-Coulomb criterion can be written in terms of principal stress components (Chen and Mizuno, 1990):

$$\frac{1}{2}(\sigma_1 - \sigma_3) = -\frac{1}{2}(\sigma_1 + \sigma_3) \sin \varphi + c \cos \varphi \quad (\text{Eq. 46})$$

The full Mohr-Coulomb (MC) yield criterion takes the form of a hexagonal cone in the principal stress space as shown in Figure 36. The invariant form of this criterion (Smith and Griffiths, 1997) is as follows:

$$f_1 = \frac{I_1}{3} \sin \varphi - \sqrt{\frac{J_2}{3}} \sin \theta \sin \varphi + \sqrt{J_2} \cos \theta - c \cos \varphi \quad (\text{Eq. 47})$$

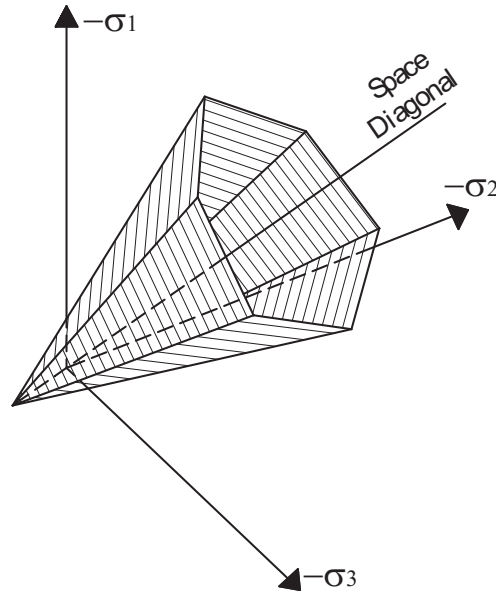


Figure 36. Mohr-Coulomb failure criteria.

In addition to the yield functions, the plastic potential function, the same form as yield function, is defined for the Mohr-Coulomb model by replacing the friction angle, φ , with the dilatancy angle, ψ , in the yield function. The plastic potential function takes the following form:

$$g = \frac{I_1}{3} \sin \psi - \sqrt{\frac{J_2}{3}} \sin \theta \sin \psi + \sqrt{J_2} \cos \theta - c \cos \psi \quad (\text{Eq. 48})$$

The dilatancy angle, ψ , is required to model dilative plastic volumetric strain increments as actually observed in dense soils. In reality, soil can sustain no or small tensile stress. This behavior can be specified as tension cut-off. The functions of tension cut-off are:

$$f_2 = \sigma_3 - T; f_3 = \sigma_2 - T; f_4 = \sigma_1 - T \quad (\text{Eq. 49})$$

where T is the maximum tensile stress. For these three yield functions, an associated flow rule is adopted. The MC material parameters include cohesion, c ; angle of internal friction, φ ; and dilatancy angle, ψ .

4.4.2 Cap Model

The cap model is a plasticity model based on the critical-state concept and the concept of continuum mechanics. The cap model is expressed in terms of the three-dimensional state of stresses and formulated on the basis of the continuum mechanics principle (Desai and Siriwardane, 1984; Chen and Mizuno, 1990).

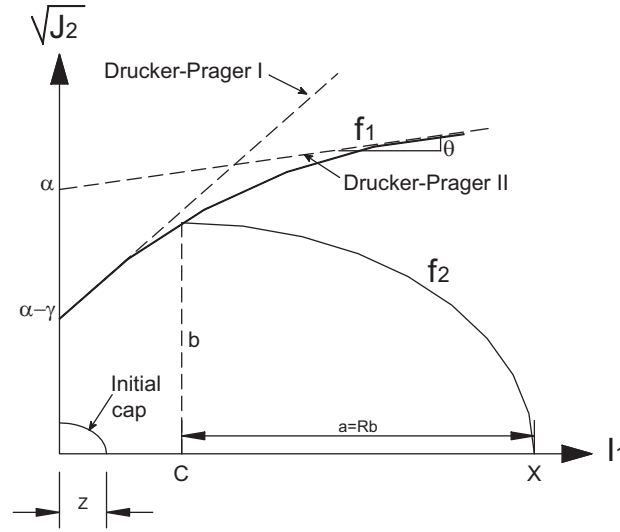


Figure 37. Yield surface for cap model (Desai and Siriwardane, 1984).

The cap model is defined by a dilative failure surface, f_1 , and a contractive yield cap surface, f_2 . The schematics of the cap model are shown in Figure 37. The expression for f_1 is given by (Desai and Siriwardane, 1984):

$$f_1 = \sqrt{J_2} + \gamma e^{-\beta I_1} - \theta I_1 - \alpha = 0 \quad (\text{Eq. 50})$$

where α , β , γ , and θ are material parameters. The quantity $(\alpha - \gamma)$ measures the cohesive strength of the material. These parameters can be determined from triaxial test (Desai and Siriwardane, 1984). During successive yielding, the material undergoes hardening behavior, represented by moving yield surfaces, f_2 . An elliptical yield cap for the cohesionless material is given in Eq. 51:

$$f_2 = R^2 J_2 + (I_1 - C)^2 - R^2 b^2 = 0 \quad (\text{Eq. 51})$$

where R = the shape factor (the ratio of the major-to-minor axis of the ellipse);
 $a = Rb = (X - C)$; X = the value of I_1 at the intersection of the yield cap and the I_1 -axis;
 C = the value of I_1 at the center of the ellipse; b = the value of $\sqrt{J_2}$ when $I_1 = C$; X = a hardening parameter that controls the change in size of the moving yield surface and the magnitude of the plastic deformation; and X = the function of the plastic volumetric strain, ϵ_v^p , as:

$$X = -\frac{1}{D} \ln \left(1 - \frac{\epsilon_v^p}{W} \right) + Z \quad (\text{Eq. 52})$$

where D , W , and Z are the material parameters, W characterizes the maximum plastic volumetric strain, D the total plastic volumetric strain rate controlling the initial loading moduli, and Z the initiation of plastic volumetric deformation under hydrostatic loading conditions or the pre-consolidation hydrostatic pressure.

4.5 ELASTO-PERFECT PLASTIC MODEL FOR BAR ELEMENT

The bar is elastic with the elastic stiffness, k , when the axial force lies between f_{\max} and f_{\min} ; and it is perfectly plastic at the axial force beyond the above limit, as shown in Figure 38.

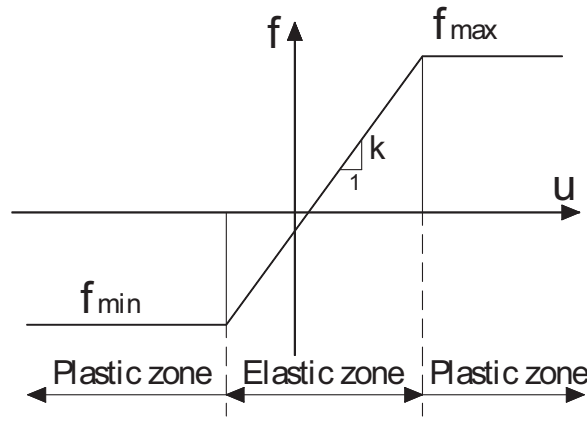


Figure 38. Nonlinear model of bar element.

4.6 CONVERGENCE CRITERIA

PSI performs an iterative solution process for nonlinear analyses. In this procedure, the system stiffness matrix is assembled once and does not change during the iteration. This saves the computation time for the structure with a large number of degrees of freedom. There are two convergence criteria, displacement and balanced load. Both criteria must be met during the computation. If either one is not met whenever the maximum allowable number of iterations is reached, the PSI solver stops running. These criteria can be expressed as:

$$\frac{\delta U^i}{U^i} 100\% \leq \varepsilon_d; \frac{\delta R^i}{R^i} 100\% \leq \varepsilon_d; \frac{\delta F^i}{F^i} 100\% \leq \varepsilon_f; \text{ and } \frac{\delta M^i}{M^i} 100\% \leq \varepsilon_f \quad (\text{Eq. 53})$$

where U^i , R^i , F^i , and M^i are accumulated transition displacements, rotation displacements, and force and moment at iteration i^{th} , respectively; δU^i , δR^i , δF^i , and δM^i are incremental transition displacements, rotation displacements, and force and moment at iteration i^{th} , respectively; and ε_d and ε_f are user defined tolerances.

4.7 PSI CALIBRATION AND VALIDATION

4.7.1 Case histories for calibration

The accuracy of PSI has been tested by carrying out the analyses of problems or back-analysis of full-scale shaft test by other open or commercial computer codes such as OPENSEES, ABAQUS, PLAXIS, and ANSYS.

Case Study 1: Full-Scale Single Shaft Under Vertical Load

This study has heavily referenced the study on validation and verification of the PLAXIS program (Brinkgreve, 2004). In this document, the full-scale single shaft under vertical load has been analyzed. The same shaft was analyzed by PSI and the results compared to the results using PLAXIS 2D, PLAXIS 3D FOUNDATION, and measured performance.

The shaft with 1.3 m diameter and 9.5 m length is constructed in overconsolidation clay. The parameters of soil profile are shown in Table 6. The loading system includes two hydraulic jacks, one reaction beam, and sixteen anchors supporting the reaction beam. In the PSI analysis, 20-node cubic elements are used. Because of the symmetric condition, only one-fourth of the Pile-Soil system is modeled and analyzed as shown in Figure 39. One-fourth of the soil volume is 25-m by 25-m and 16-m deep. The vertical load at the shaft top is modeled by the equivalent joint loads. The concrete shaft properties used in the linear elastic model are: Young's modulus $E = 3 \times 10^7$ kPa, Poisson's ratio $\nu = 0.2$, and unit weight $\gamma = 24$ kN/m³. Three coefficients of earth pressure values are considered: 1) $K_0 = 1 - \sin \varphi = 0.62$, 2) $K_0 = \nu / (1 - \nu) = 0.43$, and 3) $K_0 = 0.8$ for overconsolidation clay and other soil properties as shown in Table 6.

Table 6. Material parameter for soil data (Brinkgreve, 2004)

Parameter	Value	Unit
Material model	Mohr-Coulomb	-
Type of material behavior	Drained	-
Gravity, γ_s	20	kN/m ³
Young's modulus, E_s	60000	kPa
Poisson's ratio, ν	0.3	-
Cohesion, c	20	kPa
Friction angle, φ	22.7	deg.
Dilatancy angle, ψ	0	deg.

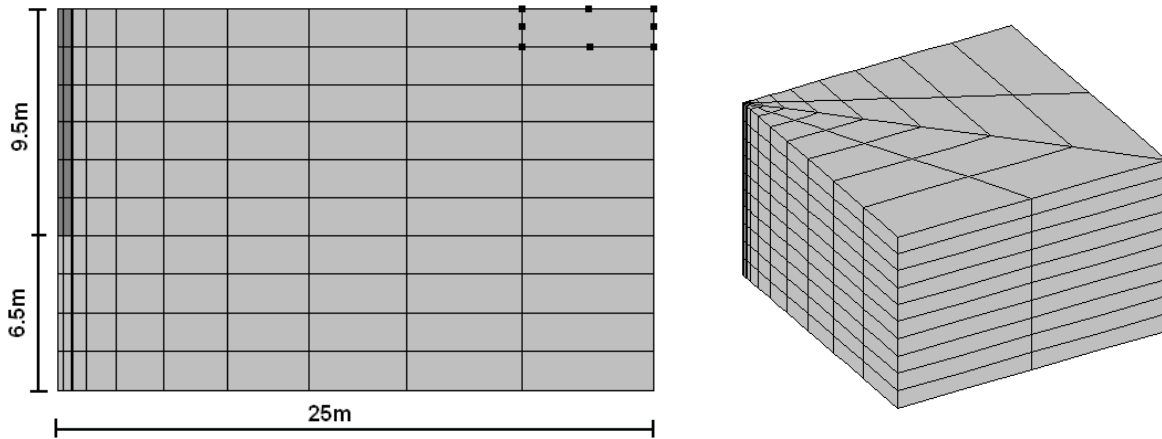


Figure 39. Side view and 3D view of finite element mesh.

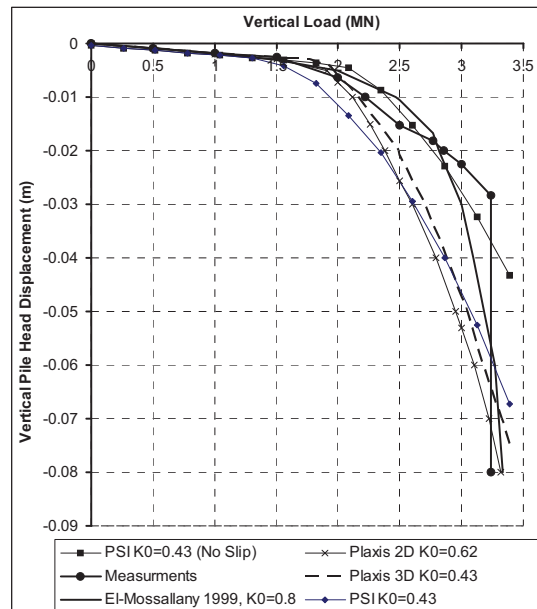


Figure 40. Comparison between PSI, PLAXIS, BEM, and test results.

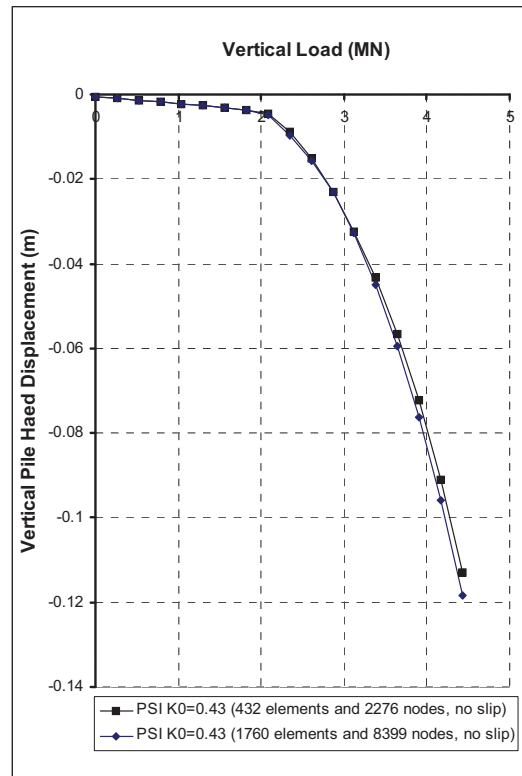


Figure 41. Effect of finite element mesh size on load-displacement curves.

The load-settlement curves are shown in Figure 40. Under a load of 1500 kN, the results of all numerical analyses agree well with test results. At a higher load, however, the results begin to vary depending on the initial stresses and the soil shaft interface. Figure 40 shows that the PSI analysis is close to the PLAXIS 3D analysis but stiffer than the PLAXIS 2D at the same initial condition ($K_0 = 0.43$) with the soil shaft interface. The PSI analysis with no soil shaft interface slip permitted gives the best agreement with the test results.

To assess the mesh density effect, two finite element mesh cases with a different number of elements and nodes were used, and the difference was not significant as shown in Figure 41.

Case Study 2: Colorado DOT Drilled shafts for Noise and Sound Barriers

The lateral load test on a drilled shaft (Shaft #1) used to support noise and walls was performed, Report No. CDOT-DTD-R-2004-8. The diameter of the tested shaft was 0.762 m (2.5 ft); length was 4.096 m (20 ft); and the distance from the shaft top to the ground surface was 1.42 m (437 ft). Two simulations were performed using (1) the soil properties from the triaxial test results and (2) the soil properties adjusted for achieving the best match between the FEM predictions and the test data. The commercially available finite element code, ABAQUS, was used to simulate the lateral shaft load test in CDOT's research.

The same material parameters were used in the PSI analyses. No attempt using PSI was made to achieve the best match. Both programs use the Mohr-Coulomb soil model with some differences: in ABAQUS, the hardening rule is considered in which cohesion depends on the plastic strain; in PSI, cohesion is defined at the zero plastic strain. The soil properties are shown in Table 7 and Table 8. The elastic Young’s modulus of shaft is selected as 34.5×10^6 kPa (5000 ksi), and Poisson’s ratio is 0.2.

Figure 42 shows the PSI finite element mesh for only one-half of the soil shaft system for symmetry. The upper part and around the shaft surface of the model is meshed finer than the lower part to get better results for the lateral load analysis.

Table 7. Soil parameters from triaxial test results.

Layers (m)	Young’s modulus (kPa)	Cohesion (kPa)
0-0.762	28579.7	71.45
0.762-1.370	22919.0	53.85
1.370-1.980	22919.0	53.85
1.980-3.050	11142.0	47.63
3.050-3.810	54444.0	253.00
3.810-4.580	23982.0	253.00

Table 8. Adjusted soil parameters for match case.

Layers (m)	Young’s modulus (kPa)	Cohesion (kPa)
0-0.762	149691.40	62.13
0.762-1.370	149691.40	48.32
1.370-1.980	149691.40	48.32
1.980-3.050	149691.40	48.32
3.050-3.810	47405.04	342.00
3.810-4.580	47405.04	41.40

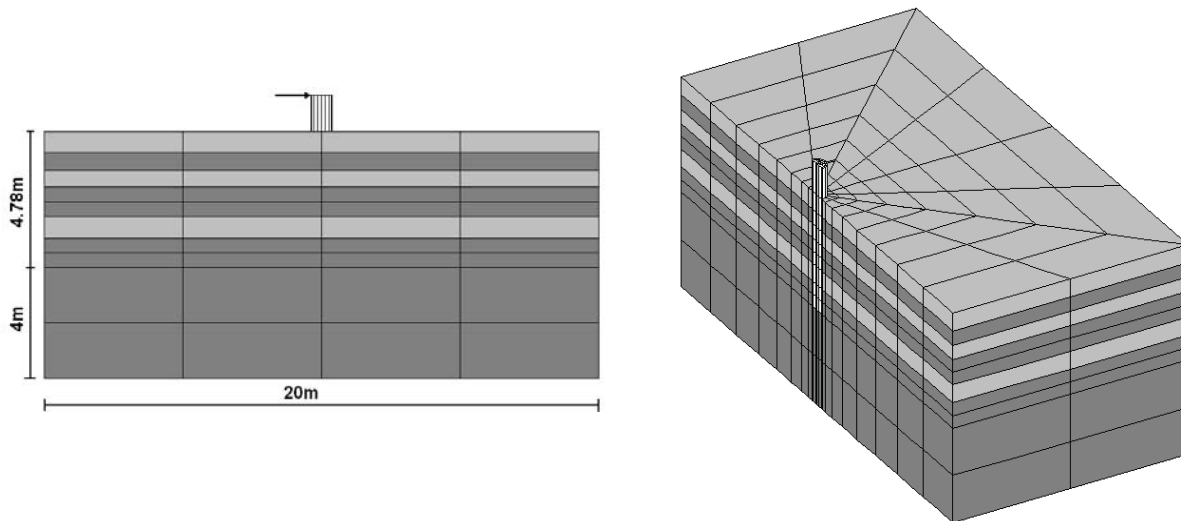


Figure 42. Side view and 3D view of finite element mesh.

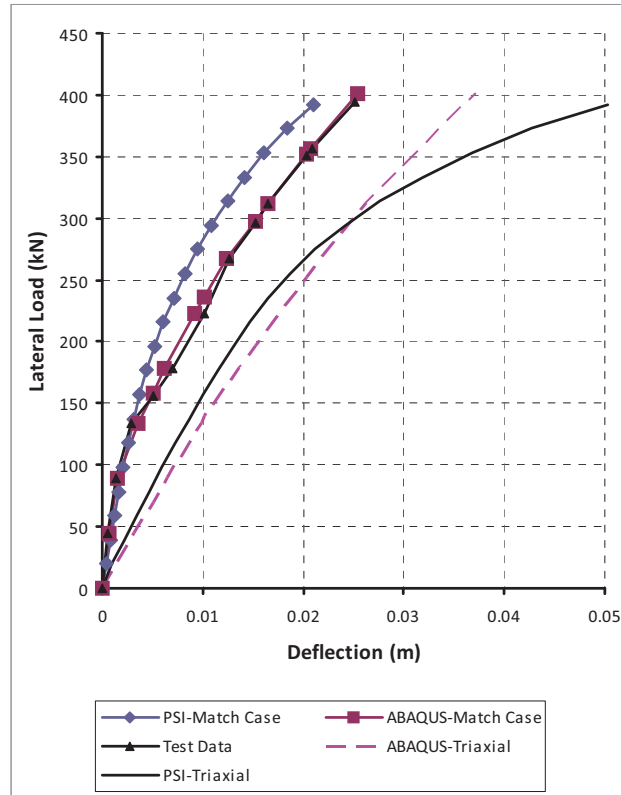


Figure 43. Comparison of the result between PSI, ABAQUS, and test data.

When the triaxial test results were used, both the ABAQUS and PSI analyses showed softer behavior. When the best matched parameters for the ABAQUS were used, the PSI analysis shows a slightly stiffer behavior. In general, the PSI results agreed well with the ABAQUS results as shown in Figure 43.

Case Study 3: Socketed Shaft in Homogeneous Soil

The model of socketed shaft in homogeneous soil shown in Figure 44 was used in the verification of the 3-D ANSYS finite element code (Brown, et al., 2001). In the ANSYS analysis, the shaft and soil were modeled using 8-node cubic elements; a 3-D point-to-surface contact element was used to model the Pile-Soil interface. In the PSI analysis, soil and shaft are modeled by 20-node cubic elements. Soil properties are shown in Table 9. The shaft configuration in Figure 44 is used in the ANSYS and PSI analyses. The behavior of shaft is assumed elastic, with Young's modulus $E = 2 \times 10^7$ kPa and Poisson's ratio $\nu = 0.3$. The soil model in the PSI analysis is the Mohr-Coulomb or the cap model with no cap effect similar to the Drucker-Prager model in the ANSYS analysis. Only the failure envelope parameter, α , and the failure envelope linear coefficient, θ , are considered in the cap model. The lateral load and displacement curves are shown in Figure 45. The PSI analyses using the Mohr-Coulomb and the cap models and the ANSYS using the Drucker-Prager model give nearly identical results.

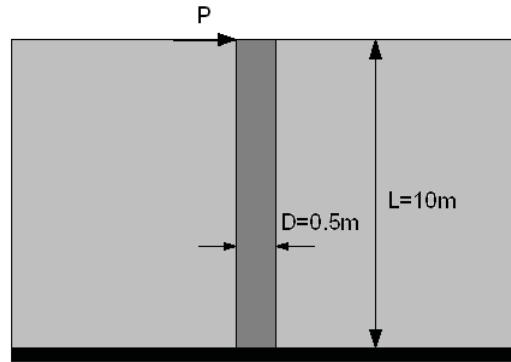


Figure 44. Socketed shaft (Brown, et al., 2001).

Table 9. Material parameter for soil data (Brown, et al., 2001).

Parameter	Value	Unit
Material model	Mohr-Coulomb, cap	-
Type of material behavior	Drained	-
Soil submerged unit weight, γ_s	11.8	kN/m ³
Young's modulus, E_s	20000	kPa
Poisson's ratio, ν	0.45	-
Cohesion, c (For the Mohr-Coulomb model)	34	kPa
Friction angle, ϕ (For the Mohr-Coulomb model)	142	deg.
Dilatancy angle, ψ (For the Mohr-Coulomb model)	142	deg.
Failure envelope parameter, α (For the cap model)	41.6	kPa
Failure envelope linear coefficient, θ (For the cap model)	0.1207	-

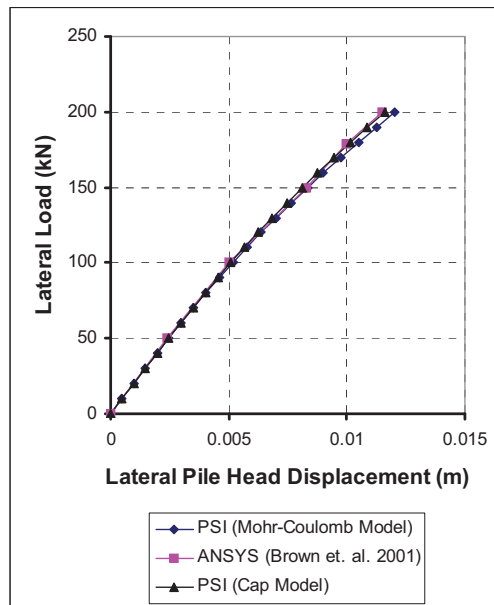


Figure 45. Comparison of shaft head displacement for single socketed shaft.

Case Study 4: Single Shaft under Vertical Load

The PSI analysis was carried out on the single shaft under vertical load. The shaft was installed and tested near the University of California, Berkeley, campus. The analysis was performed by Wang and Sita (2004) using OPENSEES. The 0.762-m (2.5-feet) diameter circular cast-in-place shaft was embedded to a depth of 5.79 m (19 feet). The soil was hard to stiff sandy clay, medium dense sandy silt, and dense clayey sand. Above the depth of about 2.2 m, soil was overconsolidation. Below 4-m deep, the undrained shear strength varied linearly with depth; and the estimated coefficient of earth pressure at rest K_0 , was 0.5. The undrained shear strength and the coefficient of earth pressure at rest vary from the 2.2-m deep to the ground surface as shown in Figure 46. For the homogeneous soil profile analysis, the undrained shear strength was the averaged undrained shear strength over the shaft length plus one shaft diameter and the coefficient of earth pressure at rest K_0 assigned to be equal to 0.5. Homogeneous soil properties were: Young’s modulus 10^5 kPa, Poisson’s ratio 0.49, total unit weight 19.62 kN/m^3 , and undrained shear strength 84 kPa. The shaft was modeled elastic with Young’s modulus $E = 20 \times 10^6$ kPa and Poisson’s ratio $\nu = 0.1$.

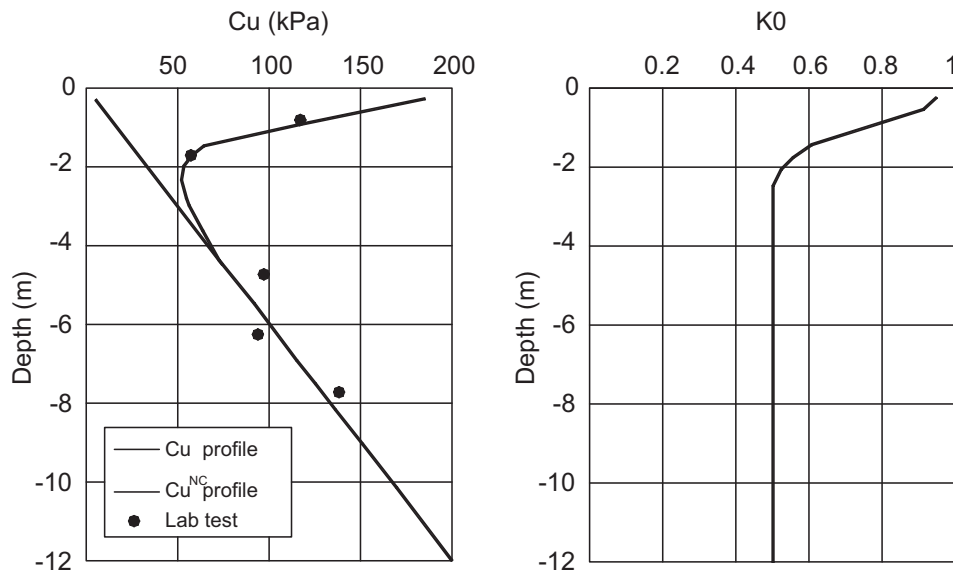


Figure 46. C_u and K_0 profiles (Wang and Sita, 2004).

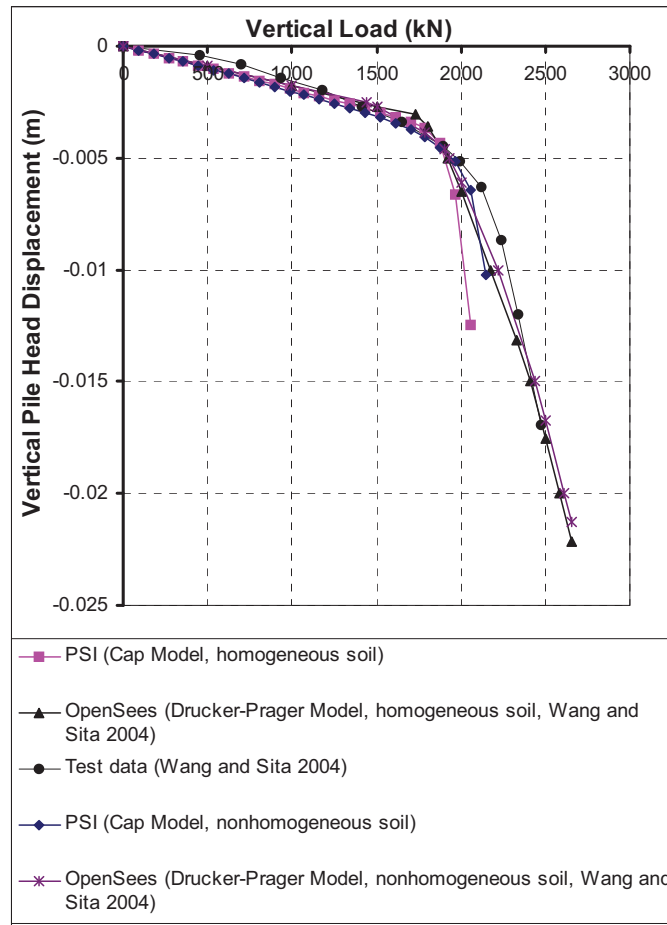


Figure 47. Comparison of the result between PSI, OPENSEES, and test data.

As shown in Figure 47, all analysis results using PSI and OPENSEES show an excellent agreement with the measured performance of the single shaft under a vertical load.

Summary and conclusions

A nonlinear finite element analysis computer code, named **PSI (Pile-Soil Interaction)**, was developed in the Center for Geotechnical Engineering Science (CGES) at the University of Colorado at Denver and Health Sciences Center for the analysis of single shafts and shaft groups under all load types singularly or combined, static or dynamic. Six different soil models and two different concrete models are implemented for the convenience of users. The PSI code was developed with the user friendly concept in mind. To assess the validity of PSI, the single shaft performances under vertical or lateral load from four different case studies were analyzed using PSI. The PSI results were compared to the measured load test results and analysis of the results using PLAXIS 2D, PLAXIS 3D, ANSYS, and ABAQUS.

- Good agreements were achieved between the PSI results and the measured shaft-load test results under vertical or lateral load conducted at the Colorado DOT (Jamal Nusairat, et al., 2004); Brinkgreve (2004); and UC Berkeley (Wang, et al., 2004).
- Good agreements were also achieved between the PSI results and the analysis results using PLAXIS 2D, PLAXIS 3D, ABAQUS, and ANASYS by the authors cited in the article.
- The above agreement indicates that the **PSI code** is effective in assessment of single shaft performance under vertical and/or lateral loads.

The subsequent development tasks will include: the comparison with further measurements and LSHAFT results, the analysis of shafts under different loads singularly or combined, the static and dynamic analyses of single or shaft groups, and assessment of group efficiency. CGES is also embarking on the development of the nonlinear SSI Finite Element Analysis Code (Soil-Structure Interaction) for the analysis of soil-structure interaction analysis of high-rise buildings under static and dynamic loads.

4.7.2 Comparative study between PSI and LS-DYNA codes

The finite element code PSI was used exclusively in the research on the effect of anomalies on drilled shaft capacities. To ensure that results produced by PSI are reasonable, selected cases were analyzed by both the PSI and the LS-DYNA codes. The latter code was initially developed at the Lawrence Livermore National Laboratory. Its commercial version has been available for many years. Numerical static shaft-load tests were performed in this comparative study. The dimensions of the finite element model are shown in Figure 48. It is assumed that the shaft-load test exhibits an axisymmetric condition, hence only a quarter of the model about the central axis was analyzed. Boundary conditions of the model are also shown in Figure 48. In order to reduce the discrepancy in the analytical results, the finite element mesh (see Figure 49) for the load test model was kept identical in both PSI and LS-DYNA. In addition to the finite element mesh, material parameters for the concrete shaft and soil were also kept the same. Throughout the entire comparative study, the concrete shaft was simulated by the cap material model. For different cases, soil was simulated either by the elastic model or the cap material model. Table 9 summarizes the material parameters used in the comparative study.

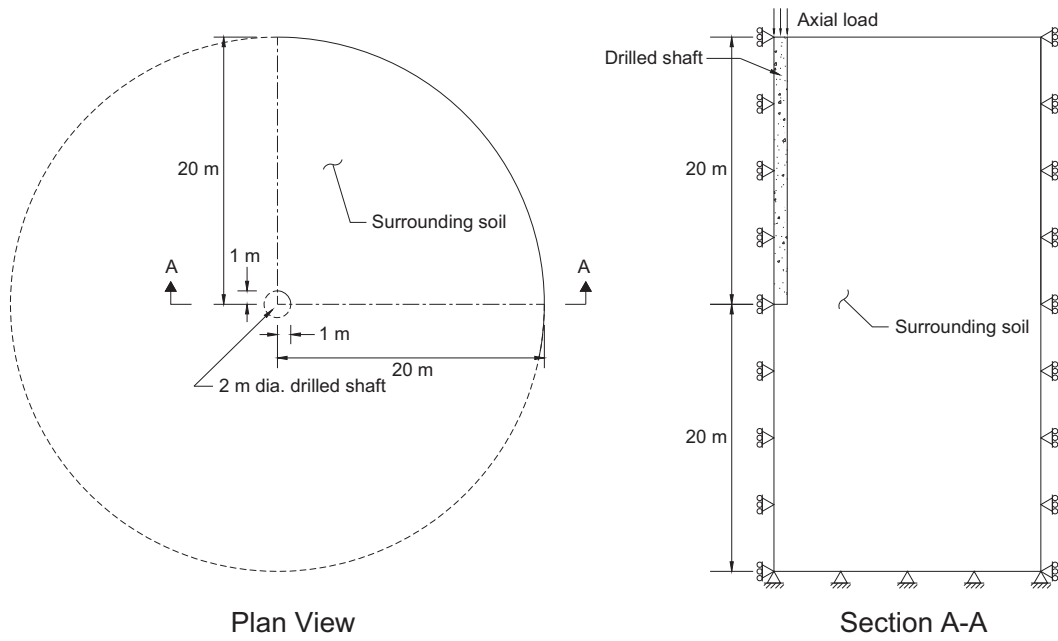
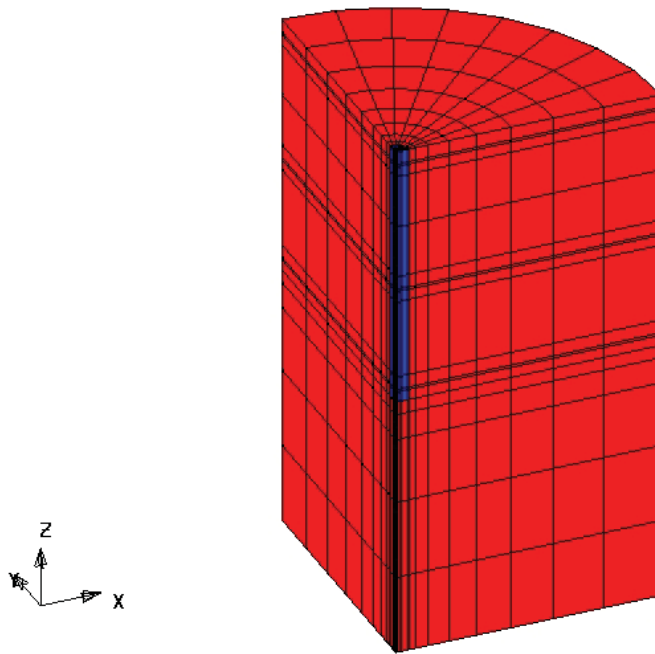


Figure 48. Schematics of numerical shaft-load test.



ETA/VPG

Figure 49. Finite element mesh for the numerical shaft-load test (axisymmetric condition).

Table 10. Material parameters used in the comparative study.

Material Parameter	Concrete	Soil	
	Cap model	Elastic model	Cap model
Density, ρ (kg/m ³)	2250	1719	1719
Bulk modulus, K (MPa)	11961.8	209	209
Shear modulus, G (MPa)	8971.3	40.4	40.4
Failure envelope parameter, α (kPa)	10021	-	0
Failure envelope linear coefficient, θ	0.0928	-	0.2815
Failure envelope exponential coefficient, γ (kPa)	0	-	0
Failure envelope exponent, β (kPa) ⁻¹	2.35E-07	-	0
Cap surface axis ratio, R	2.3	-	1.6
Hardening law exponent, D (kPa) ⁻¹	1.77E-07	-	4.00E-04
Hardening law coefficient, W	0.1	-	0.00791
Hardening law exponent, X _o (kPa)	0	-	Varies

The concrete material is assumed to have a compressive strength (f_c) of 20.7 MPa (3000 lb/in²). The modulus of elasticity of concrete (E) was determined to be 21,531 MPa using $E = 4732.4 \sqrt{f_c}$ MPa with $f_c = 20.7$ MPa ($E = 57,000 \sqrt{f_c}$ psi with $f_c = 3000$ lb/in²). The bulk modulus (K) and shear modulus (G) for concrete shown in Table 10 were determined using $E = 21,531$ MPa and an assumed Poisson's ratio $\nu = 0.2$. The stress strain curve under numerical unconfined compression test is shown in Figure 50. As for the soil, it was assumed to be a dense sand with friction angle $\phi' = 36^\circ$. Numerical triaxial compression tests under different confining pressures were performed, and the stress strain curves are shown in Figure 51. Note that the hardening law exponent X_o varies in Table 10. X_o is assumed to be related to the overburden pressure (σ_v) and lateral earth pressure (σ_h) with $X_o = \sigma_v + 2 \sigma_h$ and $\sigma_h = (1 - \sin\phi') \sigma_v$.

The first case considered examines the effect of soil models (i.e., elastic model versus cap material model). Numerical static shaft-load tests were performed with no anomalies in the shaft and with no contact interface between the shaft and the surrounding soil. The load-settlement curves from both finite element codes are presented in Figure 52. Nearly identical results are observed with the elastic soil model. Good agreement is also observed with soil simulated by the cap material model. Note that LS-DYNA produces slightly higher stiffness before yielding than the PSI in the first case. The second case examines the effect of anomaly near the top of the shaft, Figure 53, with no contact interface. The results of the second case are shown in Figure 54, where good agreement is observed. A similar trend is noted between the cases with soil modeled by the cap material model; LS-DYNA produces slightly higher stiffness when the applied load is low and shows a softer response when the load is high.

The third case examines the effect of contact interface between the shaft and soil. The input required for the contact interface for both PSI and LS-DYNA is the Coulomb friction coefficient. The friction coefficient is assumed to be equal to the value of $\tan \phi'$ ($\tan 36^\circ = 0.73$). In PSI, two additional parameters are needed in defining the contact interface, which are the normal and

shear stiffness of the contact interface. Both the normal and shear stiffness are related to the elastic properties (i.e., modulus of elasticity E and Poisson's ratio ν) of the soil. The analytical results for perfect shaft with contact interface are shown in Figure 55, where good agreement between the two codes is again observed. Consistent with the prior two cases, LS-DYNA generates higher stiffness before yielding than PSI. With the introduction of contact interface, PSI shows a distinct yield point and a soft response post-yielding (more so than LS-DYNA). Note that both PSI and LS-DYNA suggested that introduction of contact interface numerically lowers the load carrying capacity of shafts (see Figures 52 and 55).

It is concluded from this comparative study that the PSI and LS-DYNA analysis results are in good agreement in shaft capacity computation. The minor discrepancy is attributed to the constitutive modeling of soil, element formulation, and treatment of the contact interface. This comparison attests to the validity of the PSI computer code in the analysis of the shaft capacity. With more constitutive models implemented, the PSI code is considered more versatile and will be adopted in this study. In the study proposal, the GAP code developed by Summit Peak, Inc., was selected for the verification of the effectiveness of the PSI code. However, the negotiation for the right to use the GAP code was not successful; and the idea was dropped from further consideration.

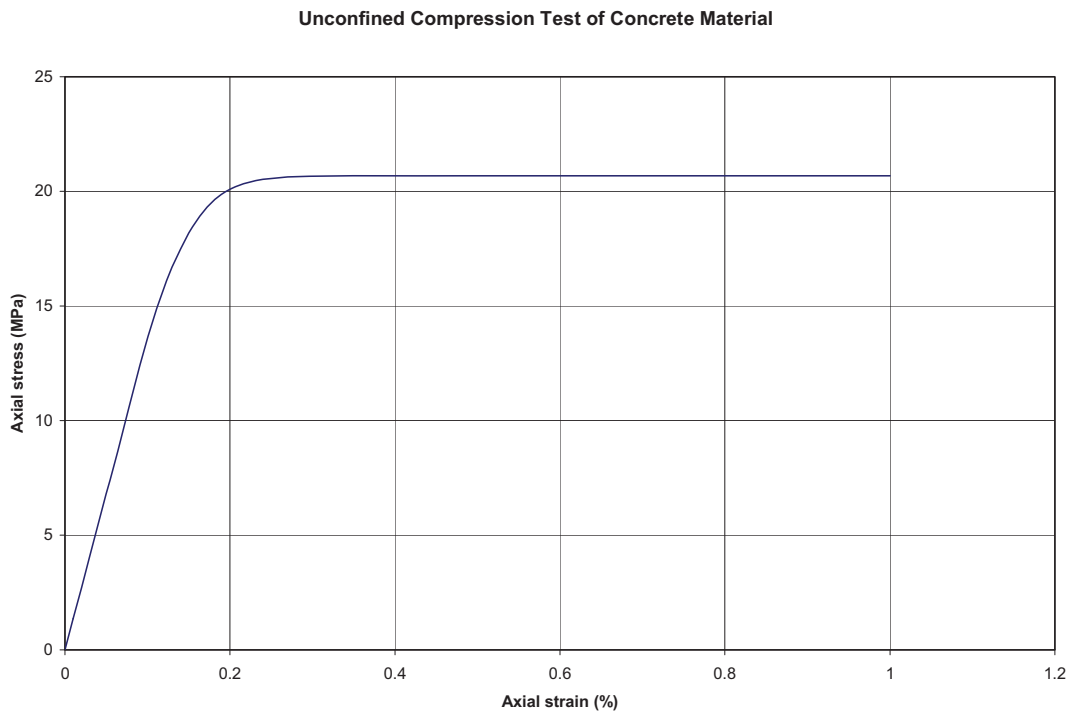


Figure 50. Numerical unconfined compression test for concrete.

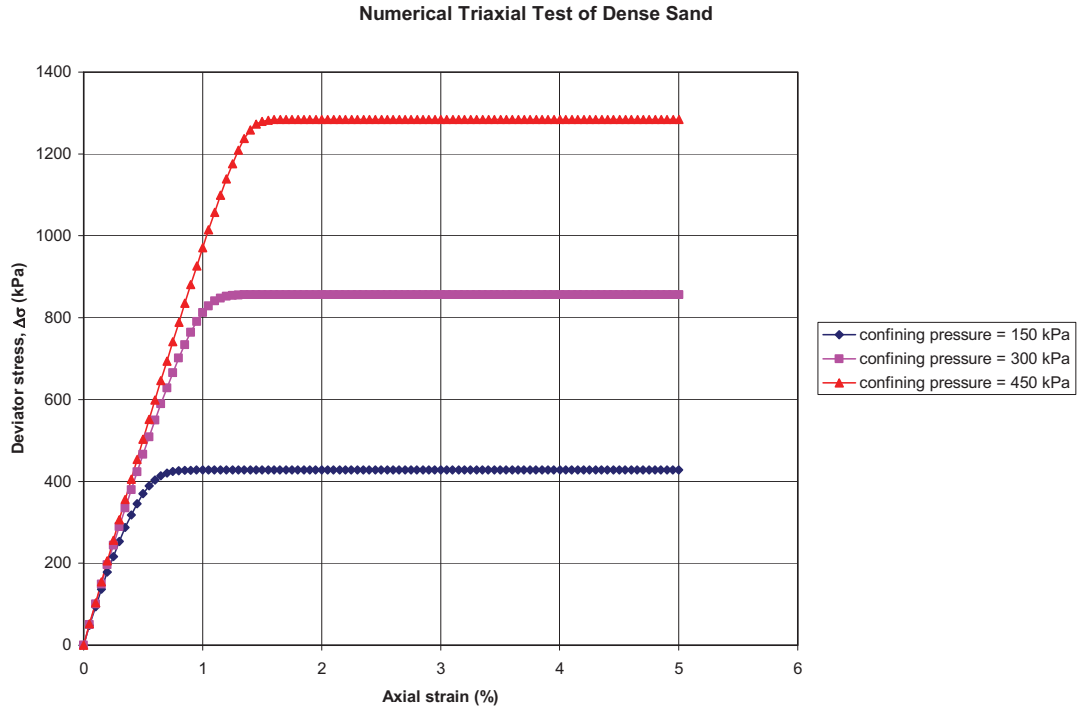


Figure 51. Numerical triaxial compression tests of sand used in the comparative study.

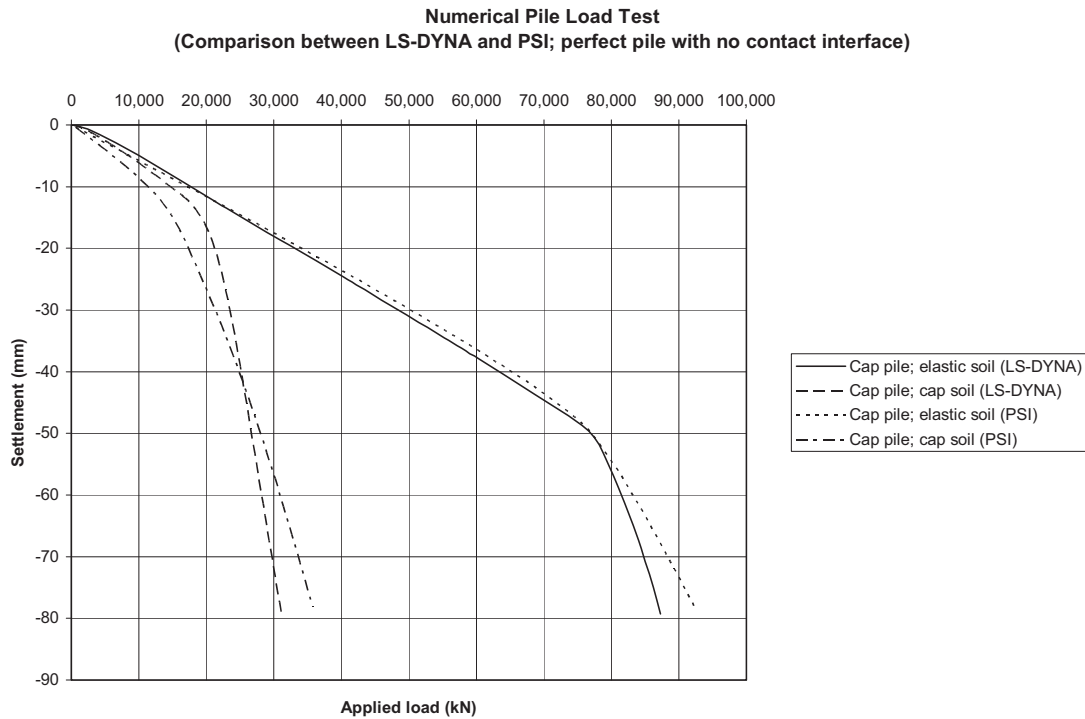


Figure 52. Numerical static shaft-load test comparison between LS-DYNA and PSI with perfect shaft and without contact interface.

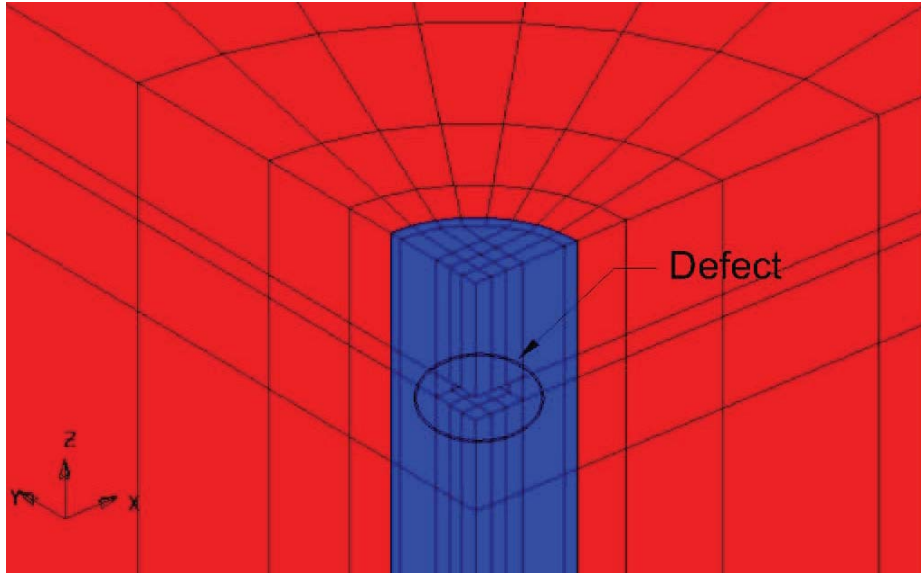


Figure 53. Location of anomaly near the shaft top.

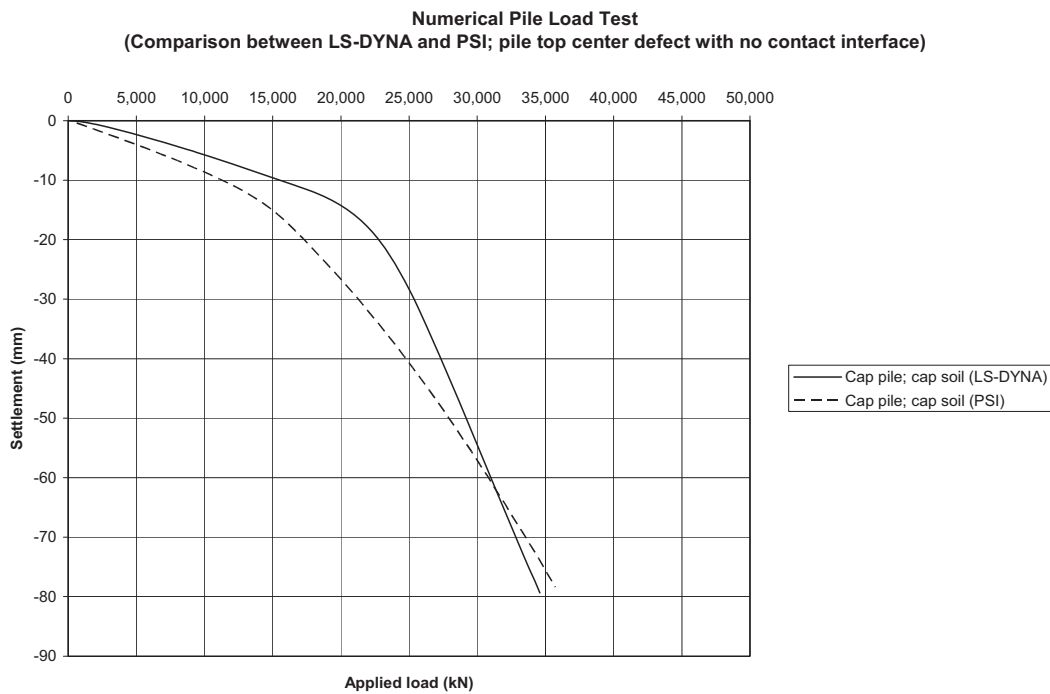


Figure 54. Numerical static shaft-load test comparison between LS-DYNA and PSI with anomaly at top of shaft and without contact interface.

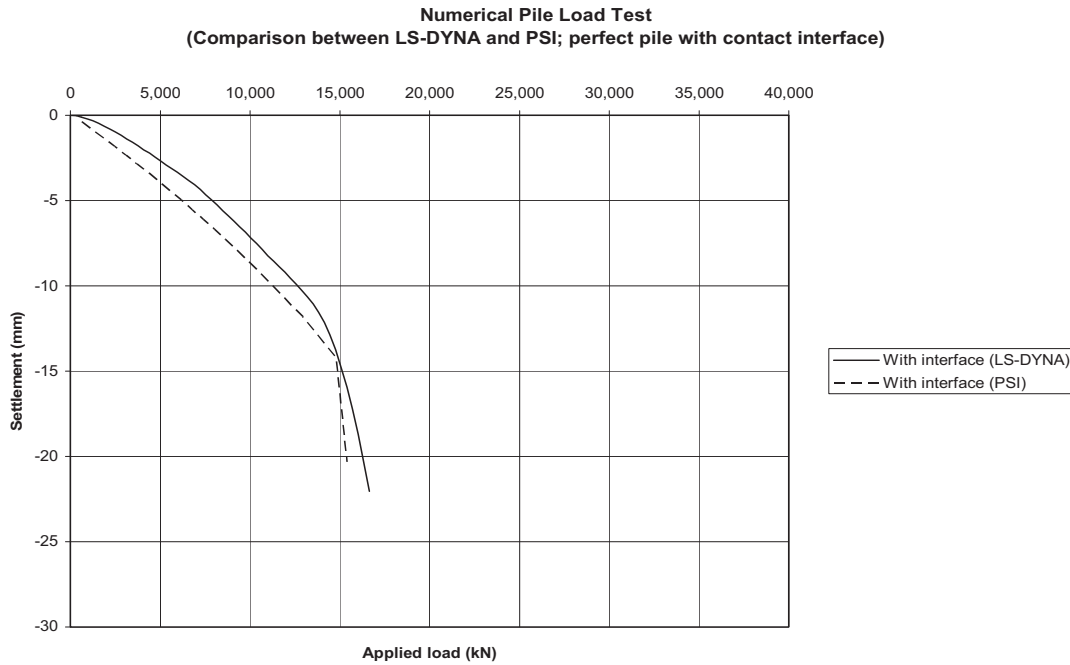


Figure 55. Numerical static shaft-load test comparison between LS-DYNA and PSI with contact interface between shaft and soil.

CHAPTER 5 – CAPACITIES OF DRILLED SHAFTS WITH ANOMALIES

Drilled shaft capacity is the lesser of two capacities: structural capacity and geotechnical capacity. The structural capacity is the drilled shaft’s material strength without the interference of foundation soils; and the geotechnical capacity involves the subsurface geological materials, soils and rocks, in supporting design loads. Typically, the structural capacity is higher than the geotechnical capacity, but not always, particularly when a drilled shaft contains anomalies. This chapter presents finite element analyses results of structural and geotechnical capacities of drilled shafts with anomalies. To incorporate the effects of various factors including subsoil types (granular and clayey soils), locations of anomalies, shaft diameters, and shapes of anomalies, nearly 400 analyses were performed as demonstrated in the later sections.

5.1. STRUCTURAL CAPACITY OF DRILLED SHAFTS

5.1.1 Concrete

Concrete strength was modeled using the Mohr-Coulomb model. This allowed the evaluation of the structural capacity of drilled shafts with anomalies. The Mohr-Coulomb material parameters for concrete are summarized in Table 11. The resulting stress strain relationship from the finite element analyses of two concrete cylinders with diameters of 1 m and 2 m and different uniaxial strengths of 20.7 and 31.1 MPa are shown in Figure 56.

Table 11. Properties of Concrete.

Number	28-day compressive strength (kPa)	Young’s modulus (kPa)	Poisson’s ratio	Mohr-Coulomb friction angle (degree)	Mohr-Coulomb cohesion (kPa)
1	20,710 (3,000 psi)	21,552,265	0.2	38	4,960
2	3,1065 (4,500 psi)	26,396,026	0.2	38	7,423

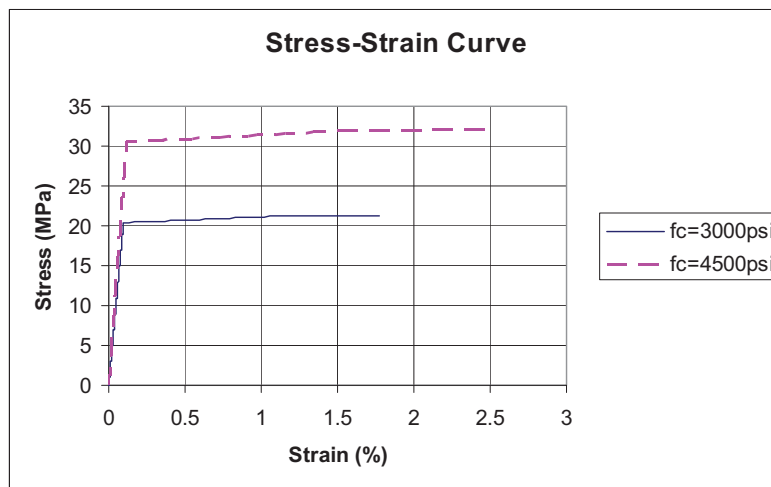


Figure 56. Stress strain curves for concrete cylinders.

5.1.2 Structural capacity of drilled shafts without anomalies via ACI Code

The structural capacities of drilled shafts with diameters of 1 m and 2 m, and a length of 20 m were evaluated using the following equations from the ACI code (ACI 318-05):

Drilled shaft with reinforcement:

$$\phi P_n = \beta \phi [0.85 f'_c (A_g - A_s) + A_s f_y] \quad (\text{Eq. 54})$$

The capacity of concrete only:

$$\phi P_n^c = \beta \phi 0.85 f'_c (A_g - A_s) \quad (\text{Eq. 55})$$

The capacity of the shaft without reinforcement:

$$P_n^c = \beta 0.85 P^c \quad (\text{Eq. 56})$$

where:

$$P^c = f'_c A_g \quad (\text{Eq. 57})$$

Additionally, finite element analyses were performed on the above four drilled shafts on rigid support (or hard rocks). The resulting load-displacement curves are shown in Figure 57 where the displacements reflect the elastic deformation of drilled shafts under load. The structural capacity of drilled shafts with 2% of reinforcement is given in Table 13, in which ϕ and β factor is rejected.

Table 12. Structural capacity of concrete without reduction.

Concrete Strength, f'_c kPa (psi)	Shaft Diameter (m)	P^c , Eq. 57 (kN)	P^c , FEM (kN)
20,710 (3,000)	2	65,062.0	64,687.14
31,065 (4500)	2	97,594.0	98,570.88
20,710 (3000)	1	16,265.5	16,017.77
31,065 (4500)	1	24,398.5	24,642.72

Table 13. Structural capacity of drilled shafts with 2% reinforcement

Concrete Strength, f'_c kPa (psi)	Shaft Diameter (m)	P_n/β (kN)
20,710 (3,000)	2	80,214
31,065 (4500)	2	107,313
20,710 (3000)	1	19,931
31,065 (4500)	1	26,708

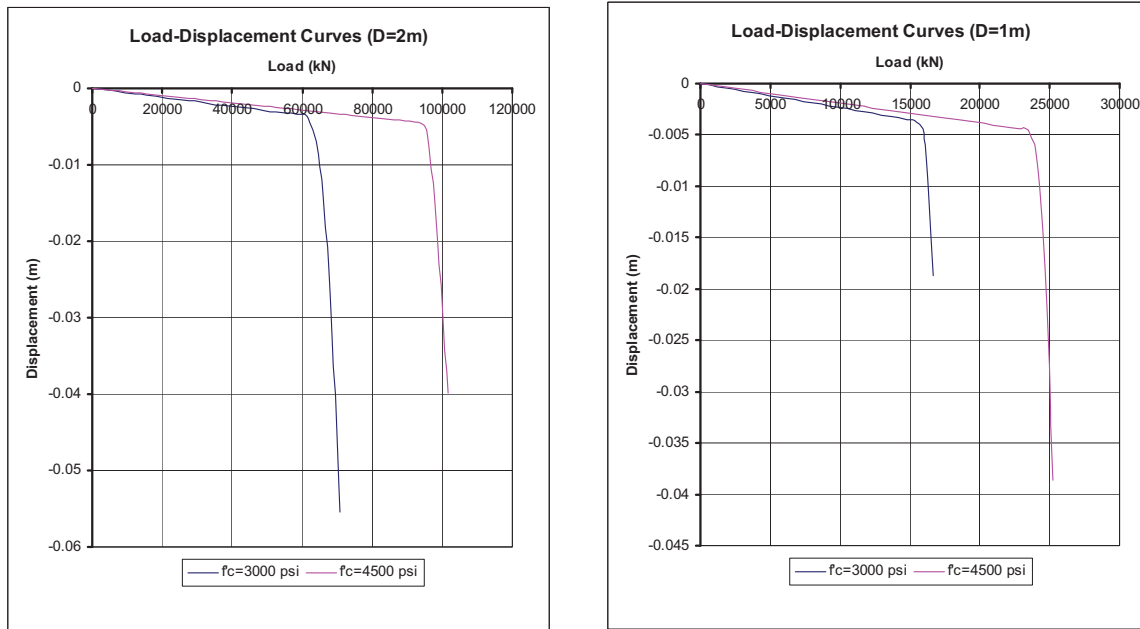


Figure 57. Load-displacement curves of four concrete drilled shafts.

5.2. STRUCTURAL CAPACITY OF DRILLED SHAFTS WITH ANOMALIES

5.2.1 Size, location, and properties of anomalies

Hypothetical drilled shafts with various sizes of anomalies located at different elevations within the shafts shown in Figure 58, Table 14, and Table 15, and their sizes and shapes are shown in Figure 59. All anomalies discussed were concentric anomalies except the last one, a nonconcentric anomaly. As discussed later, this nonconcentricity had a drastic effect on the structural capacity of a drilled shaft. The created lengths of anomalies were 0.2 m, 1 m, and 1.2 m. Table 14 summarizes the types of anomalies and the associated cross-sectional area reductions.

For the drilled shafts with neck-in types 1, 2, or 3, the reinforcements are not covered with concrete; thus their structural capacities are assumed to be the same as the drilled shafts without reinforcement. For the drilled shafts with cubic and nonconcentric anomalies, the structural capacities include the contributions from both concrete and 2% reinforcement; but only the reinforcement covered by concrete in nonconcentric anomalies was considered.

Table 14. Anomaly sizes.

Shaft Diameter (m)	Shape	Area (m²)	Reduction of Cross Section (%)
2	Cubic 0.93 x 0.93	0.865	27.5
2	Cylinder R _d = 0.88	2.430	77.3
2	Neck-in type 1	2.440	77.3
2	Neck-in type 2	2.760	87.7
2	Neck-in type 3	3.050	96.7
2	Nonconcentric	2.440	77.3
1	Cubic 0.465 x 0.465	0.216	27.5
1	Cylinder R _d = 0.44	0.604	77.3
1	Neck-in type 1	0.610	77.3
1	Neck-in type 2	0.690	87.7
1	Neck-in type 3	0.763	96.7
1	Nonconcentric	0.604	77.3

Table 15. Anomaly locations.

Number	Depth (m)
1	1
2	11
3	19

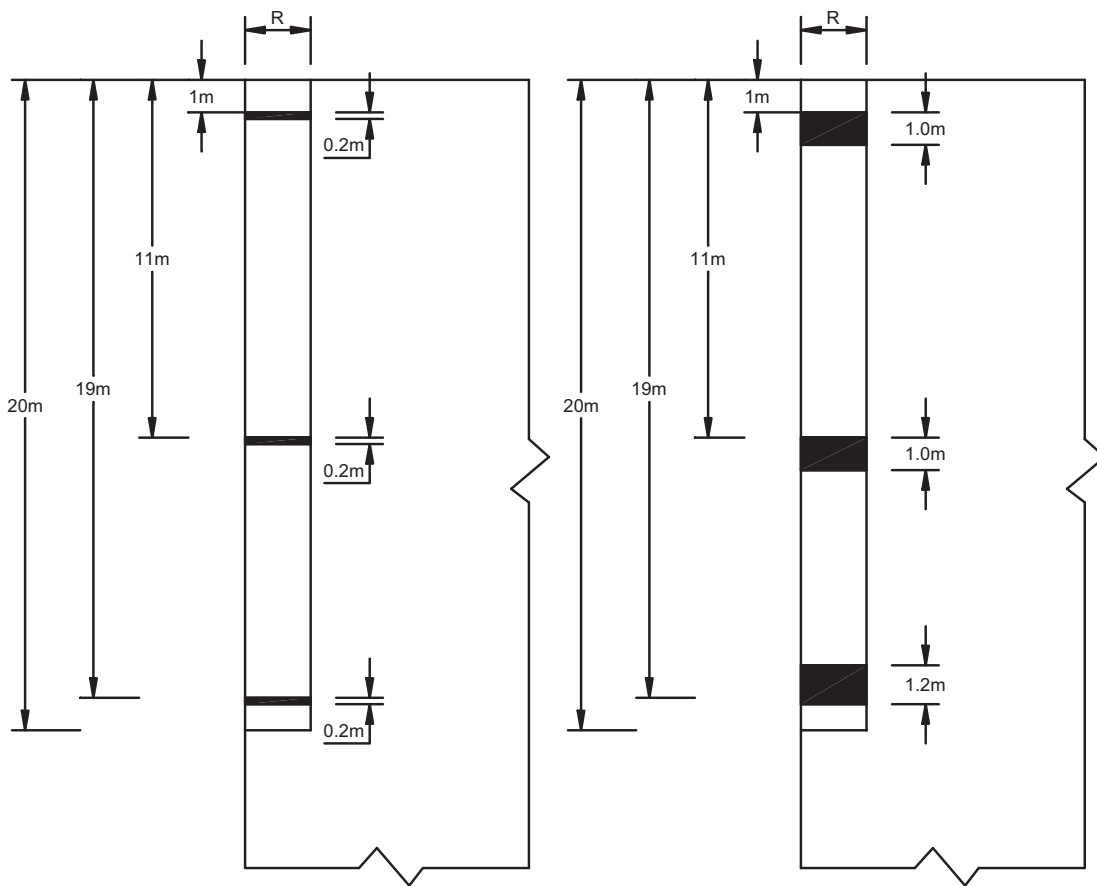


Figure 58. Anomaly locations.

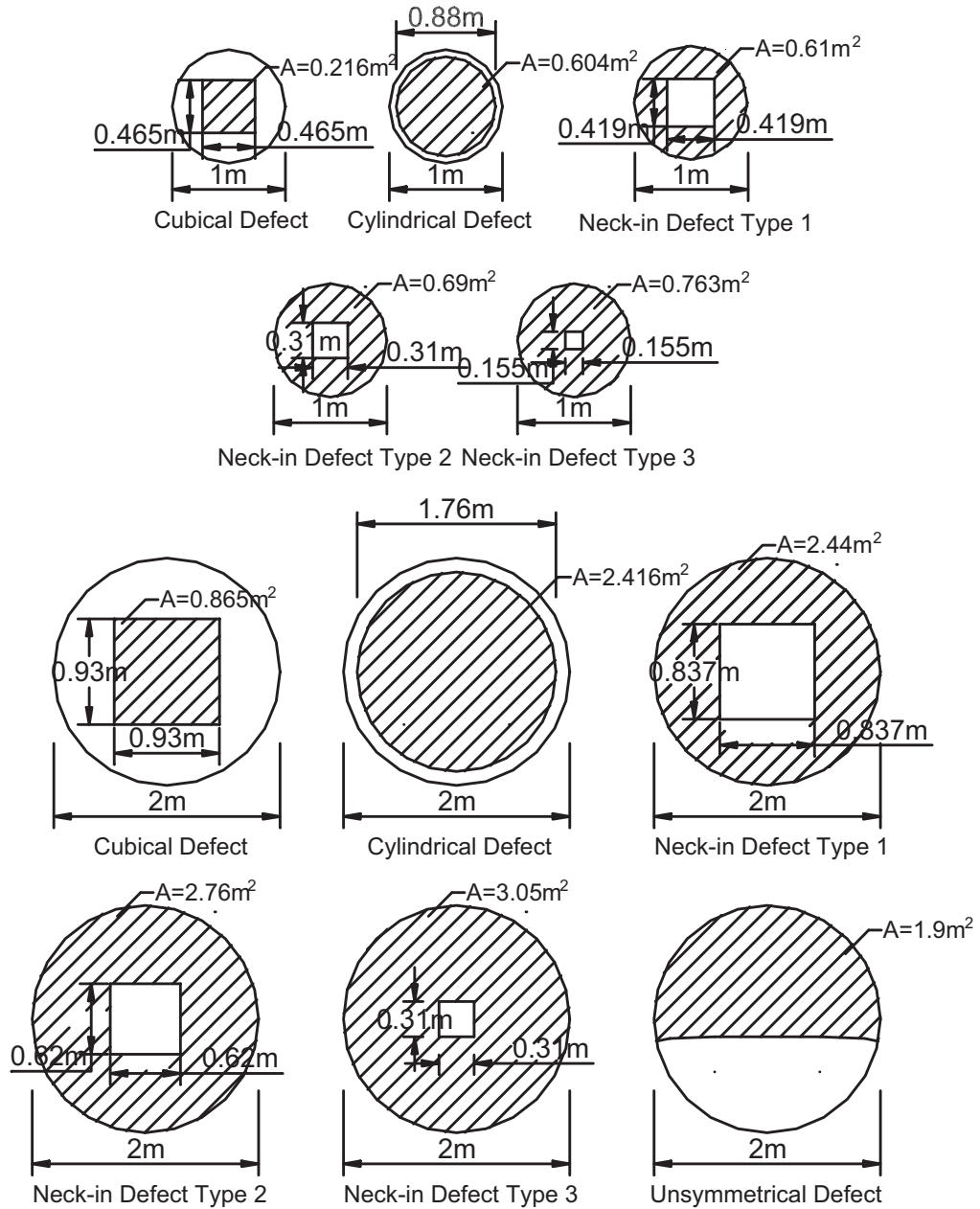


Figure 59. Anomaly sizes and shapes (shaded areas are anomaly zones).

5.2.2 Structural capacity of drilled shafts with anomalies

Structural capacities of drilled shafts with anomalies are represented in Table 16 for sections with concrete only and sections with concrete and 2% reinforcement. For anomaly sections with concrete only, structural capacities are computed using the values in Table 12. For cubical sections with 2% reinforcement, the structural capacities are computed using the values from Table 13. For drilled shafts with nonconcentric sections, the structural capacity for the axial load only or for the axial load and the bending moment can be calculated using the finite element analysis and interaction diagram, created using the method represented in Chapter 3. As shown in Figure 60, the point representing the structural capacity for axial load and bending moment (P and $M = 0.51P$, where $e = 0.51$ m is eccentricity) of drilled shafts with nonconcentric anomalies computed by finite element analysis lies nearly on the interaction curve.

Table 16. Structural capacities of drilled shafts with anomalies.

Concrete Strength kPa (psi)	Anomaly type	% Area Reduction (% Capacity Reduction)	Structural Capacity (kN)	
			(D = 2 m)	(D = 1m)
20,710 (3,000)	Cubical	27.5	46898	11613.0
	Cylindrical	77.3	14769	3692.0
	Neck-in type 1	77.3	14769	3692.0
	Neck-in type 2	87.7	8003	2001.0
	Neck-in type 3	96.7	2147	536.8
31,065 (4,500)	Cubical	27.5	71464	17866.0
	Cylindrical	77.3	22154	5538.0
	Neck-in type 1	77.3	22154	5538.0
	Neck-in type 2	87.7	12004	3001.0
	Neck-in type 3	96.7	3220	805.0

Table 16. (continued).

Concrete Strength kPa (psi)	Anomaly type	% Area Reduction	% Capacity Reduction	Structural Capacity (2% of reinforcement) (kN)	
				(D = 2 m)	(D = 1 m)
20,710 (3,000)	Cubical	27.5	19.1	64,867	16,117
	Nonconcentric (1)	77.3	87.7	9,857	-
	Nonconcentric (2)	77.3	58.8	33,070	-
31,065 (4,500)	Cubical	27.5	21.6	84,293	20,989
	Nonconcentric (1)	77.3	89.1	11,705	-
	Nonconcentric (2)	77.3	59.0	43,936	-

Note: (1) - Axial load and bending moment; (2) - Axial load only

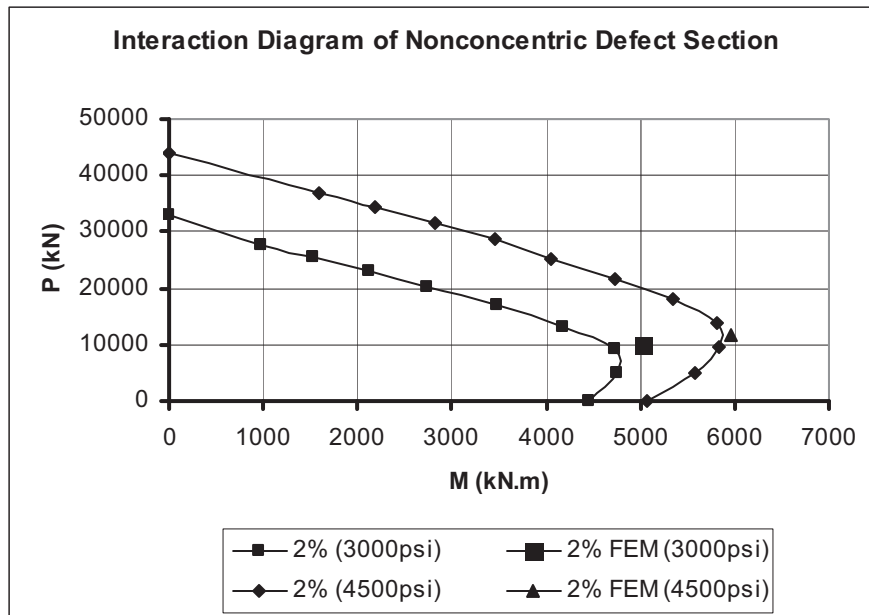


Figure 60. Structural capacity and interaction diagram of nonconcentric anomaly section.

5.3. SOIL PROPERTIES

The Mohr-Coulomb model was used to describe the behavior of the clay and sand with the former ranges from soft to stiff and the latter ranges from loose to dense. In the case of soft clay, a drilled shaft is assumed to rest on bedrock. The properties of soils are summarized in Table 17.

Table 17. Strength properties of soil.

Number	Soil type	Friction angle ($^{\circ}$)	Cohesion (kPa)
1	Sand	45	0
2	Sand	40	0
3	Sand	30	0
4	Clay	0	25
5	Clay	0	50
6	Clay	0	100
7	Clay	0	200
8	Clay	0	300

Soil Young's modulus varies with depth given in the following equation:

$$E = Kp_a \left(\frac{\sigma_3}{p_a} \right)^n \quad (\text{Eq. 58})$$

where E Young's modulus; K Young's modulus number; n Young's modulus exponent number; σ_3 horizontal stress varies with depth; and p_a atmospheric pressure.

For the sandy soil, Young's modulus is assumed to vary linearly with depth with $n = 1$. The dilatancy angles of soils as shown in Figure 61 can be determined by (Bolton, 1986):

$$\psi = \varphi_{tc} - \varphi_{cv} = 3 \left(D_r \left(10 - \ln \frac{100p}{p_a} \right) - 1 \right) \quad (\text{Eq. 59})$$

where φ_{tc} peak secant friction angle in triaxial compression test; φ_{cv} friction angle at critical void ratio; D_r relative density; p_a atmospheric pressure; and p mean pressure. Values of φ_{tc} are equal to φ , where $\varphi = 45^{\circ}$ at $D_r = 100\%$, $\varphi = 40^{\circ}$ at $D_r = 60\%$, and $\psi = 0^{\circ}$ for $\varphi = 30^{\circ}$.

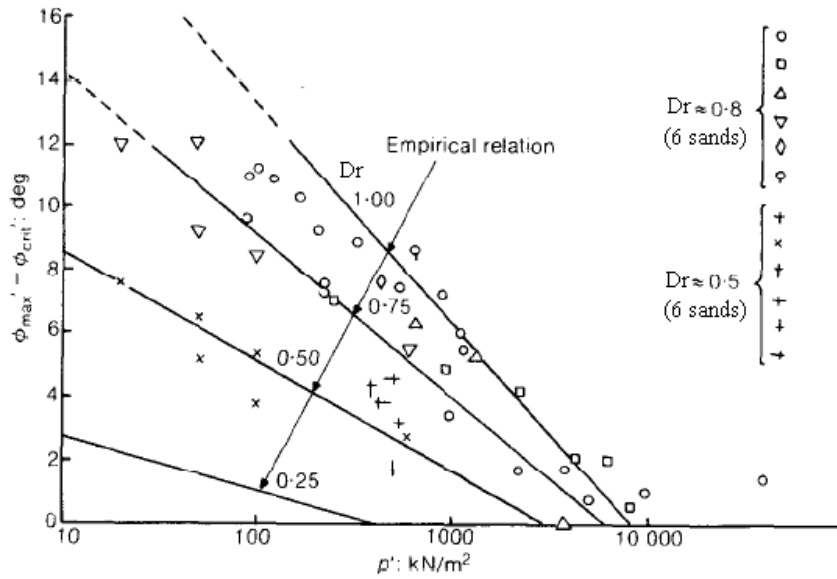


Figure 61. Dilatancy angles for sands (Bolton, 1986).

For the clay soil, Young's modulus is assumed to vary parabolically with depth and $n = 0.5$. Young's modulus does not affect the failure load of drilled shafts, for all cases, $K = 1000$. The Poisson's ratio for sand is 0.3 and for clay is 0.495. Bedrock at shaft tip in the clayey soil was modeled as an elastic material. The coefficient of lateral earth pressure at rest is assumed:

$$K_0 = 1 - \sin \varphi \quad (\text{Eq. 60})$$

5.4 SHAFT MODEL

The shaft is modeled by using 20-node solid elements, and reinforcement is modeled by nonlinear bar elements as represented in an earlier chapter. Under vertical load, only one-quarter of full model for symmetric anomaly and one-half of model for nonconcentric anomaly are used in analyses. The plane view and 3-D view of models are shown in Figure 62 for symmetric anomalies and Figure 63 for nonconcentric anomalies.

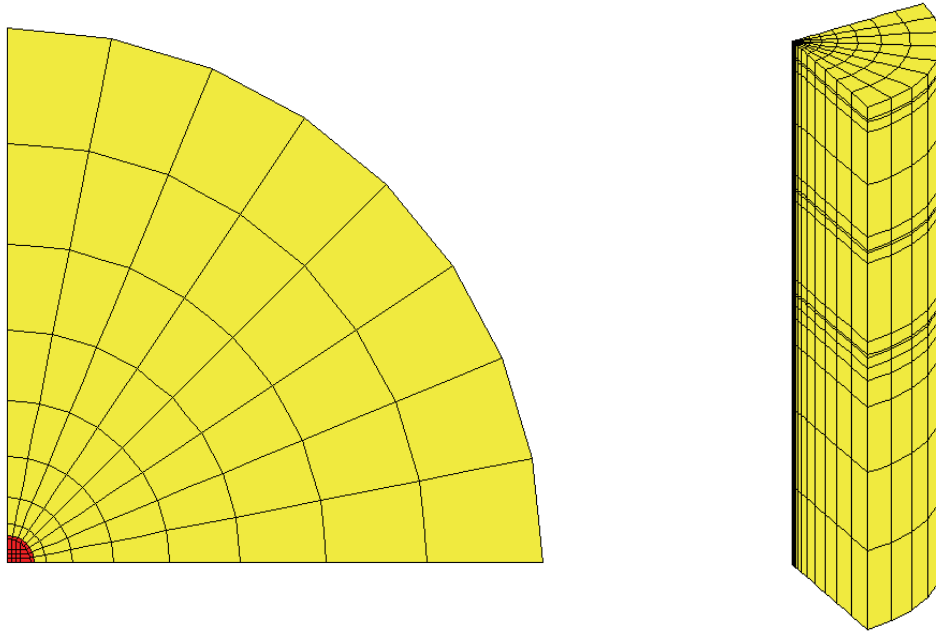


Figure 62. Plane and 3-D views of a drilled shaft with symmetric anomalies.

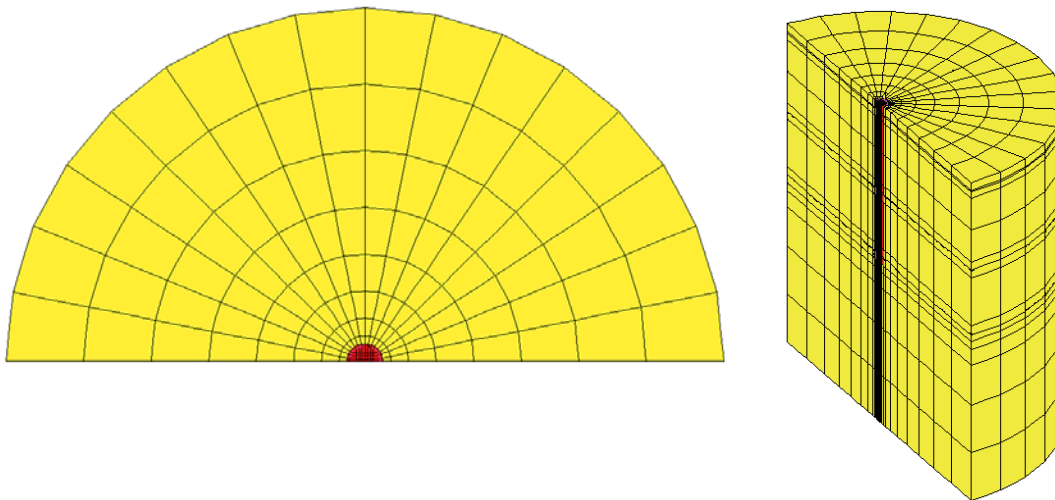


Figure 63. Plane and 3-D views of a drilled shaft with nonconcentric anomalies.

5.5 DEFINE THE EFFECT OF ANOMALIES

There are two kinds of capacities in drilled shaft design: geotechnical capacity and structural capacity. The former is the ultimate capacity of a drilled shaft for geotechnical consideration; the latter is the ultimate capacity of a drilled shaft for structural consideration. The smaller of the two controls the capacity of a drilled shaft and is further called drilled shaft capacity. When a load is applied to the top of a drilled shaft, it is transferred to both drilled shafts and its surrounding foundation soils in terms of side shear initially and eventually to both side shear and end bearing force. The total load transferred to the drilled shaft is termed “shaft-load transfer.” The total load transferred to the surrounding geomaterials is termed “geotechnical-load transfer” with an understanding that the sum of the load transferred to shaft and the load transferred to geomaterials equals the total load applied at the top of the drilled shaft.

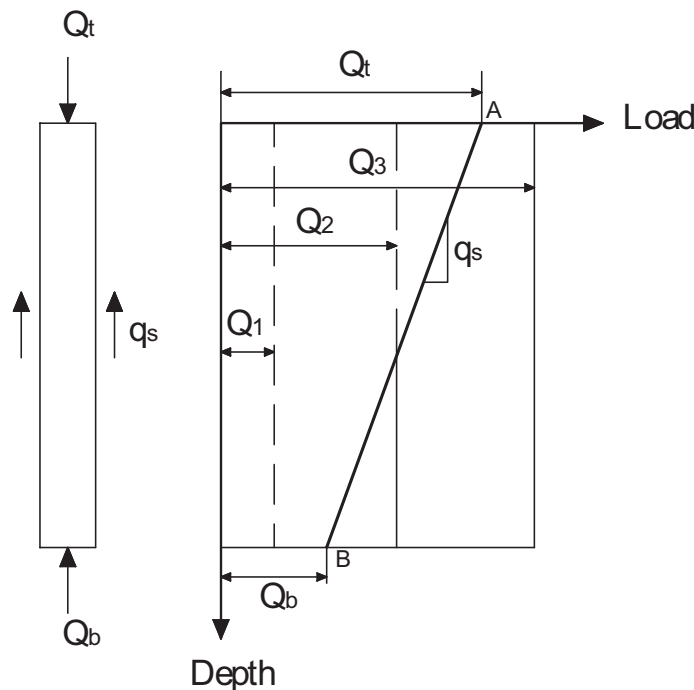


Figure 64. Effect definition of anomalies.

Anomalies affect the capacity of drilled shafts, only if the structural capacity of a shaft with anomaly is less than the axial load in the shaft at any depth where a anomaly is located. Figure 64 shows the distribution of the axial load along a drilled shaft. With the same anomaly at any depth, the structural capacity, Q_1 (or Q_3), is constant as represented by the vertical line in Figure 64. If the structural capacity line lies on the left side of the axial force line (no intersection), $Q_1 \leq Q_b$, the anomaly affects the drilled shaft capacity at any location; and the structural capacity controls. If the structural capacity line lies on the right side of the axial force line (no intersection), $Q_3 \geq Q_t$, the drilled shaft structure is much stronger than the geotechnical capacity; the anomaly has no affect on the shaft structural capacity at any location; and the geotechnical capacity controls. If the structural capacity line cuts the axial force line into two parts, $Q_b < Q_2 < Q_t$, anomalies located above the intersection point will have an effect on the drill shaft capacity; and the structural capacity controls. Anomalies located below the

intersection point have no effect, and the geotechnical capacity controls instead. The capacity indicated by the intersection of point A of the shaft-load transfer curve with the horizontal coordinate as shown in Figure 64 gives the geotechnical capacity of a drilled shaft.

5.6 CAPACITIES OF DRILLED SHAFTS IN COHESIVE SOILS

Geotechnical capacities of drilled shafts in cohesive soils are calculated using the α method and also obtained from the load-settlement curve for the soft, medium, and stiff clays. The method was also used to obtain the geotech capacities for very stiff clay and extremely stiff clay, where the load is the total load applied to a drilled shaft, by the finite element analyses. In finite element analyses, the drilled shaft capacities are selected as the load at a point with maximum curvature on a load-settlement curve as shown in Figures 65 and 66. The results of the two methods are compared in Table 18. In finite element analysis, at the failure load, the side resistances are the same as those in the α method; the tip resistances from the finite element analysis are, however, higher. The values of N_c^* predicted from the finite element method are about 9 to 11 for drilled shafts of both 1-m and 2-m in diameter, which is somewhat higher than the values used in the computation of side shear resistance in conventional drilled shaft design (Reese, et al., 2006). These values of N_c^* and $\alpha = 1$ are used to compute the shaft-load transfer curves at failure load by using Equations. 1 and 6 shown in Figures 67, 68, 69, and 70 for both 1-m and 2-m in diameter of drilled shafts.

Table 18. Geotechnical capacity of drilled shafts in cohesive soil.

Diameter (m)	Capacity (kPa)	FEM			α method		
		c_u (kPa)			c_u (kPa)		
		25	50	100	25	50	100
1	Q_s (Shaft)	1,570.8	3,141.6	6,283.2	1,570.8	3,141.6	6,283.2
	Q_b (Base)	185.2	370.4	886.8	176.7	353.4	706.8
	Q_t (Total)	1,756.0	3,512.0	7,170.0	1,747.5	3,495.0	6,990.0
2	Q_s (Shaft)	3,141.6	6,283.2	12,566.4	3,141.6	6,283.2	12,566.4
	Q_b (Base)	857.6	1,725.8	3,450.6	706.8	1,413.7	2827.4
	Q_t (Total)	4,004.0	8,009.0	16,017.0	3,848.4	7,696.9	15,393.8

Table 18. (continued).

Diameter (m)	Capacity (kPa)	FEM		α method	
		c_u (kPa)		c_u (kPa)	
		200	300	200	300
1	Q_s (Shaft)	12,562	18,842	12,562	18,842
	Q_b (Base)	1,608	2,720	1,414	2,120
	Q_t (Total)	14,170	21,562	13,976	20,962
2	Q_s (Shaft)	25,148	37,685	25,148	37,685
	Q_b (Base)	5,655	8,519	5,655	8,482
	Q_t (Total)	30,803	46,205	30,803	4,6167

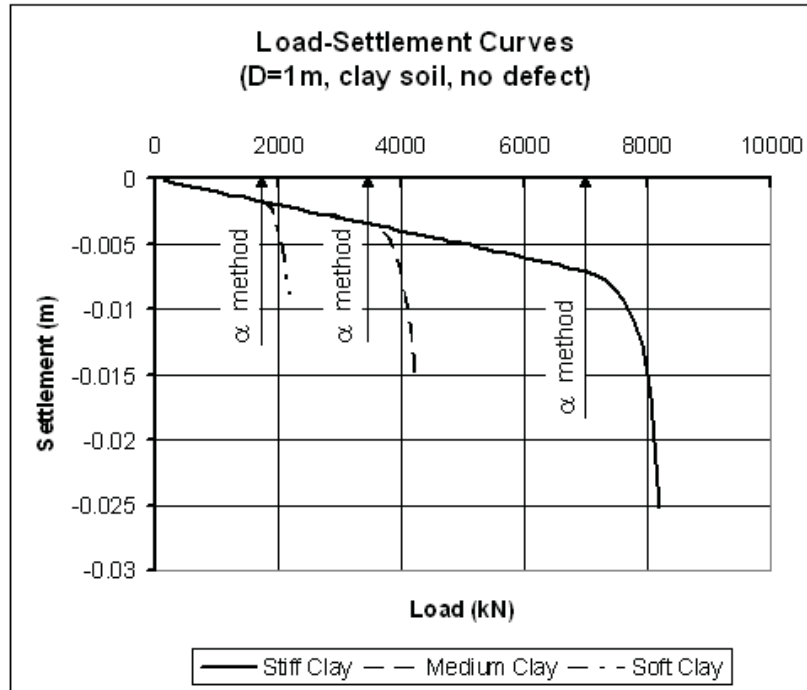


Figure 65. Load-settlement curves for 1-m diameter drilled shaft in clay with various stiffness.

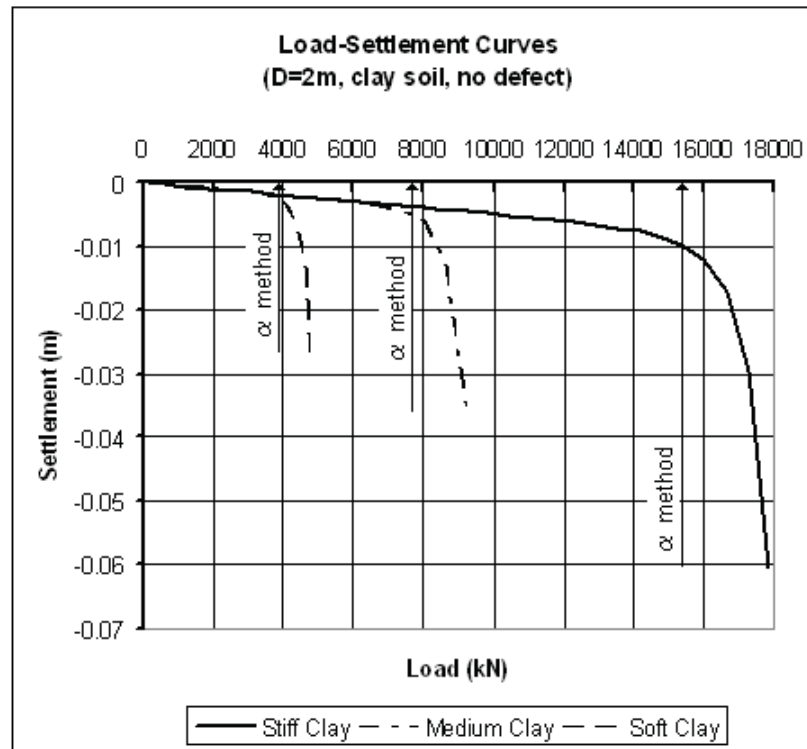


Figure 66. Load-settlement curves for 2-m diameter drilled shaft in clay with various stiffness.

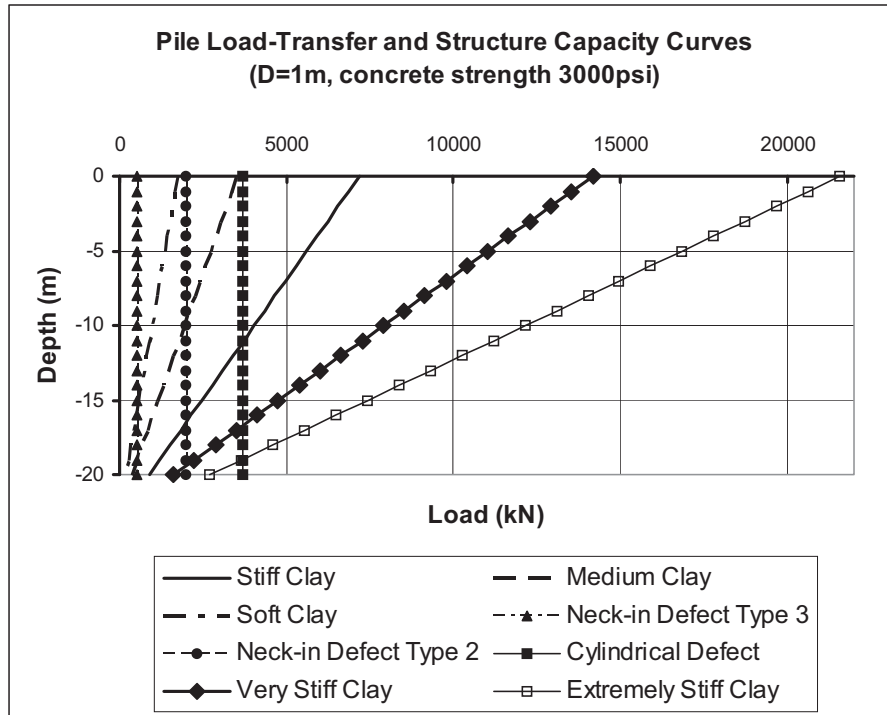


Figure 67. Shaft-load transfer and structural capacity curves for 1-m drilled shafts with 3,000 psi concrete constructed in clay.

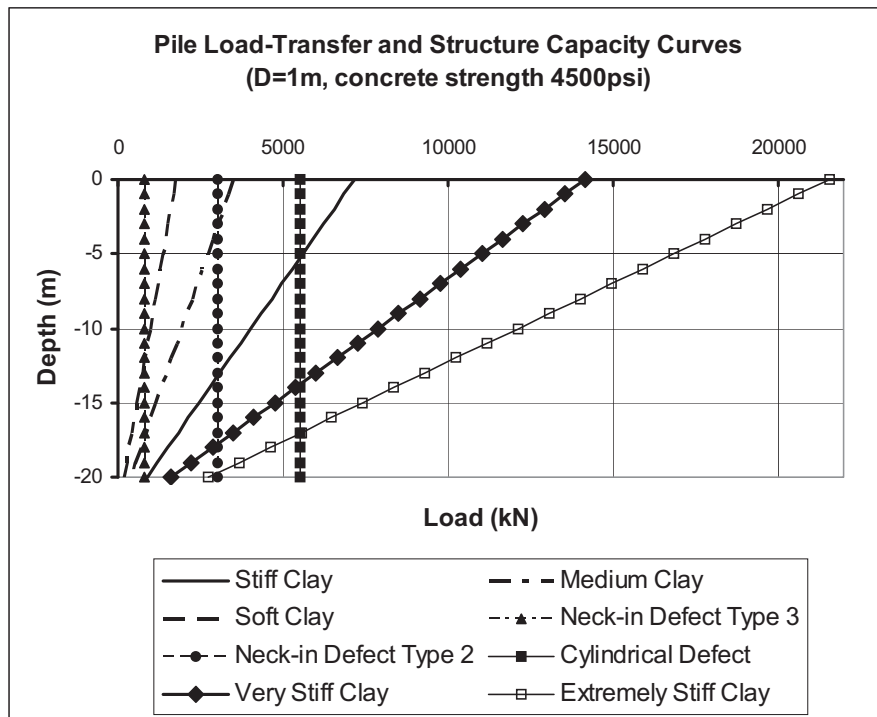


Figure 68. Shaft-load transfer and structural capacity curves for 1-m drilled shafts with 4,500 psi concrete constructed in clay.

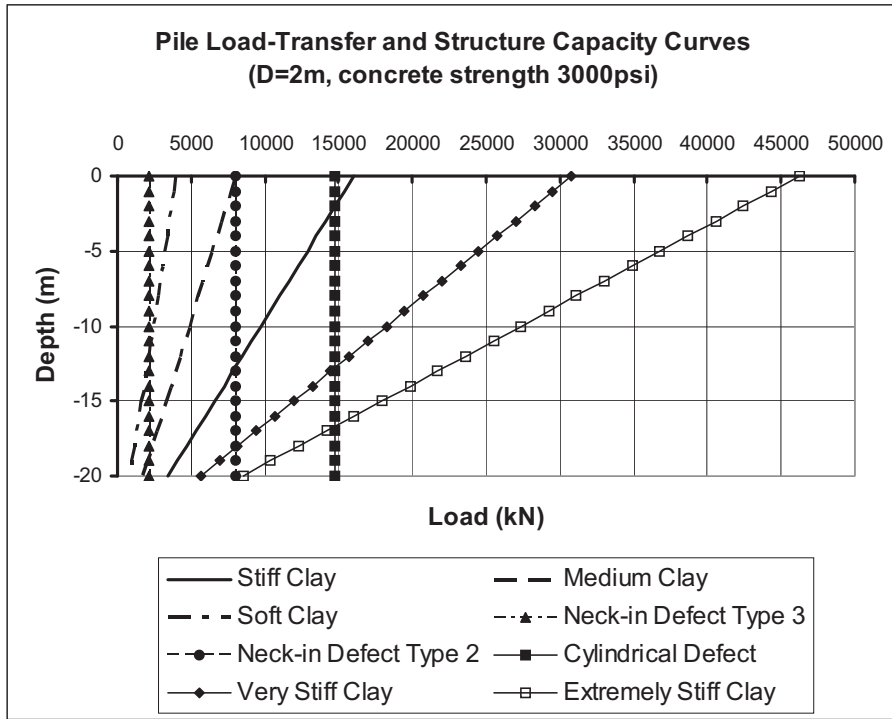


Figure 69. Shaft-load transfer and structural capacity curves for 2-m drilled shafts with 3,000 psi concrete constructed in clay.

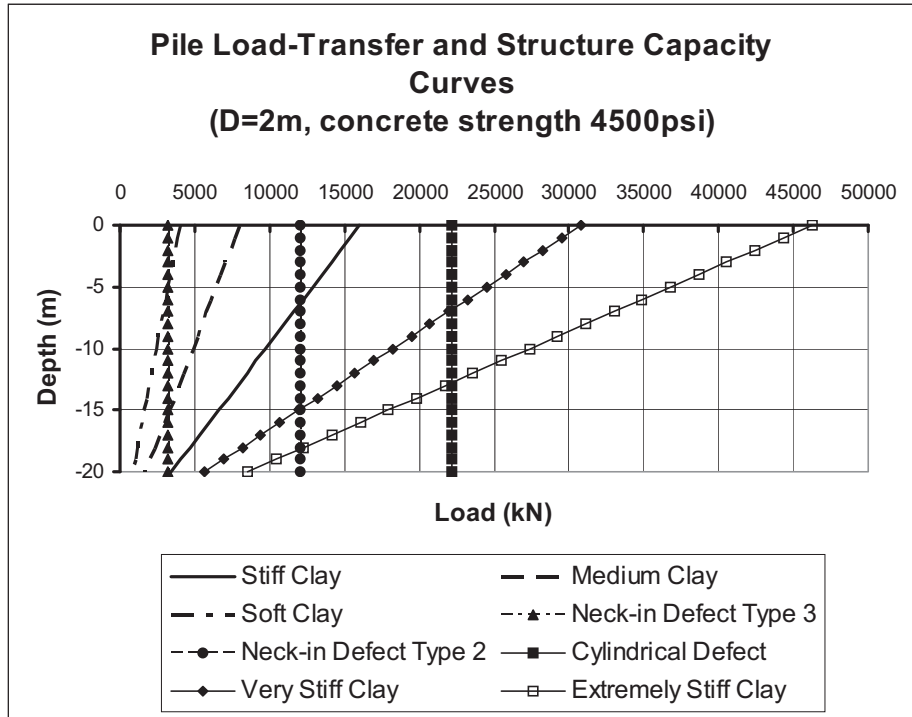


Figure 70. Shaft-load transfer and structural capacity curves for 2-m drilled shafts with 4,500 psi concrete constructed in clay.

As shown in Figures 69 and 70, each point on a structural capacity gives not only the structural capacity but also the anomaly location. When the point on a structural capacity line lies above a shaft-load transfer curve, then it indicates that the structural capacity is smaller than the corresponding shaft load; and the anomaly is said to affect negatively the capacity of drilled shafts. In this case, the structural capacity controls capacity of drilled shafts. Thus, the capacity of drilled shafts with anomalies located above the intersecting point is equal to the structural capacity with anomalies. This structural capacity is then compared to the geotechnical capacity, and the smaller one then is the drilled shaft capacity. The structural capacity reduction is defined as the ratio of the capacity with anomalies to the capacity without anomalies. The capacities of drilled shafts with anomalies are shown in Tables 19 and 20 for drilled shafts of 1-m diameter and Tables 21 and 22 for drilled shafts of 2-m diameter.

The structural capacity of a drilled shaft with a cubical anomaly as shown in Table 16 is much higher than its corresponding geotechnical capacities of drilled shafts (Table 18), and this anomaly has no effect on drilled shaft capacity. The effect on capacity of drilled shafts of all other anomaly types with a higher reduction of cross-sectional areas depends on size, location of anomaly, anomaly concentricity, and soil strength as can be seen in Figures 67, 68, 69, and 70.

The drilled shaft capacity reduction in clay with 1- to 1.2-m anomaly length is shown in Table 19 to Table 22. The structural anomaly in drilled shafts of 3000 psi concrete strength has more effect than the anomaly in drilled shafts of 4500 psi concrete strength because the structural capacity with 3000 psi concrete strength is smaller than that with 4500 psi concrete strength. For 2-m diameter drilled shafts with 4500 psi concrete strength, only the type 3 neck-in anomaly reduced the drilled shaft capacity.

The effect of anomalies depends on the slope of load transfer curve (or the strength of clay soil), especially for deep anomalies. For a given anomaly, the geotechnical load transfer to soil increases as the soil strength increases and, thus, the effect of anomaly decreases. At the same applied load, anomaly sections of drilled shafts in soft clay experiences more load than in stiff clay. The large anomalies significantly reduce axial stiffness of drilled shafts before failure. The load-settlement curves of drilled shafts with anomalies are below the load-settlement curves of drilled shafts without anomalies (see the Figures in the Appendix).

In comparison of neck-in anomaly Type 1 and cylindrical anomaly with the same reduction of cross-sectional area, the capacities of drilled shafts with neck-in Type 1 anomaly is much higher than those of drilled shafts with cylindrical anomaly as shown in Figures 71 and 72. In all analyses, all anomaly voids are assumed to be empty, which seems appropriate when a very weak soil fills the anomaly voids around the exterior surface of a drilled shaft.

A nonconcentric anomaly has a higher effect on the drilled shaft capacity than a concentric anomaly. This is due to the eccentricity caused by the bending moment in the shaft segment with anomaly under an axial load. In drilled shafts with nonconcentric anomaly near the shaft top, the structural capacities are generally less than those of the shafts with cylindrical anomalies of the same cross-sectional area reduction. For anomalies at greater depth, such as the anomaly at the middle of the shaft, the soil surrounding the drilled shaft can fail, so that the structural capacity

of a drilled shaft with a nonconcentric anomaly could be higher; therefore, the anomaly effect is of no significance. The capacity reductions are given in Tables 23 and 24.

The length of a anomaly, as defined earlier in Section 5.2, also has an affect on the capacity of a drilled shaft. For a long neck-in anomaly with no interface between soil and shaft, side resistance will be lost. The structural capacity of a anomaly segment is also affected by the length of the anomaly because of two end conditions. The longer anomaly has less capacity than the shorter anomaly as shown in Figure 73.

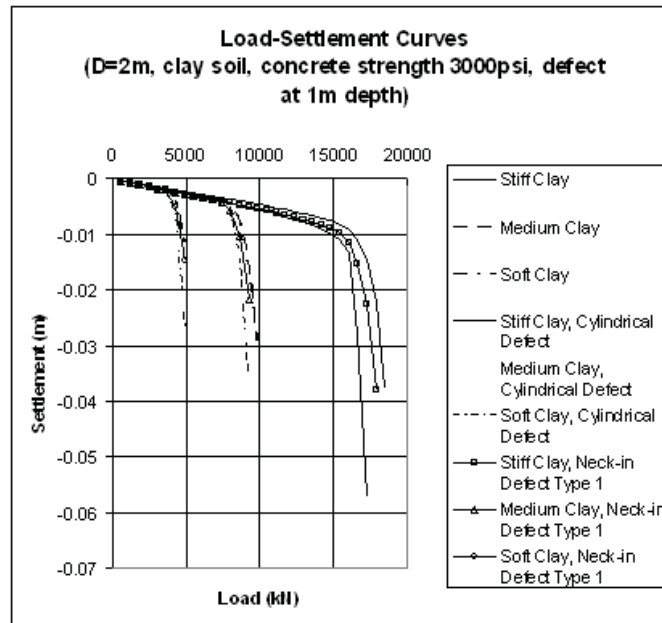


Figure 71. Neck-in anomaly Type 1 and cylindrical anomaly at 1-m depth, D = 2 m.

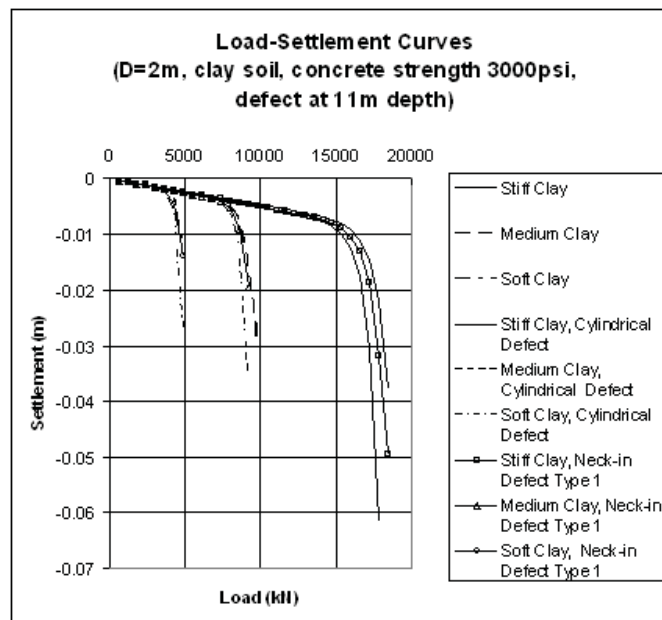


Figure 72. Neck-in anomaly Type 1 and cylindrical anomaly at 11-m depth, D = 2 m.

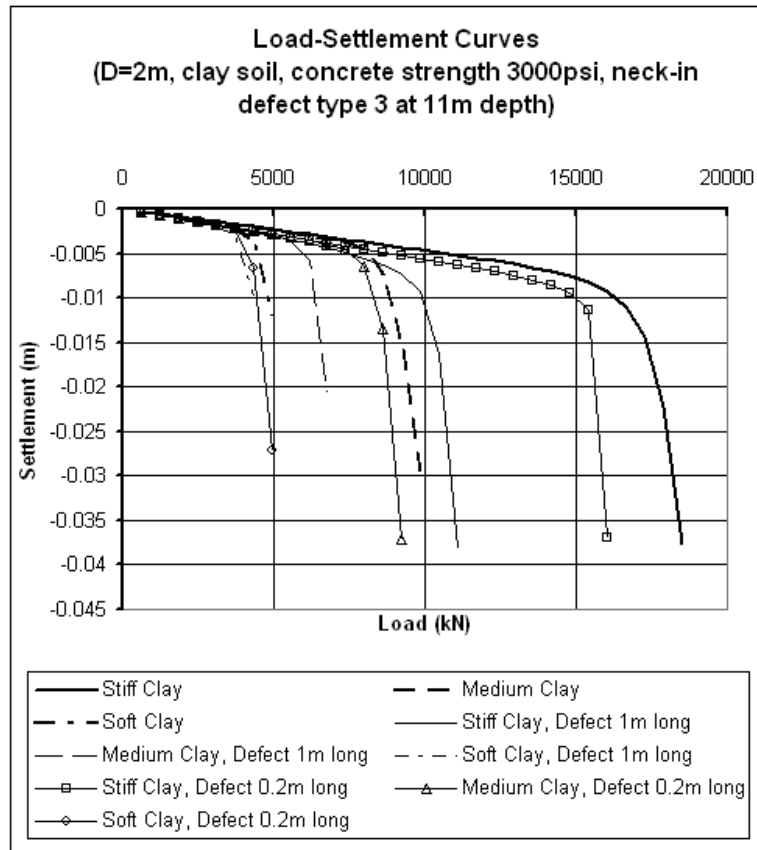


Figure 73. Comparison of short and long anomalies.

Table 19. Capacity reduction for the case of concrete strength 3,000 psi, shaft in clay, shaft diameter D = 1 m, anomaly length 1-1.2 m.

Cohesion, C_u (kPa)	Anomaly type	Anomaly location	Capacity (kN)	Capacity reduction (%)
25	Cylindrical	Top	1,756	0
		Middle	1,756	0
		Bottom	1,756	0
	Neck-in type 2	Top	1,756	0
		Middle	1,756	0
		Bottom	1,756	0
	Neck-in type 3	Top	770	56.2
		Middle	1,540	12.3
		Bottom	1,756	0
50	Cylindrical	Top	3,512	0
		Middle	3,512	0
		Bottom	3,512	0
	Neck-in type 2	Top	2,156	38.6
		Middle	3,512	0
		Bottom	3,512	0
	Neck-in type 3	Top	770	78.0
		Middle	2,464	30
		Bottom	3,512	0
100	Cylindrical	Top	4,158	42.0
		Middle	7,170	0
		Bottom	7,170	0
	Neck-in type 2	Top	2,310	67.8
		Middle	6,006	16.2
		Bottom	7,170	0
	Neck-in type 3	Top	924	87.0
		Middle	4,312	41.2
		Bottom	6,930	3.3

Table 20. Capacity reduction for the case of concrete strength 4,500 psi, shaft in clay, shaft diameter $D = 1$ m, anomaly length 1-1.2 m.

Cohesion, C_u (kPa)	Anomaly type	Anomaly location	Capacity (kN)	Capacity reduction (%)
25	Cylindrical	Top	1,756	0
		Middle	1,756	0
		Bottom	1,756	0
	Neck-in type 2	Top	1,756	0
		Middle	1,756	0
		Bottom	1,756	0
	Neck-in type 3	Top	770	56.0
		Middle	1,694	3.5
		Bottom	1,756	0
50	Cylindrical	Top	3,512	0
		Middle	3,512	0
		Bottom	3,512	0
	Neck-in type 2	Top	3,234	8.0
		Middle	3,512	0
		Bottom	3,512	0
	Neck-in type 3	Top	924	74.0
		Middle	2,772	21.0
		Bottom	3,512	0
100	Cylindrical	Top	5,852	18.0
		Middle	7,170	0
		Bottom	7,170	0
	Neck-in type 2	Top	3,388	53.0
		Middle	6,776	5.5
		Bottom	7,170	0
	Neck-in type 3	Top	1,078	85.0
		Middle	4,620	36.0
		Bottom	7,170	0

Table 21. Capacity reduction for the case of concrete strength 3,000 psi, shaft in clay, shaft diameter D = 2 m, anomaly length 1-1.2 m.

Cohesion, C_u (kPa)	Anomaly type	Anomaly location	Capacity (kN)	Capacity reduction (%)
25	Cylindrical	Top	4,004	0
		Middle	4,004	0
		Bottom	4,004	0
	Neck-in type 2	Top	4,004	0
		Middle	4,004	0
		Bottom	4,004	0
	Neck-in type 3	Top	1,848	54.0
		Middle	4,004	0
		Bottom	4,004	0
50	Cylindrical	Top	8,009	0
		Middle	8,009	0
		Bottom	8,009	0
	Neck-in type 2	Top	8,009	0
		Middle	8,009	0
		Bottom	8,009	0
	Neck-in type 3	Top	2,464	69.0
		Middle	6,160	23.0
		Bottom	8,009	0
100	Cylindrical	Top	16,017	0
		Middle	16,017	0
		Bottom	16,017	0
	Neck-in type 2	Top	10,473	34.6
		Middle	15,402	3.8
		Bottom	16,017	0
	Neck-in type 3	Top	2,464	84.6
		Middle	9,857	38.5
		Bottom	14,785	7.7

Table 22. Capacity reduction for the case of concrete strength 4,500 psi, shaft in clay, shaft diameter D = 2 m, anomaly length 1-1.2 m.

Cohesion, C_u (kPa)	Anomaly type	Anomaly location	Capacity (kN)	Capacity reduction (%)
25	Cylindrical	Top	4,004	0
		Middle	4,004	0
		Bottom	4,004	0
	Neck-in type 2	Top	4,004	0
		Middle	4,004	0
		Bottom	4,004	0
	Neck-in type 3	Top	3,080	30.00
		Middle	4,004	0
		Bottom	4,004	0
50	Cylindrical	Top	8,009	0
		Middle	8,009	0
		Bottom	8,009	0
	Neck-in type 2	Top	8,009	0
		Middle	8,009	0
		Bottom	8,009	0
	Neck-in type 3	Top	3,696	54.00
		Middle	6,776	15.04
		Bottom	8,009	0
100	Cylindrical	Top	16,017	0
		Middle	16,017	0
		Bottom	16,017	0
	Neck-in type 2	Top	15,401	3.08
		Middle	16,017	0
		Bottom	16,017	0
	Neck-in type 3	Top	3,696	76.09
		Middle	11,089	30.76
		Bottom	16,017	0

Table 23. Capacity reduction for nonconcentric anomaly, concrete strength 3,000 psi, shaft in clay, diameter D = 2 m, anomaly length 1-1.2 m.

Cohesion, C_u (kPa)	Anomaly location	Capacity (kN)	Capacity reduction (%)
25	Top	4,004	0
	Middle	4,004	0
	Bottom	4,004	0
50	Top	6,160	23.0
	Middle	8,009	0
	Bottom	8,009	0
100	Top	6,160	61.5
	Middle	16,017	0
	Bottom	16,017	0

Table 24. Capacity reduction for nonconcentric anomaly, concrete strength 4,500 psi, shaft in clay, diameter D = 2 m, anomaly length 1-1.2 m.

Cohesion, C_u (kPa)	Anomaly location	Capacity (kN)	Capacity reduction (%)
25	Top	4,004	0
	Middle	4,004	0
	Bottom	4,004	0
50	Top	6,160	23.0
	Middle	8,009	0
	Bottom	8,009	0
100	Top	6,160	61.5
	Middle	16,017	0
	Bottom	16,017	0

5.7 CAPACITIES OF DRILLED SHAFTS IN COHESIONLESS SOILS

In the case of drilled shafts in sandy soils, the soil capacities can be determined by following the procedures outlined in the FHWA manual (O’Neill and Reese, 1999) and by utilizing the finite element analyses. For drilled shafts in contractive loose sand, the capacity is computed at the point with maximum curvature on load-settlement as shown in (Figures 74 and 75). For the drilled shaft in medium and dense sands, the load-settlement curves in finite element analyses do not show a significant maximum curvature because of high dilation. Hence, the capacities computed by finite element analyses are based on the maximum stress at the shaft base as represented in Eq. 13 as outlined in the FHWA manual (O’Neill and Reese, 1999) ($N_{SPT} = 50$ for dense sand and $N_{SPT} = 30$ for medium sand). The analysis results are shown in Table 25. The shaft-load transfer curves and the structural capacity lines for drilled shafts with different anomalies are summarized in Figures 76 - 79. Tables 26 - 31 give the drilled shaft capacity reductions for the drilled shafts with different anomalies, where drilled shaft capacities are the smaller of structural and geotechnical capacities.

Table 25. Capacities of drilled shafts in sandy soils.

Diameter (m)	Capacity (kPa)	FEM			FHWA (1999) method		
		Friction Angle (ϕ)			Friction Angle (ϕ)		
		30 ⁰	40 ⁰	45 ⁰	30 ⁰	40 ⁰	45 ⁰
1	Q_s (Shaft)	3737	4905	8324	-	7923	7923
	Q_b (Base)	1037	1405	2107	-	1354	2258
	Q_t (Total)	4774	6310	10431	-	9278	10181
2	Q_s (Shaft)	7117	13587	17406	-	15847	15847
	Q_b (Base)	3356	5290	8798	-	5419	9032
	Q_t (Total)	10473	18877	26204	-	21266	24879

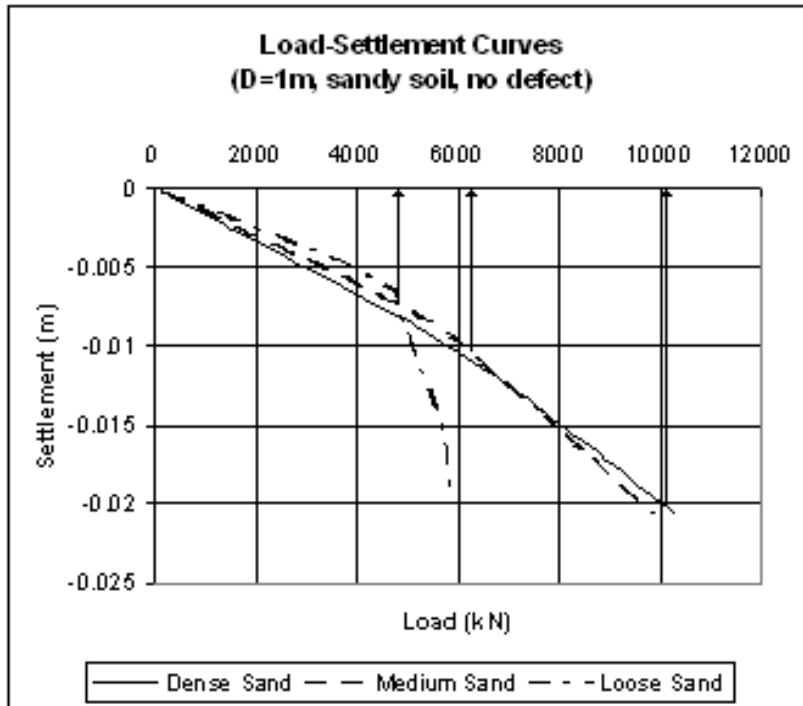


Figure 74. Load-settlement curves for drilled shafts of 1-m diameter in sand.

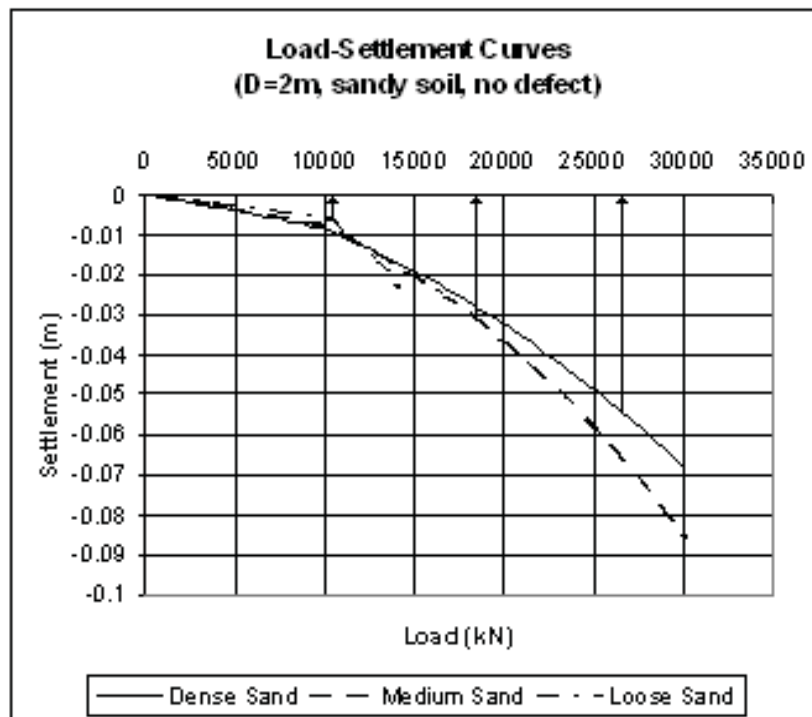


Figure 75. Load-settlement curves for drilled shafts of 2-m diameter in sand.

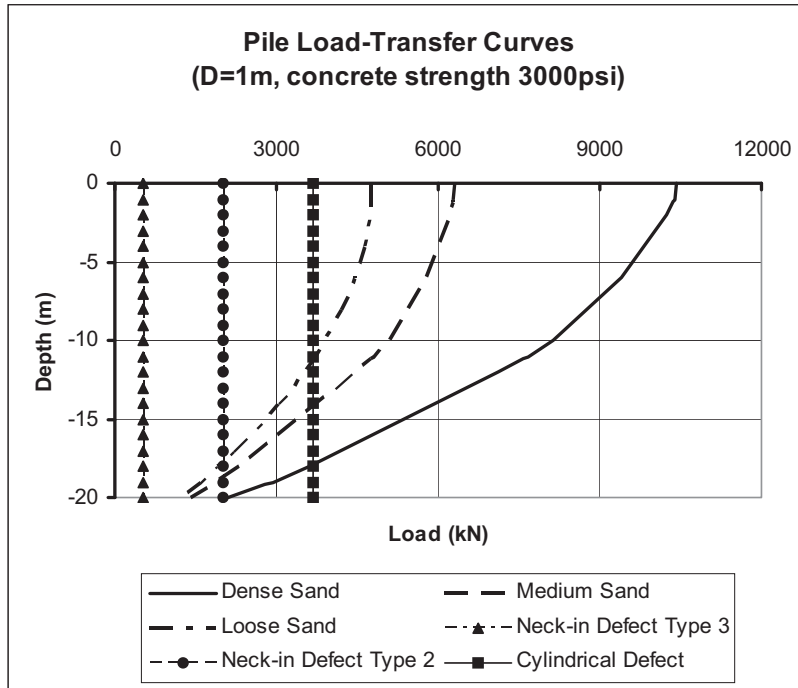


Figure 76. Shaft-load transfer curves for drilled shafts of 1-m diameter in sand.

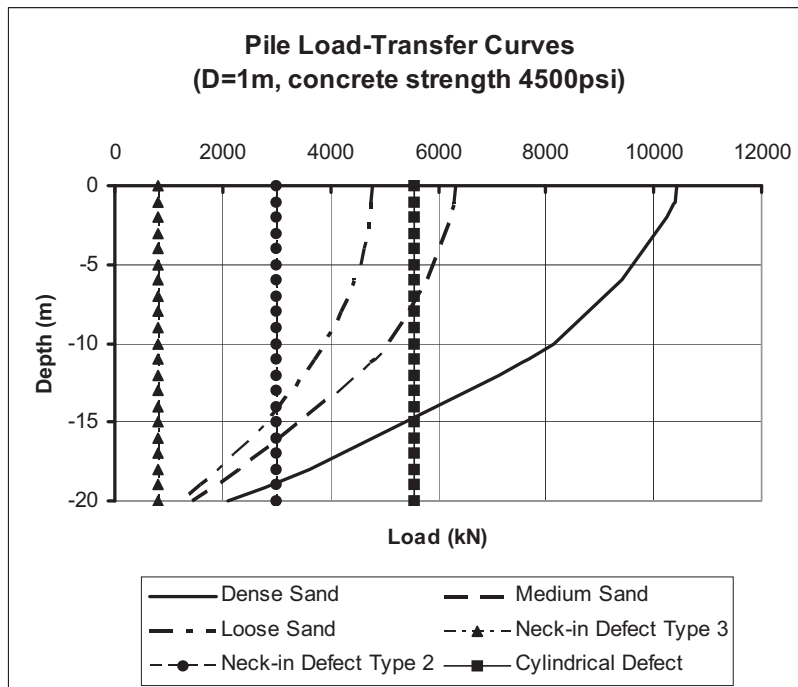


Figure 77. Shaft-load transfer curves for drilled shafts of 1-m diameter in sand.

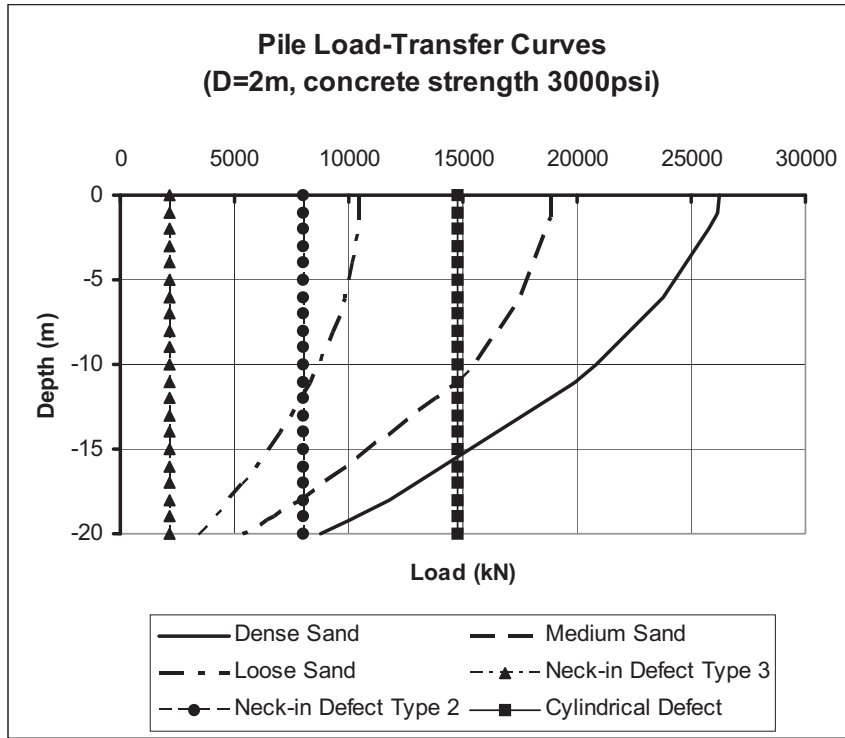


Figure 78. Shaft-load transfer curves for drilled shafts of 2-m diameter in sand.

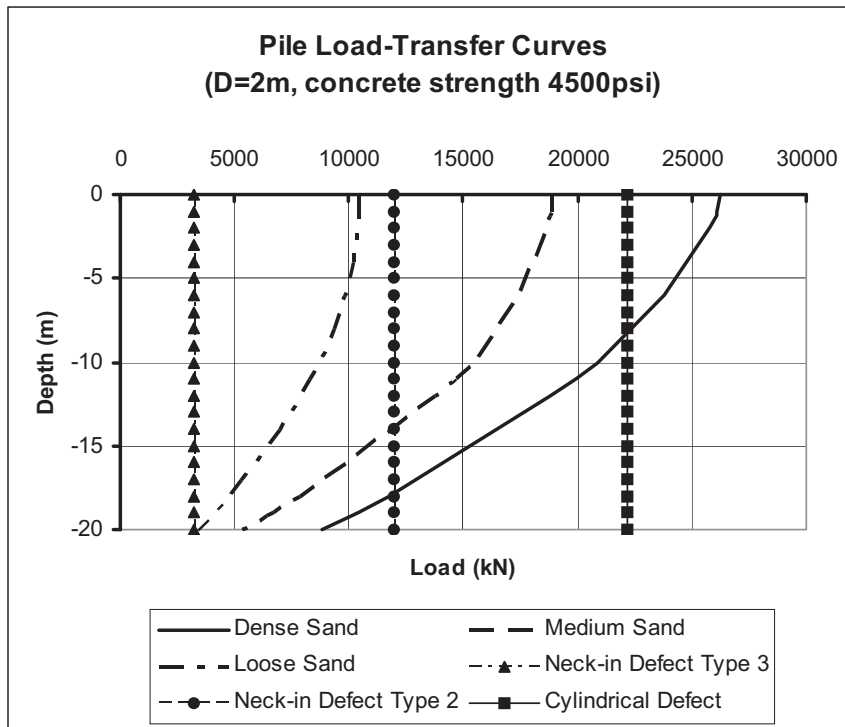


Figure 79. Shaft-load transfer curves for drilled shafts of 2-m diameter in sand.

Table 26. Drilled shaft capacity reduction for the case of concrete strength 3,000 psi, shaft in sand, shaft diameter D = 1 m, anomaly length 1-1.2 m.

Friction angle, ϕ	Anomaly type	Anomaly location	Capacity (kN)	Capacity reduction (%)
30	Cylindrical	Top	3,850	19.4
		Middle	4,774	0
		Bottom	4,774	0
	Neck-in type 2	Top	2,002	58.0
		Middle	3,234	32.2
		Bottom	4,774	0
	Neck-in type 3	Top	462	90.3
		Middle	1,694	64.5
		Bottom	4,158	12.9
40	Cylindrical	Top	3,850	39.0
		Middle	5,544	12.1
		Bottom	6,310	0
	Neck-in type 2	Top	2,002	68.3
		Middle	3,542	43.9
		Bottom	6,310	0
	Neck-in type 3	Top	462	92.7
		Middle	1,848	70.7
		Bottom	4,620	27.0
45	Cylindrical	Top	3,850	63.0
		Middle	5,698	45.4
		Bottom	10,431	0
	Neck-in type 2	Top	2,002	80.8
		Middle	3,696	64.6
		Bottom	10,431	0
	Neck-in type 3	Top	462	95.6
		Middle	2,156	79.3
		Bottom	4,158	60.0

Table 27. Drilled shaft capacity reduction for the case of concrete strength 4,500 psi, shaft in sand, shaft diameter D = 1 m, anomaly length 1-1.2 m.

Friction angle, ϕ	Anomaly type	Anomaly location	Capacity (kN)	Capacity reduction (%)
30	Cylindrical	Top	4,774	0
		Middle	4,774	0
		Bottom	4,774	0
	Neck-in type 2	Top	2,926	38.70
		Middle	4,312	9.70
		Bottom	4,774	0
	Neck-in type 3	Top	770	83.90
		Middle	1,848	61.30
		Bottom	4,158	12.90
40	Cylindrical	Top	4,928	21.90
		Middle	6,310	0
		Bottom	6,310	0
	Neck-in type 2	Top	3,080	51.20
		Middle	4,774	24.34
		Bottom	6,310	0
	Neck-in type 3	Top	770	87.80
		Middle	2,310	63.40
		Bottom	4,620	27.00
45	Cylindrical	Top	4,928	58.80
		Middle	8,808	15.60
		Bottom	10,431	0
	Neck-in type 2	Top	3,080	70.40
		Middle	4,928	52.70
		Bottom	10,431	0
	Neck-in type 3	Top	770	92.60
		Middle	2,464	76.40
		Bottom	4,620	55.70

Table 28. Drilled shaft capacity reduction for the case of concrete strength 3,000 psi, shaft in sand, shaft diameter D = 2 m, anomaly length 1-1.2 m.

Friction angle, ϕ	Anomaly type	Anomaly location	Capacity (kN)	Capacity reduction (%)
30	Cylindrical	Top	10,473	0
		Middle	10,473	0
		Bottom	10,473	0
	Neck-in type 2	Top	9,857	5.9
		Middle	10,473	0
		Bottom	10,473	0
	Neck-in type 3	Top	1,848	82.3
		Middle	4,312	58.8
		Bottom	9,857	5.9
40	Cylindrical	Top	15,401	18.4
		Middle	18,877	0
		Bottom	18,877	0
	Neck-in type 2	Top	9,857	47.8
		Middle	12,937	31.5
		Bottom	18,877	0
	Neck-in type 3	Top	1,848	90.2
		Middle	5,544	70.6
		Bottom	10,473	44.5
45	Cylindrical	Top	15,401	41.2
		Middle	20,946	20.0
		Bottom	26,204	0
	Neck-in type 2	Top	9,857	62.4
		Middle	13,553	48.3
		Bottom	26,204	0
	Neck-in type 3	Top	1,848	92.9
		Middle	5,544	78.8
		Bottom	10,473	60.0

Table 29. Drilled shaft capacity reduction for the case of concrete strength 4,500 psi, shaft in sand, shaft diameter D = 2 m, anomaly length 1-1.2 m.

Friction angle, ϕ	Anomaly type	Anomaly location	Capacity (kN)	Capacity reduction (%)
30	Cylindrical	Top	10,473	0
		Middle	10,473	0
		Bottom	10,473	0
	Neck-in type 2	Top	10,473	0
		Middle	10,473	0
		Bottom	10,473	0
	Neck-in type 3	Top	3,080	70.6
		Middle	5,544	47.0
		Bottom	9,857	5.9
40	Cylindrical	Top	18,877	0
		Middle	18,877	0
		Bottom	18,877	0
	Neck-in type 2	Top	14,785	21.7
		Middle	17,250	8.6
		Bottom	18,877	0
	Neck-in type 3	Top	3,080	83.7
		Middle	6,160	67.4
		Bottom	11,705	38.0
45	Cylindrical	Top	20,946	20.0
		Middle	26,204	0
		Bottom	26,204	0
	Neck-in type 2	Top	14,785	43.6
		Middle	17,250	34.2
		Bottom	26,204	0
	Neck-in type 3	Top	3,080	88.2
		Middle	6,160	76.5
		Bottom	12,937	50.6

Table 30. Drilled shaft capacity reduction for nonconcentric anomaly, concrete strength 3,000 psi, soil in sand, diameter D = 2 m, anomaly length 1-1.2 m.

Friction angle, ϕ	Anomaly location	Capacity (kN)	Capacity reduction (%)
30	Top	6,160	41.0
	Middle	10,473	0
	Bottom	10,473	0
40	Top	6,160	67.4
	Middle	18,877	0
	Bottom	18,877	0
45	Top	6,160	76.5
	Middle	26,204	0
	Bottom	26,204	0

Table 31. Drilled shaft capacity reduction for nonconcentric anomaly, concrete strength 4,500 psi, diameter D = 2m, soil in sand, anomaly length 1-1.2m.

Friction angle, ϕ	Anomaly location	Capacity (kN)	Capacity reduction (%)
30	Top	6,160	41.0
	Middle	10,473	0
	Bottom	10,473	0
40	Top	6,160	67.4
	Middle	18,877	0
	Bottom	18,877	0
45	Top	6,160	76.5
	Middle	26,204	0
	Bottom	26,204	0

5.8 Capacities of drilled shafts in cohesive soil with bedrock at shaft tip

For the drilled shafts with cubical anomalies, the drilled shaft is in clay soil with the shaft tip on rock, and the drilled shaft capacity is equal to the structural capacity. The reductions of capacities are given in Table 32 to Table 35. As observed in other cases, the anomalies of the drilled shafts in soft clay impose more significant effect on drilled shaft capacity than the anomalies in drilled shafts in stiff clay.

Table 32. Drilled shaft capacity reduction for the case of concrete strength 3,000 psi, shaft in clay with bedrock at shaft tip, shaft diameter $D = 1$ m, anomaly length 1-1.2 m.

Cohesion, C_u (kPa)	Anomaly location	Capacity (kN)	Capacity reduction (%)
25	Top	16,200	18.72
	Middle	16,900	15.21
	Bottom	17,500	12.20
50	Top	16,300	18.22
	Middle	17,700	11.19
	Bottom	18,900	5.17
100	Top	16,500	17.21
	Middle	19,300	3.17
	Bottom	19,931	0.00
200	Top	16,800	15.71
	Middle	19,931	0.00
	Bottom	19,931	0.00
300	Top	17,100	14.20
	Middle	19,931	0.00
	Bottom	19,931	0.00

Table 33. Drilled shaft capacity reduction for the case of concrete strength 4,500 psi, shaft in clay with bedrock at shaft tip, shaft diameter D = 1 m, anomaly length 1-1.2 m.

Cohesion, C_u (kPa)	Anomaly location	Capacity (kN)	Capacity reduction (%)
25	Top	21,000	21.37
	Middle	21,700	18.75
	Bottom	22,400	16.13
50	Top	21,100	21.00
	Middle	22,500	15.76
	Bottom	23,800	10.89
100	Top	21,300	20.25
	Middle	24,100	9.76
	Bottom	26,708	0.00
200	Top	21,700	18.75
	Middle	26,708	0.00
	Bottom	26,708	0.00
300	Top	22,100	17.25
	Middle	26,708	0.00
	Bottom	26,708	0.00

Table 34. Drilled shaft capacity reduction for the case of concrete strength 3,000 psi, shaft in clay with bedrock at shaft tip, shaft diameter D = 2 m, anomaly length 1-1.2 m.

Cohesion, C_u (kPa)	Anomaly location	Capacity (kN)	Capacity reduction (%)
25	Top	65,000	18.97
	Middle	66,600	16.97
	Bottom	67,700	15.60
50	Top	65,200	18.72
	Middle	68,300	14.85
	Bottom	70,600	11.99
100	Top	65,600	18.22
	Middle	71,900	10.36
	Bottom	76,300	4.88
200	Top	66,300	17.35
	Middle	78,900	1.64
	Bottom	80,214	0.00
300	Top	66,900	16.60
	Middle	80,214	0.00
	Bottom	80,214	0.00

Table 35. Capacity reduction for the case of concrete strength 4,500 psi, shaft in clay with bedrock at shaft tip, shaft diameter D = 2 m, anomaly length 1-1.2 m.

Cohesion, C_u (kPa)	Anomaly location	Capacity (kN)	Capacity reduction (%)
25	Top	84,400	21.35
	Middle	86,000	19.86
	Bottom	87,100	18.84
50	Top	84,600	21.17
	Middle	87,800	18.18
	Bottom	90,000	16.13
100	Top	85,000	20.79
	Middle	91,300	14.92
	Bottom	95,700	10.82
200	Top	85,800	20.05
	Middle	98,300	8.40
	Bottom	107,313	0.00
300	Top	86,400	19.49
	Middle	105,400	1.78
	Bottom	107,313	0.00

CHAPTER 6 - SUMMARY, CONCLUSIONS, AND RECOMMENDATIONS

6.1 SUMMARY

The objective of this report is to study the effect of structural anomalies in a drilled shaft on its capacity, to produce guidelines for assessing the importance of anomalies on the drilled shaft capacity in different soils, and to prioritize anomalies the remediation effort.

The study included: 1) conducting a comprehensive literature search of drilled shafts with anomalies; 2) developing the finite element code, PSI-VA, for use in this study; and 3) evaluating the effect of factors such as anomaly location and sizes, soil types, and concrete strength on shaft capacity.

The anomalies (or anomaly or imperfection) were caused mainly by the deficiencies in construction quality control that resulted in the creation of a void or voids with or without earth filling, as reported by DiMaggio (2008), Haramy (2006), and Mullins, etc., (2005). These anomalies can be located by various geophysical and tomographic techniques (Haramy, 2006; Haramy, et al., 2007). Once located, the subsequent tasks would include the assessment of its effect on the drilled shaft capacity, which is dictated by its structural and geotechnical capacities and also the design of a corrective measure. This study focuses on the anomaly effect on the drilled shaft capacity. A comprehensive finite element analysis program was carried to assess the effect of concentric anomalies. The study covers 1-m and 2-m diameter drilled shafts in clayey soils including soft, medium, stiff, very stiff, and extremely stiff clays and the medium, dense, and very dense sands. The study can be expanded to cover the effect of nonconcentric anomalies under both axial and lateral loads, static and/or dynamic, expected to more dramatically affect the drilled shaft capacity.

6.2 FINDINGS AND CONCLUSIONS

The comprehensive finite element analysis program provides the following major conclusions: anomalies will affect axial structural capacity; drilled shaft capacity is affected by the size and location of anomalies and the strength of the surrounding soils; and concentric anomalies can drastically decrease the structural capacity of a drilled shaft even under axial load, depending on the location of anomalies.

Finite element analyses were also performed to validate the PSI computer code for predicting the measured performance of drilled shafts and also to compare the PSI predictions to the analysis results using other computer codes. Findings confirmed that excellent agreements were achieved between the PSI results and the measured shaft-load test results under vertical or lateral load CDOT (Jamal Nusairat, et al., 2004), Brinkgreve (2004), and UC Berkeley (Wang, et al., 2004). Excellent agreements were also achieved between the PSI results and the analysis results using PLAXIS 2D, PLAXIS 3D, ABAQUS, ANASYS, and LS-DYNA by the authors cited in the article. These comparisons validate **PSI code** as an effective code for use in assessing drilled shaft performance under vertical and/or lateral loads. Based on the PSI code, PSI-VA was developed specifically for the evaluation of the anomaly effect on drilled shaft capacity.

PSI-VA was then used in the finite element analysis for the evaluation of the effect of anomalies on drilled shaft capacities. Analysis and findings of 1-m and 2-m in diameter drilled shafts in clayey soils including soft, medium, stiff, very stiff, and extremely stiff clays and medium, dense, and very dense sands are summarized as follows:

- Structural capacity reduction of drilled shafts depends on concentricity of anomalies. Nonconcentric anomalies result in much more severe structural capacity reduction.
- When the structural capacity is smaller than the geotechnical capacity over some length of a drilled shaft, the structural capacity curve intersects the shaft-load transfer curve. In this case the anomalies located at a depth shallower than the depth of such intersection will result in drilled shaft capacity reduction, which is controlled by the reduced structural capacity. Below such depth, however, the anomaly will not affect the drilled shaft capacity.
- When structural capacity is larger than geotechnical capacity, the shaft-load transfer curve lies to the left of structural capacity curve; and the drilled shaft experiences smaller loads than that associated with the structural capacity. Thus, structural anomalies do not affect the drilled capacity; and the geotechnical capacity controls its design.
- When the structural capacity curve lies to the left of geotechnical capacity curve, the drilled shaft capacity is affected by the anomalies located at any depth; and the structural capacity controls the design.
- Analysis results show that nonconcentric anomalies drastically compromise the structural capacity because of the bending moment, and nonconcentric anomalies are much more critical.
- The strength of soils surrounding drilled shafts influences the drilled shaft capacity and performance. Thus, the effects of soil types and strengths on load transfer must be investigated.
- It is critical to locate a anomaly(s) and assess its effects on the drilled shaft capacity.
- Because of the potentially strong negative effect of anomalies on drilled shaft capacity, it is of paramount importance to monitor the drilled shaft construction QA/QC, including maintaining a proper rebar spacing-aggregate size ratio and a proper concrete slump (or fluidity) to avoid anomalies in regions outside the reinforcing cage. Once detected, it must be eradicated by grouting.

6.3 RECOMMENDATIONS FOR REMEDIATION

The following are the recommendations for the remediation guidelines:

- A proper construction quality monitoring program including sonic wave survey; tomographic imaging; and temperature, moisture, and density measurements are recommended for all critical drilled shafts.
- Once anomalies are located, the voids must be filled with concrete grout.
- If prioritization is necessary in fixing the anomalies, the shallow, nonconcentric anomalies must receive first attention because of higher load and more drastic effect of anomalies.

- The effects of soil types and strengths must be properly assessed from the shaft-load transfer curve and the structural-capacity curve to assess the critical nature of a anomaly(s).

6.4 FUTURE STUDY

The following extensions would have completed the comprehensive study on the effect of anomalies on drilled shaft capacity:

- Install strain gages (or load cells) at a proper depth increment to measure load transferred; and, if possible, install settlements at different depths to provide t-z curves for assessing the load transfer. These gages and load cells could have been used to monitor the drilled shaft performance and safety during its lifetime.
- Extend the study to cover the effect of nonconcentric anomalies on vertical drilled shaft capacity.
- Extend the study to cover the effect of anomaly on the lateral load carrying capacity of a drilled shaft.
- Extend the study to cover the transient loads, like wind and seismic loads.
- Complete the development of a computer code for the design of drilled shafts under static and transient loads. This code could be named PSI-VLT for vertical, lateral, and torsional loads. It could be developed into a comprehensive program to be used in drilled shaft design.

APPENDIX A – FIGURES

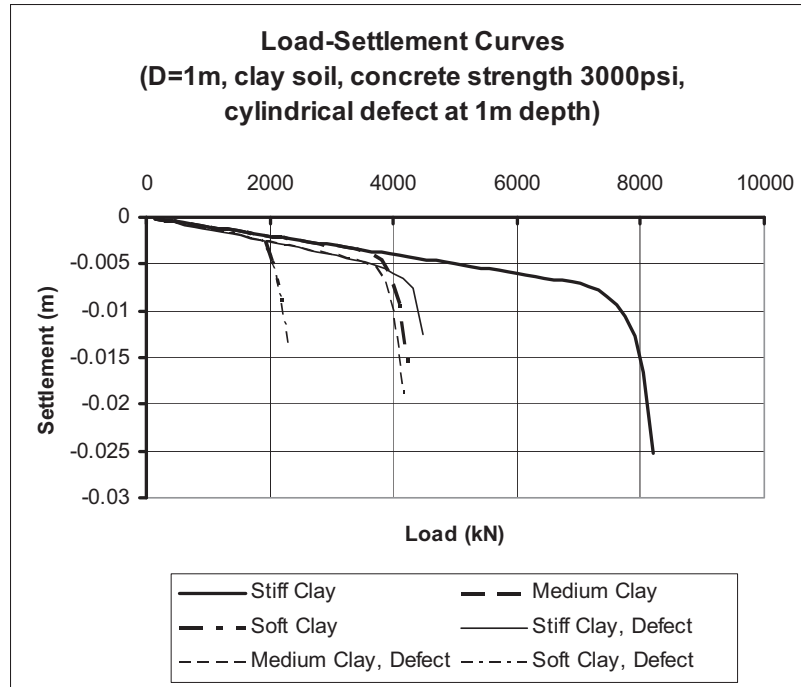


Figure 80. Load-settlement curves for drilled shafts of 1-m diameter in clay (Concrete strength 3,000 psi, 1-m length cylindrical anomaly at 1-m depth).

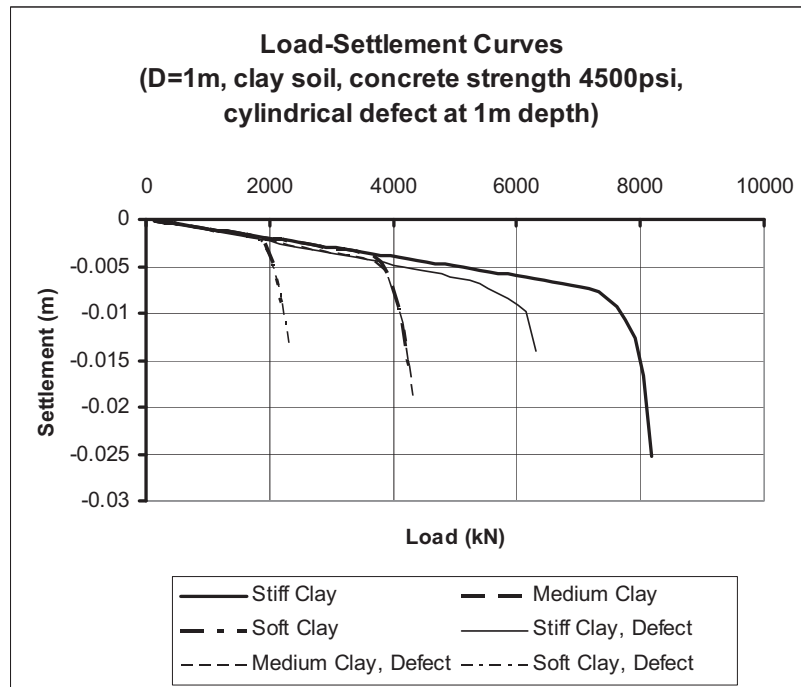


Figure 81. Load-settlement curves for drilled shafts of 1-m diameter in clay (Concrete strength 4,500 psi, 1-m length cylindrical anomaly at 1-m depth).

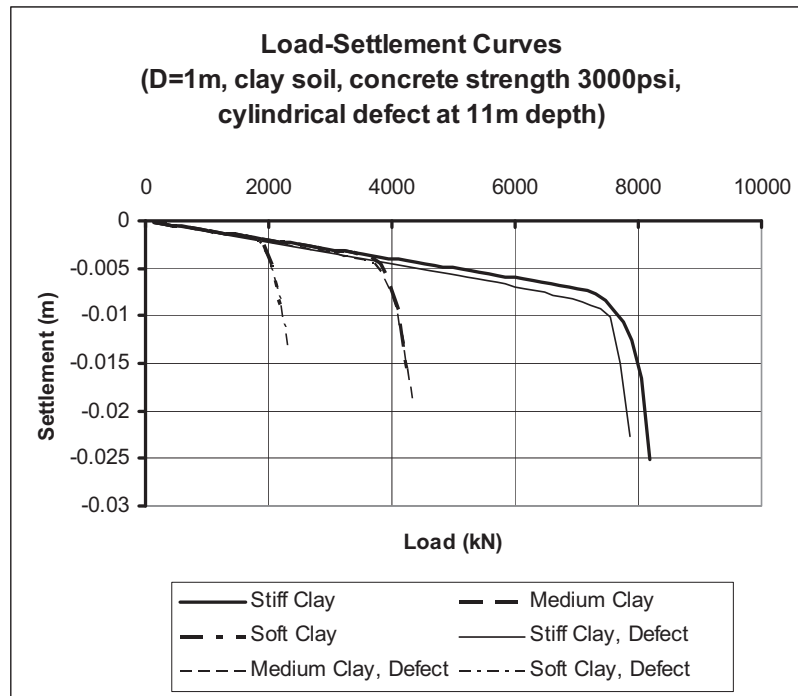


Figure 82. Load-settlement curves for drilled shafts of 1-m diameter in clay (Concrete strength 4,500 psi, 1-m length cylindrical anomaly at 11-m depth).

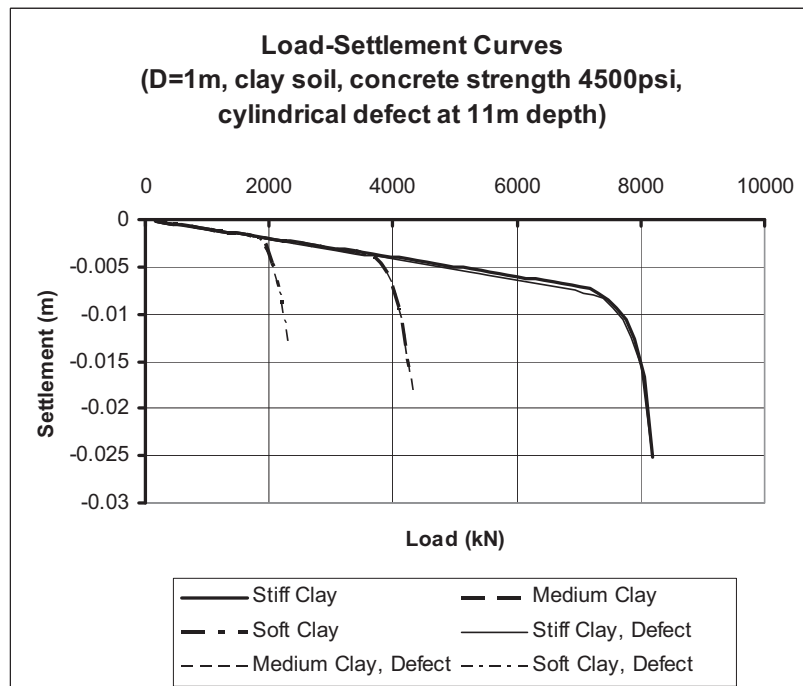


Figure 83. Load-settlement curves for drilled shafts of 1-m diameter in clay (Concrete strength 4,500 psi, 1-m length cylindrical anomaly at 11-m depth).

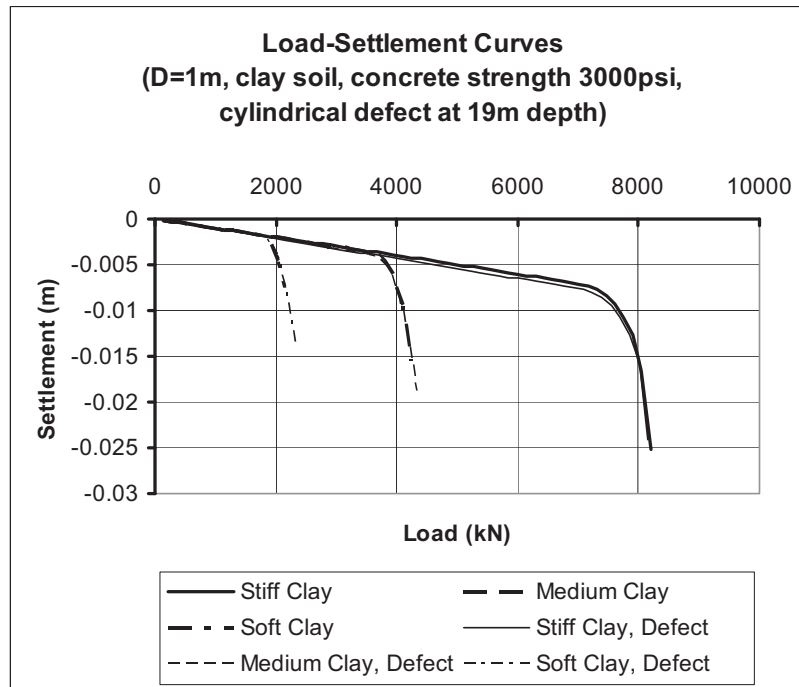


Figure 84. Load-settlement curves for drilled shafts of 1-m diameter in clay (Concrete strength 4,500 psi, 1.2-m length cylindrical anomaly at 19-m depth).

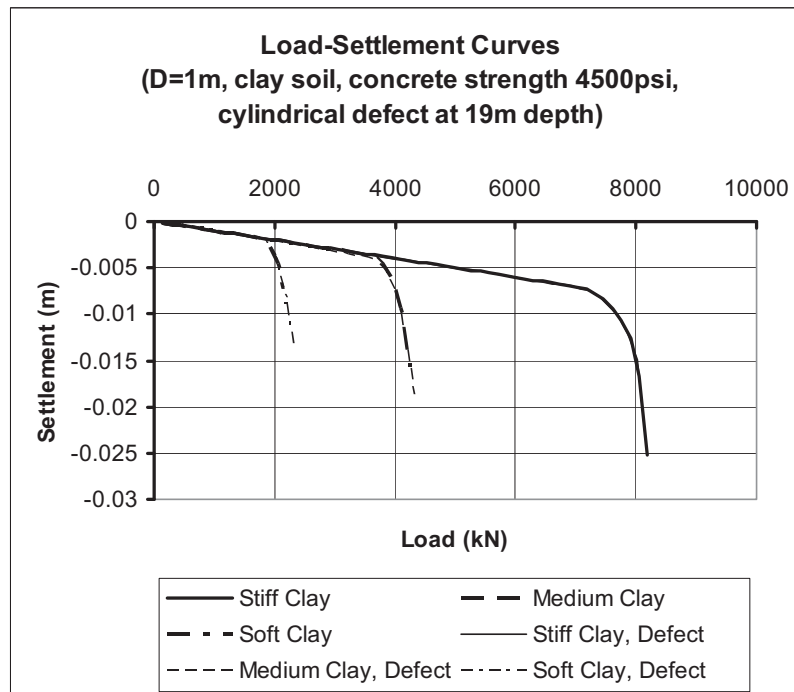


Figure 85. Load-settlement curves for drilled shafts of 1-m diameter in clay (Concrete strength 4,500 psi, 1.2-m length cylindrical anomaly at 19-m depth).

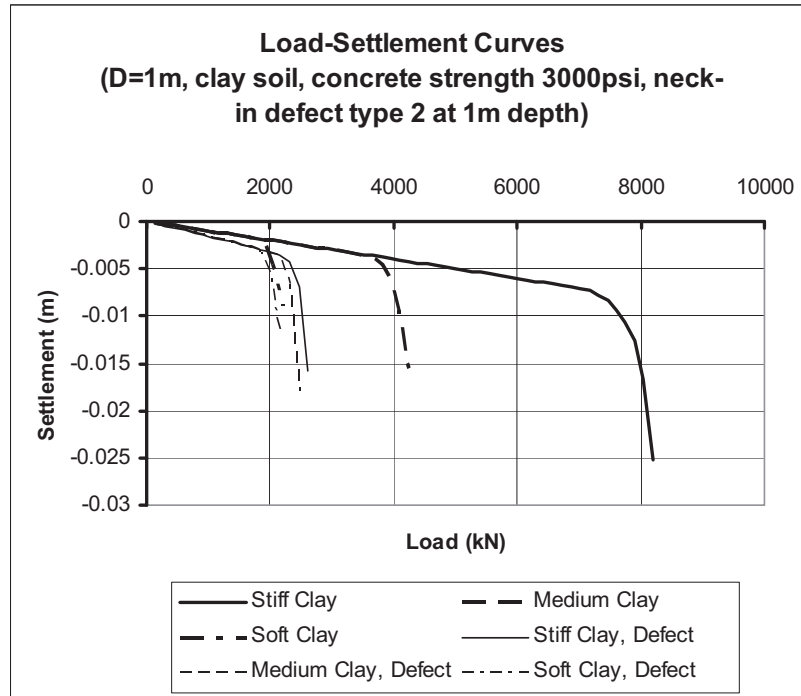


Figure 86. Load-settlement curves for drilled shafts of 1-m diameter in clay (Concrete strength 3,000 psi, 1-m length neck-in anomaly type 2 at 1-m depth).

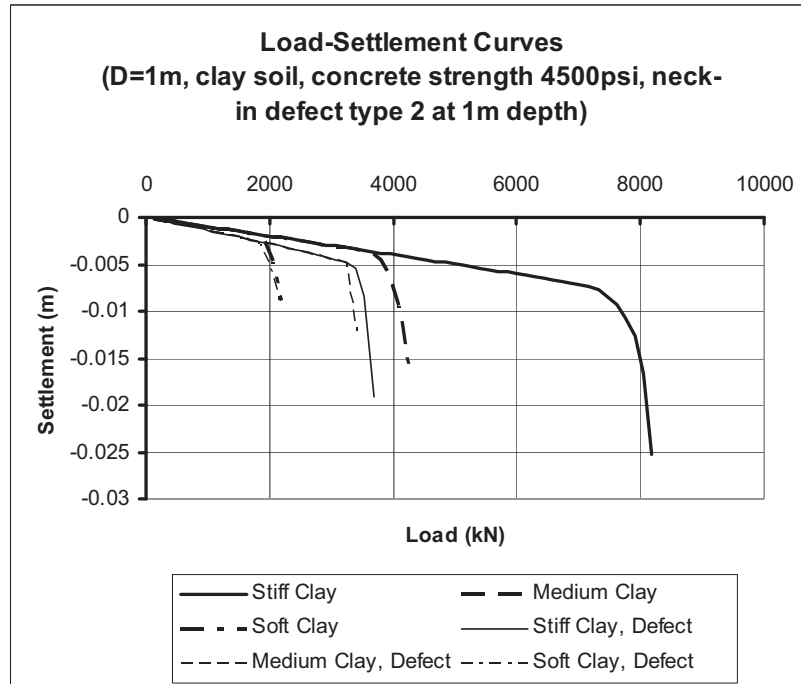


Figure 87. Load-settlement curves for drilled shafts of 1-m diameter in clay (Concrete strength 4,500 psi, 1-m length neck-in anomaly type 2 at 1-m depth).

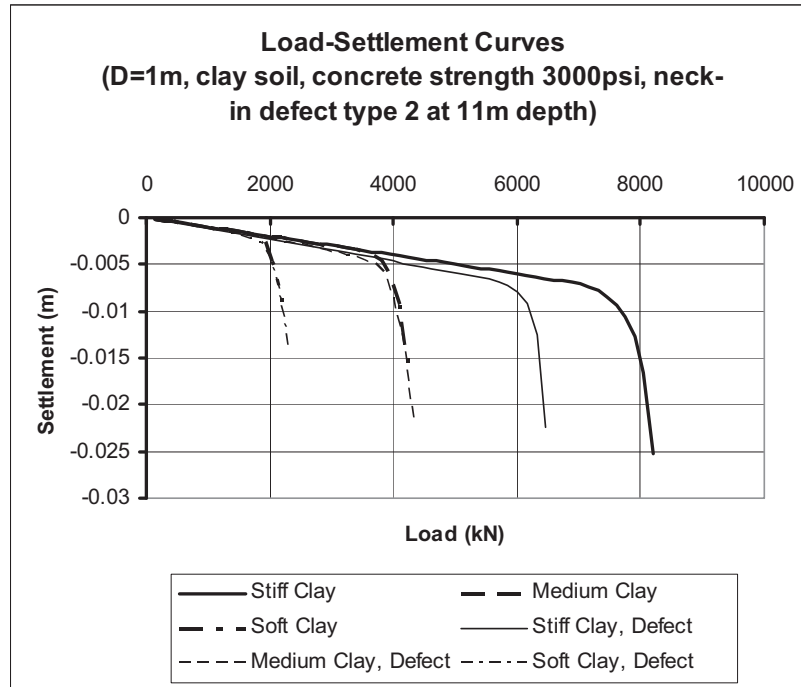


Figure 88. Load-settlement curves for drilled shafts of 1-m diameter in clay (Concrete strength 3,000 psi, 1-m length neck-in anomaly type 2 at 11-m depth).

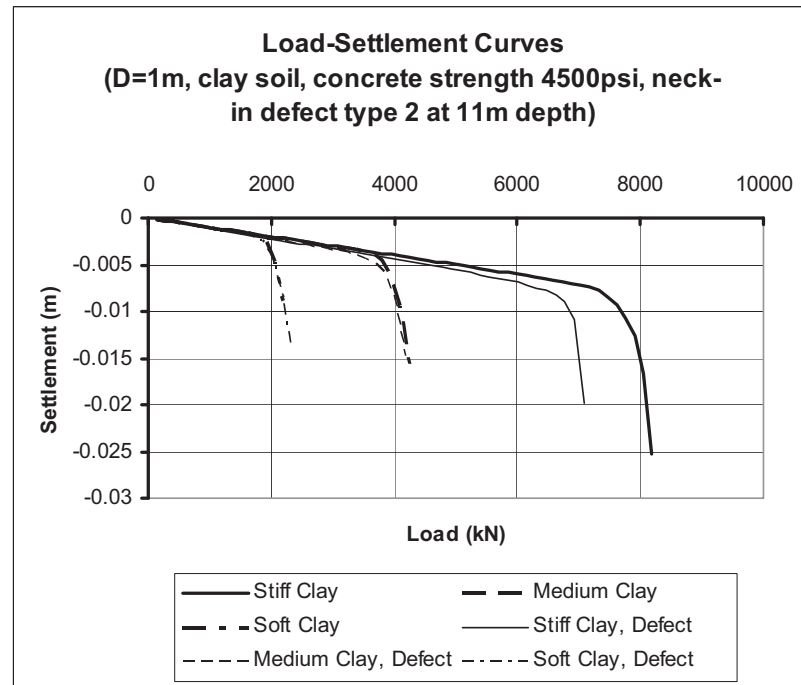


Figure 89. Load-settlement curves for drilled shafts of 1-m diameter in clay (Concrete strength 4,500 psi, 1-m length neck-in anomaly type 2 at 11-m depth).

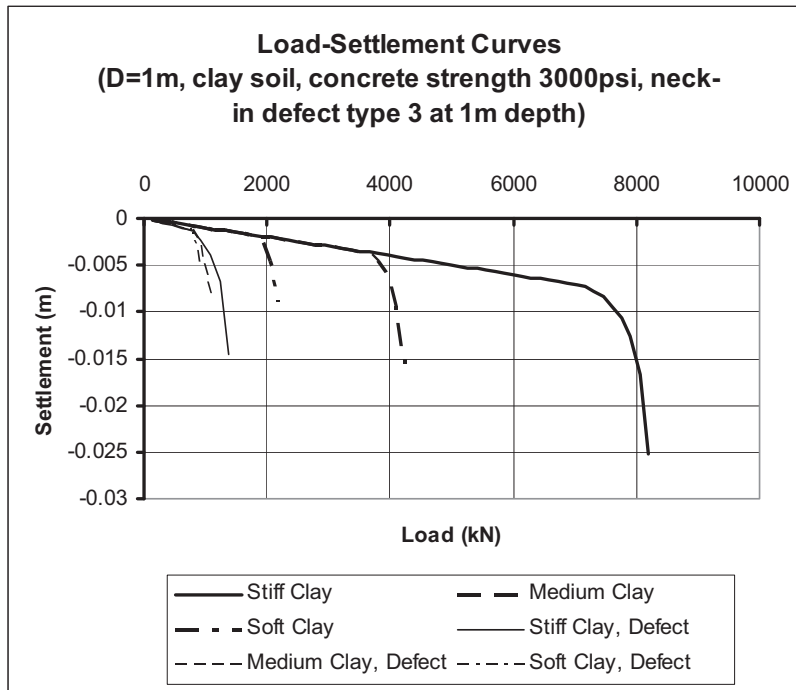


Figure 90. Load-settlement curves for drilled shafts of 1-m diameter in clay (Concrete strength 3,000 psi, 1-m length neck-in anomaly type 3 at 1-m depth).

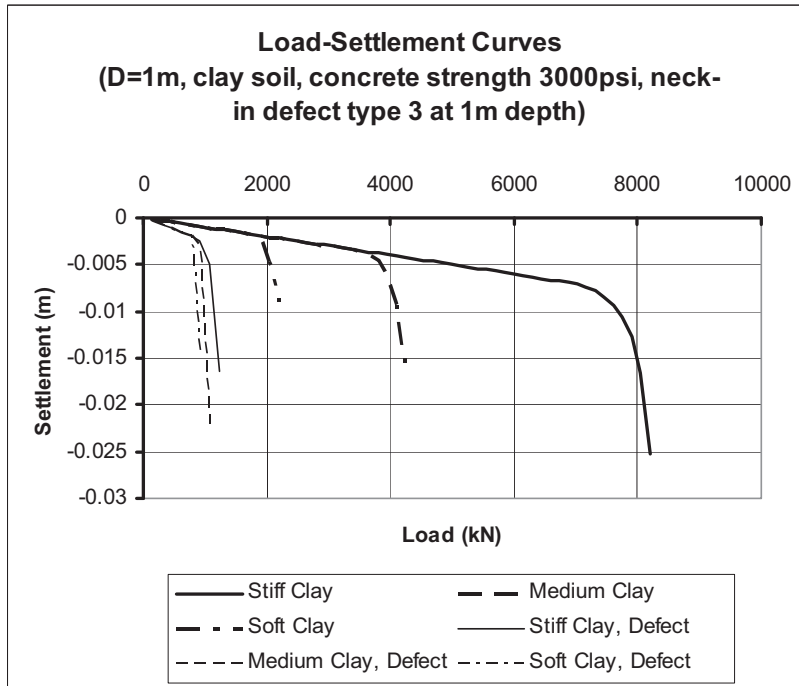


Figure 91. Load-settlement curves for drilled shafts of 1-m diameter in clay (Concrete strength 4,500 psi, 1-m length neck-in anomaly type 3 at 1-m depth).

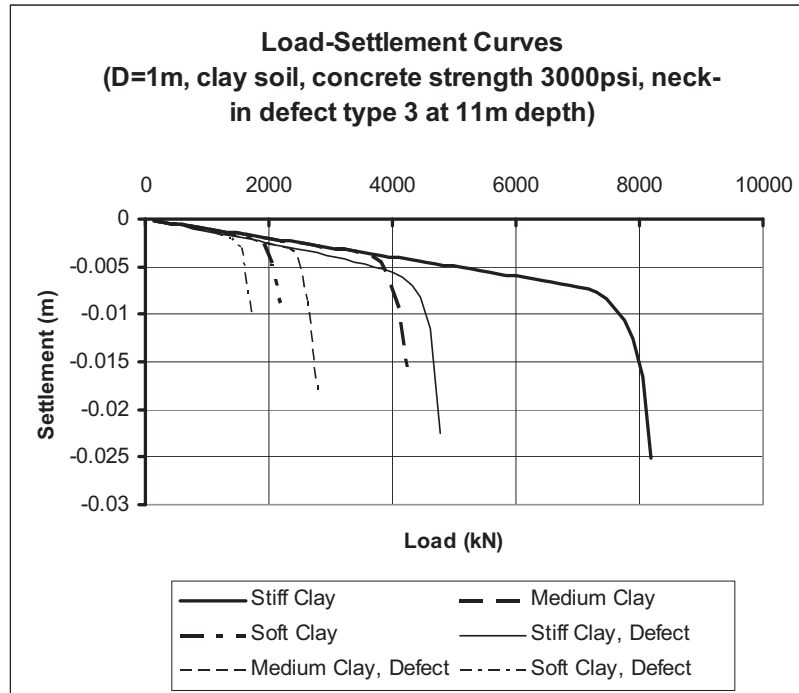


Figure 92. Load-settlement curves for drilled shafts of 1-m diameter in clay (Concrete strength 3,000 psi, 1-m length neck-in anomaly type 3 at 11-m depth).

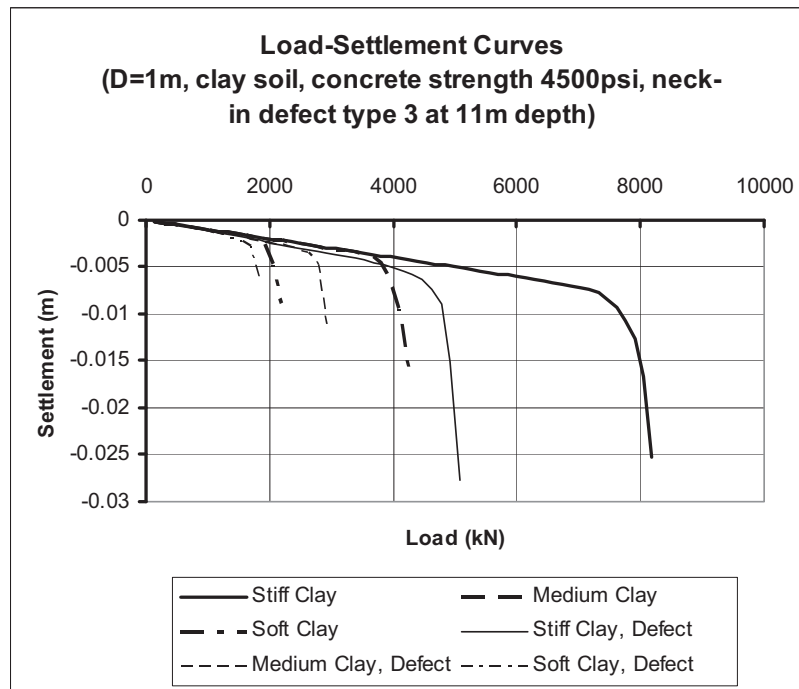


Figure 93. Load-settlement curves for drilled shafts of 1-m diameter in clay (Concrete strength 4,500 psi, 1-m length neck-in anomaly type 3 at 11-m depth).

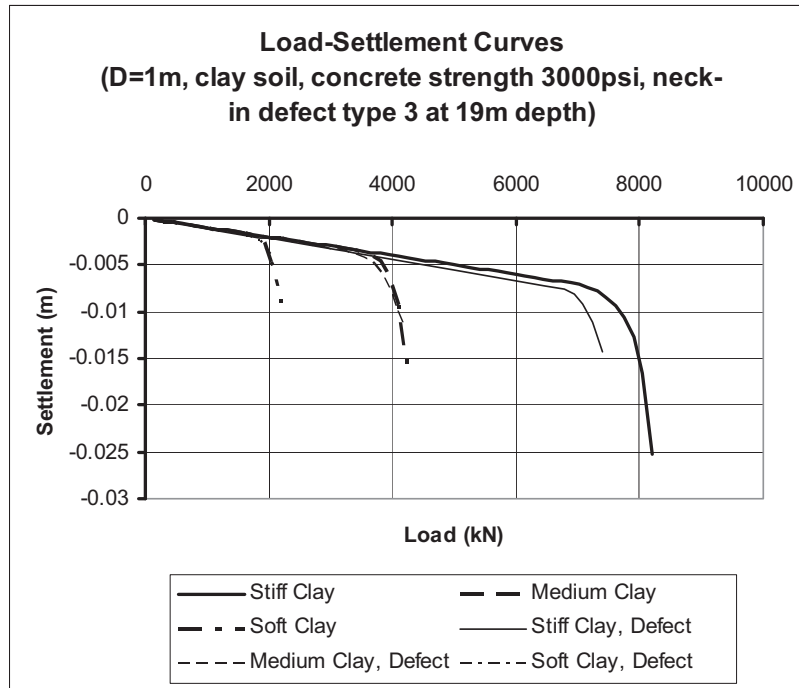


Figure 94. Load-settlement curves for drilled shafts of 1-m diameter in clay (Concrete strength 3,000 psi, 1-m length neck-in anomaly type 3 at 19-m depth).

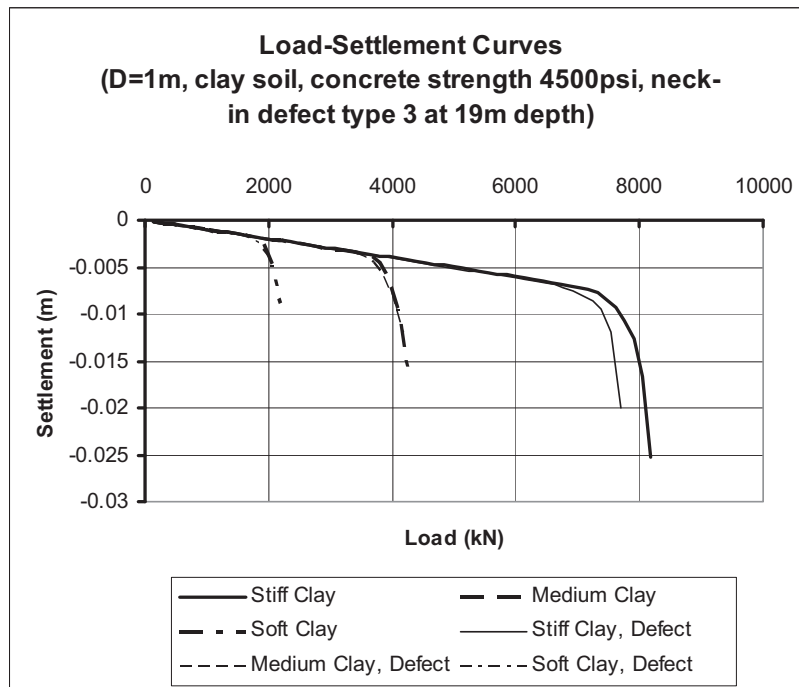


Figure 95. Load-settlement curves for drilled shafts of 1-m diameter in clay (Concrete strength 4,500 psi, 1-m length neck-in anomaly type 3 at 19-m depth).

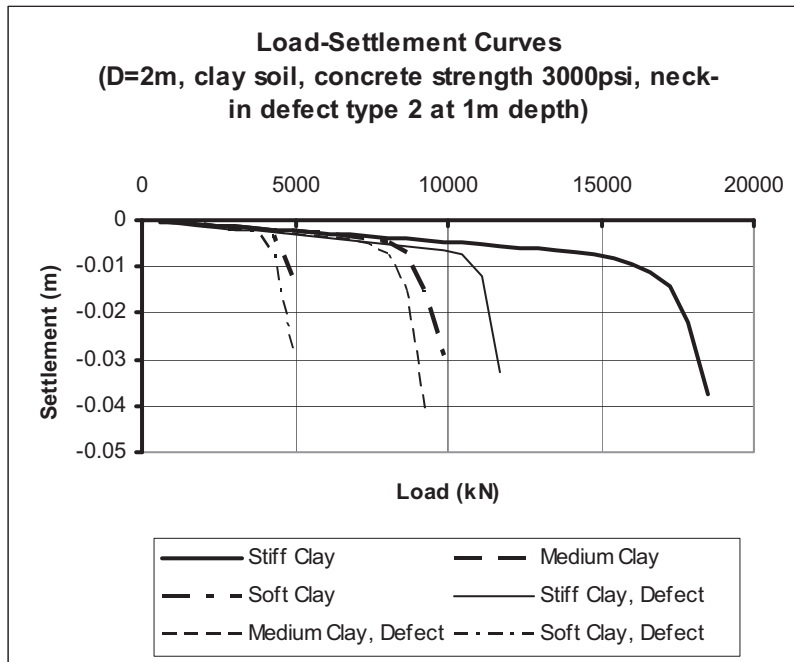


Figure 96. Load-settlement curves for drilled shafts of 2-m diameter in clay (Concrete strength 3,000 psi, 1-m length neck-in anomaly type 2 at 1-m depth).

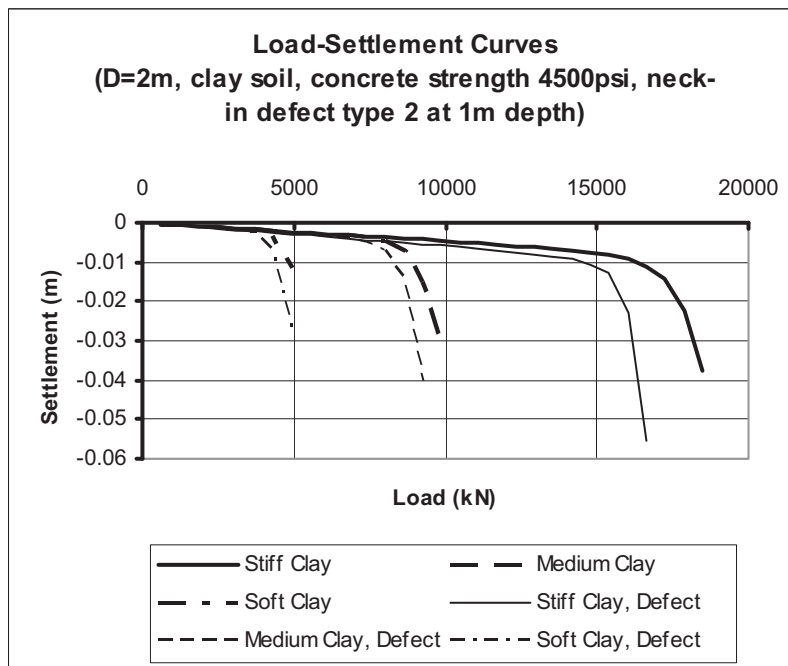


Figure 97. Load-settlement curves for drilled shafts of 2-m diameter in clay (Concrete strength 4,500 psi, 1-m length neck-in anomaly type 2 at 1-m depth).

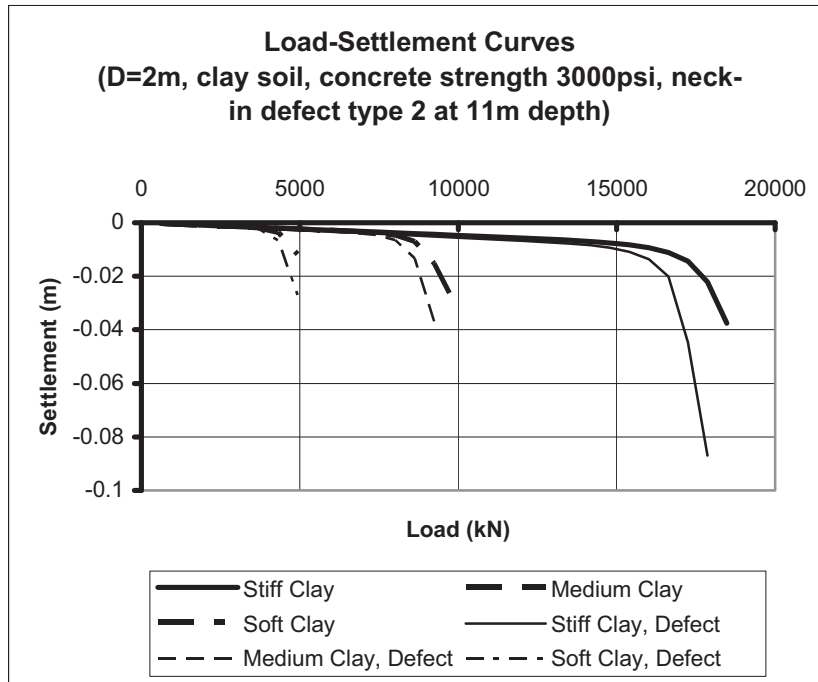


Figure 98. Load-settlement curves for drilled shafts of 2-m diameter in clay (Concrete strength 3,000 psi, 1-m length neck-in anomaly type 2 at 11-m depth).

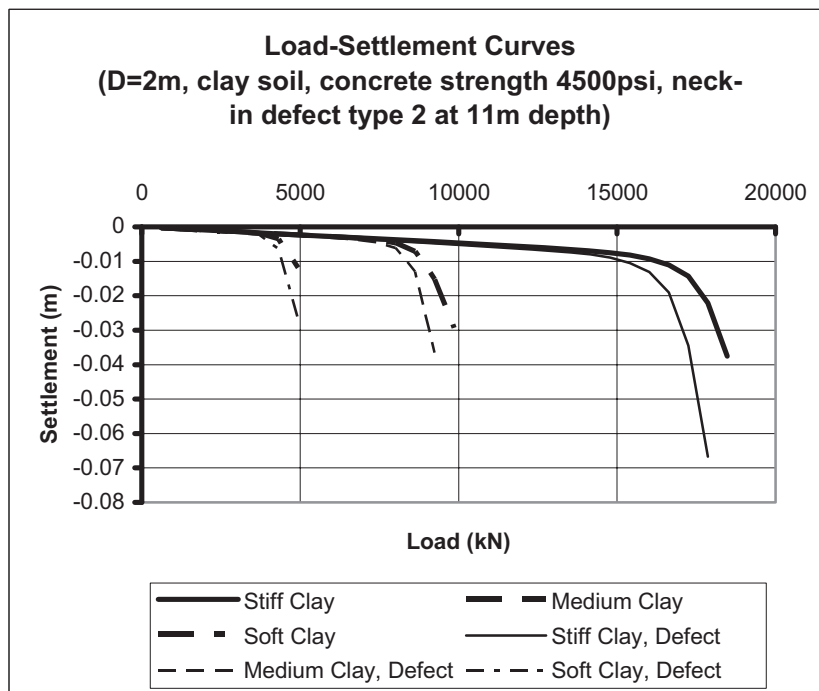


Figure 99. Load-settlement curves for drilled shafts of 2-m diameter in clay (Concrete strength 4,500 psi, 1-m length neck-in anomaly type 2 at 11-m depth).

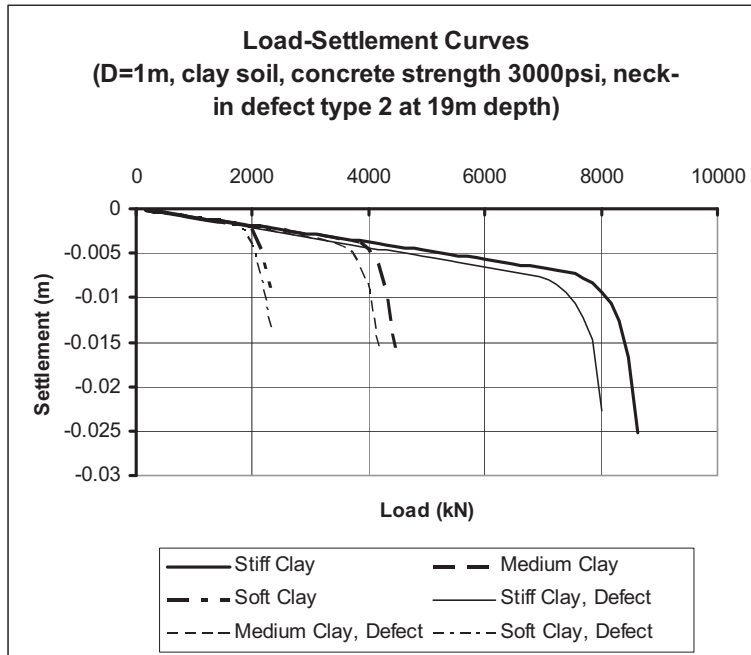


Figure 100. Load-settlement curves for drilled shafts of 2-m diameter in clay (Concrete strength 3,000 psi, 1.2-m length neck-in anomaly type 2 at 19-m depth).

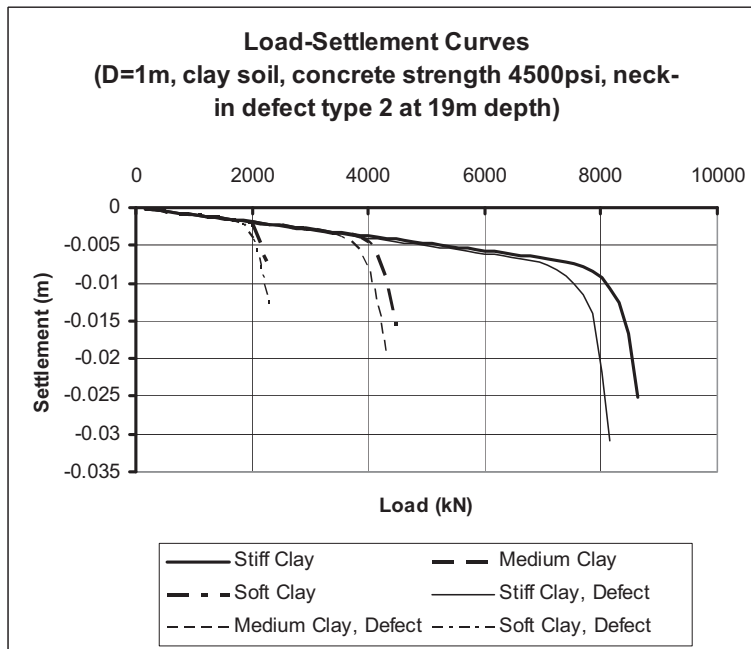


Figure 101. Load-settlement curves for drilled shafts of 2-m diameter in clay (Concrete strength 4,500 psi, 1.2-m length neck-in anomaly type 2 at 19-m depth).

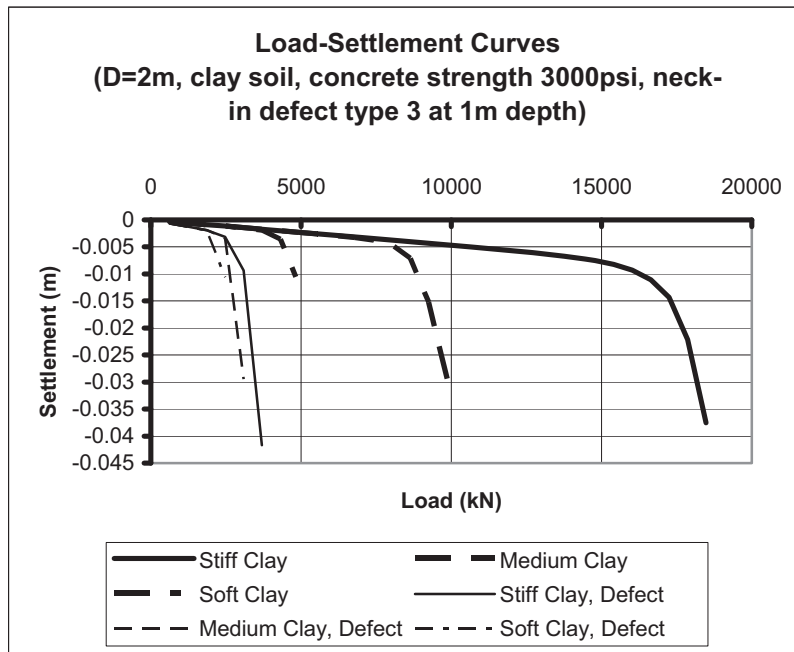


Figure 102. Load-settlement curves for drilled shafts of 2-m diameter in clay (Concrete strength 3,000 psi, 1-m length neck-in anomaly type 3 at 1-m depth).

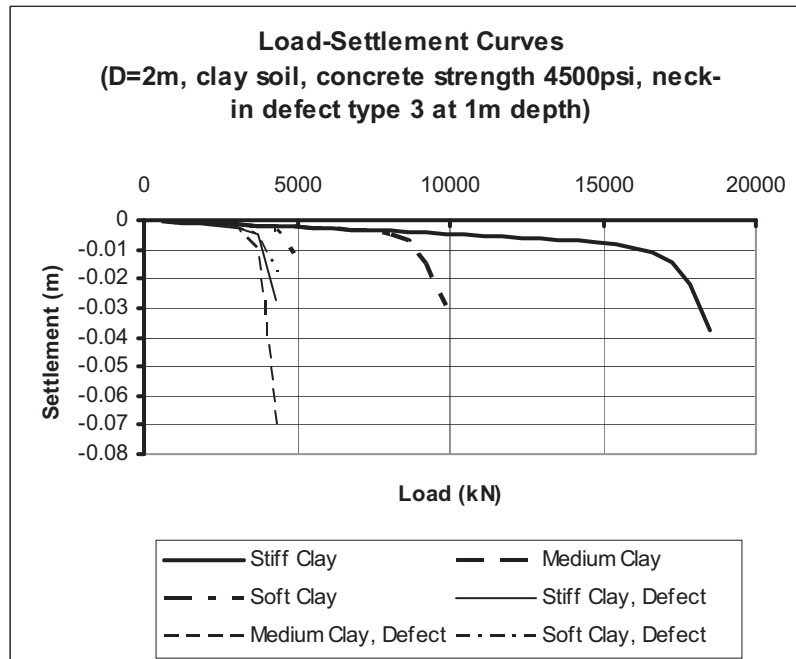


Figure 103. Load-settlement curves for drilled shafts of 2-m diameter in clay (Concrete strength 4,500 psi, 1-m length neck-in anomaly type 3 at 1-m depth).

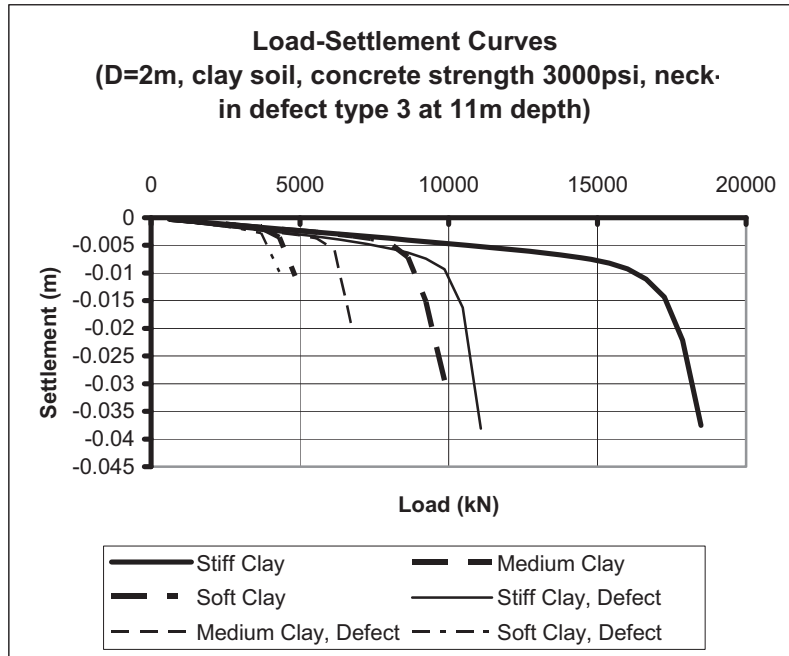


Figure 104. Load-settlement curves for drilled shafts of 2-m diameter in clay (Concrete strength 3,000 psi, 1-m length neck-in anomaly type 3 at 11-m depth).

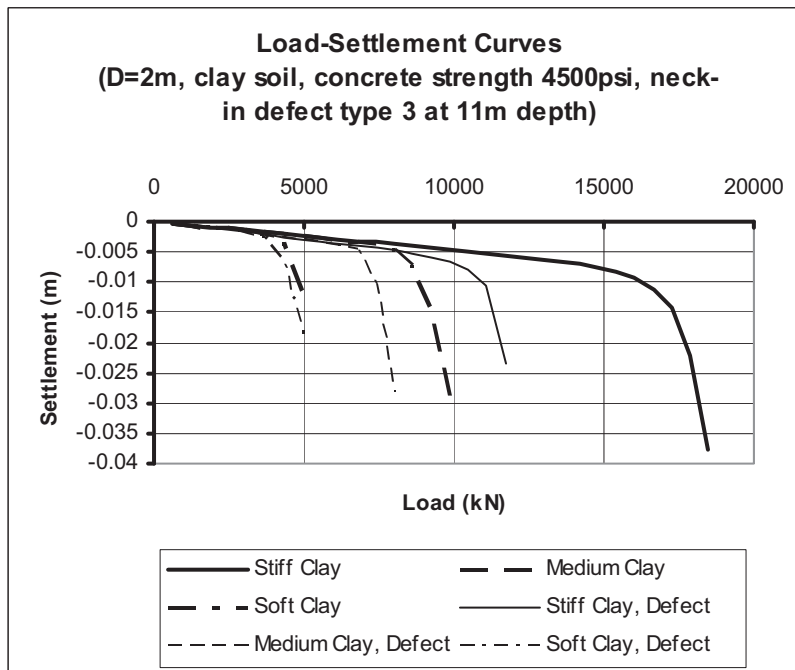


Figure 105. Load-settlement curves for drilled shafts of 2-m diameter in clay (Concrete strength 4,500 psi, 1-m length neck-in anomaly type 3 at 11-m depth).

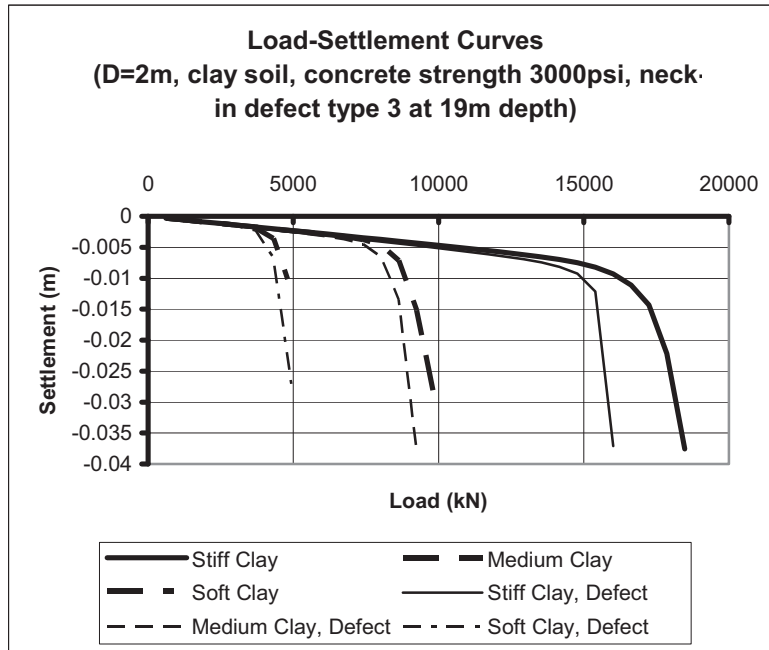


Figure 106. Load-settlement curves for drilled shafts of 2-m diameter in clay (Concrete strength 3,000 psi, 1.2-m length neck-in anomaly type 3 at 19-m depth).

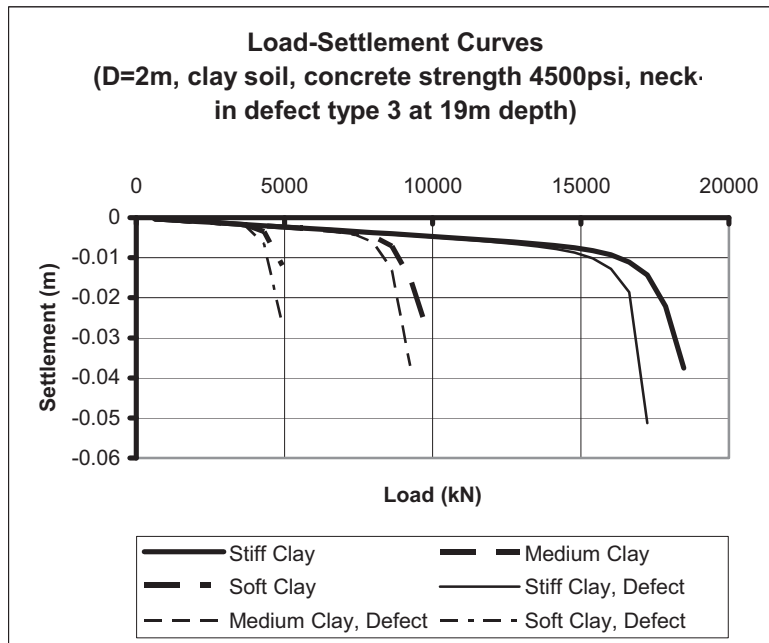


Figure 107. Load-settlement curves for drilled shafts of 2-m diameter in clay (Concrete strength 4,500 psi, 1.2-m length neck-in anomaly type 3 at 19-m depth).

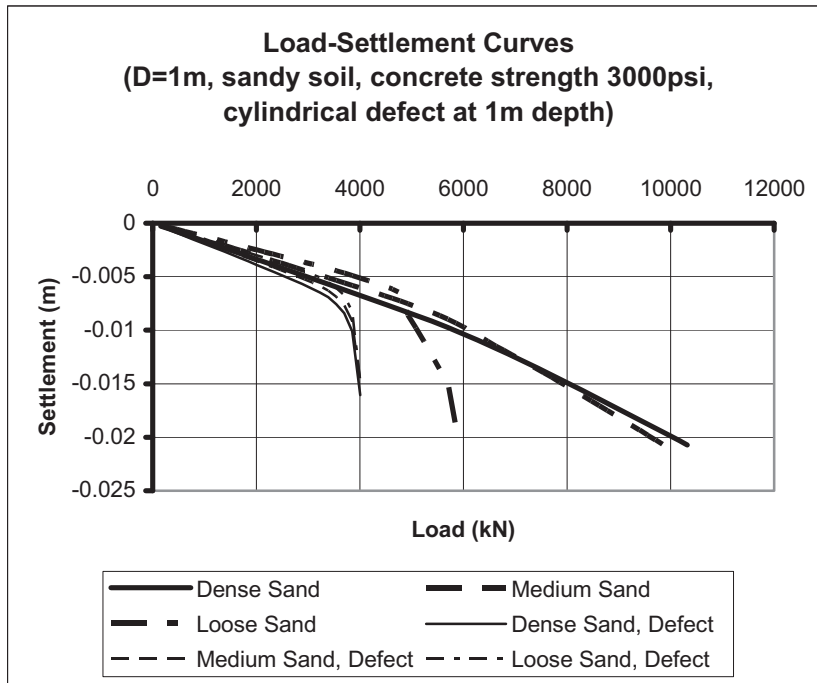


Figure 108. Load-settlement curves for drilled shafts of 1-m diameter in sand (Concrete strength 3,000 psi, 1-m length cylindrical anomaly at 1-m depth).

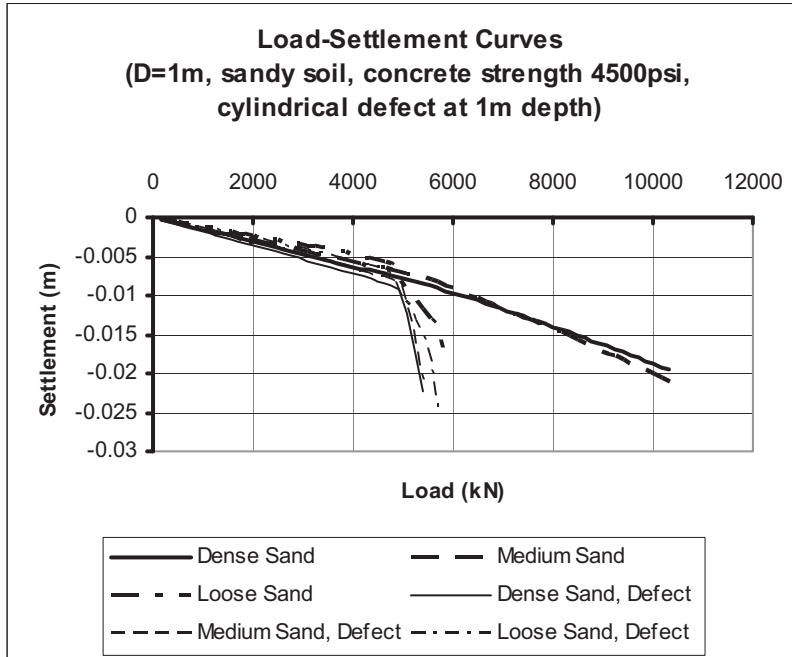


Figure 109. Load-settlement curves for drilled shafts of 1-m diameter in sand (Concrete strength 4,500 psi, 1-m length cylindrical anomaly at 1-m depth).

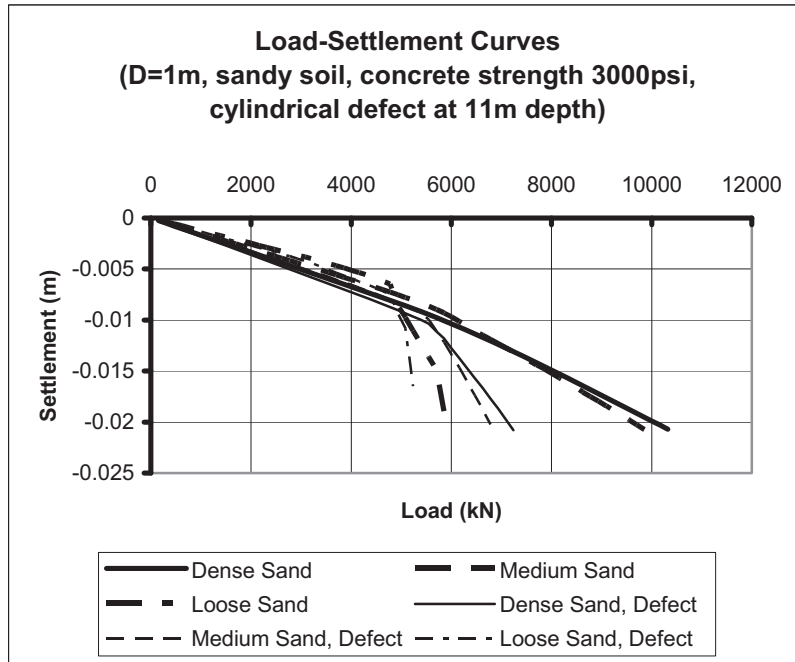


Figure 110. Load-settlement curves for drilled shafts of 1-m diameter in sand (Concrete strength 3,000 psi, 1-m length cylindrical anomaly at 11-m depth).

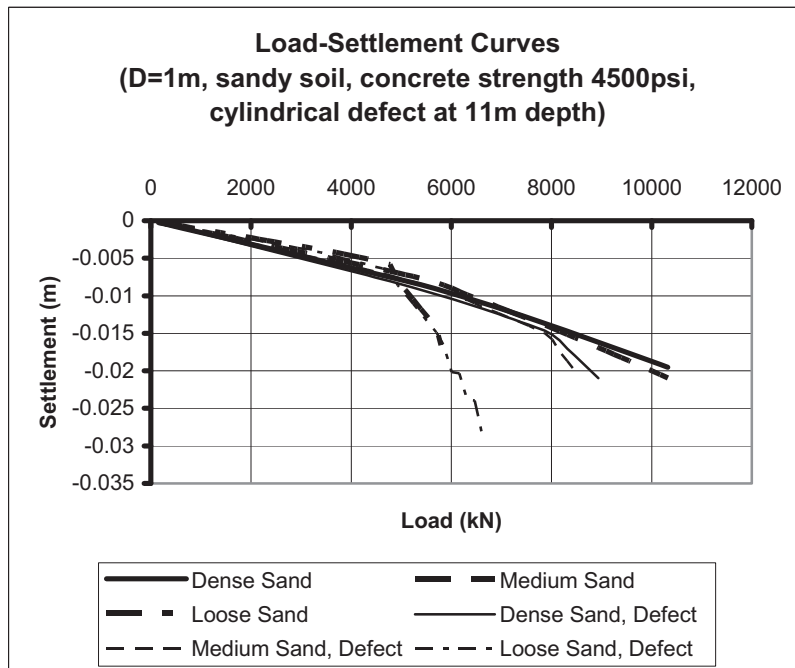


Figure 111. Load-settlement curves for drilled shafts of 1-m diameter in sand (Concrete strength 4,500 psi, 1-m length cylindrical anomaly at 11-m depth).

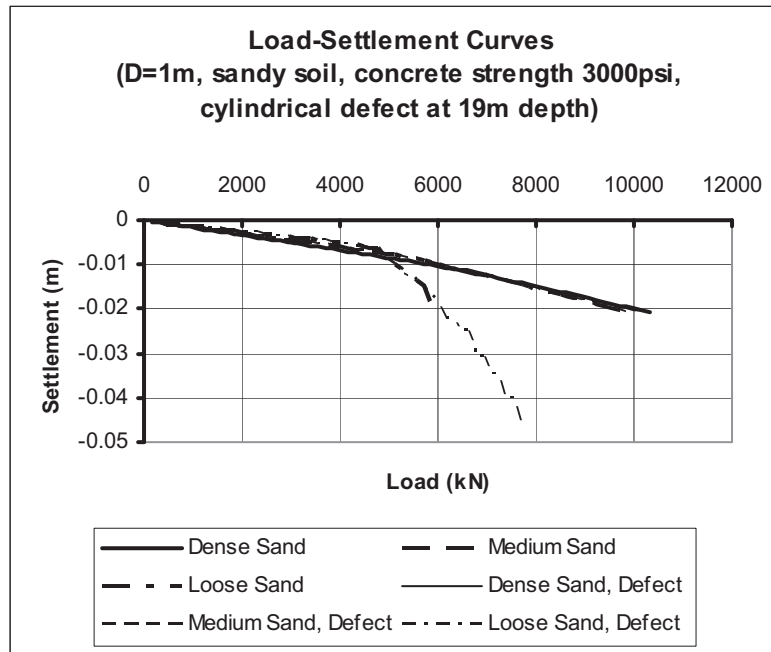


Figure 112. Load-settlement curves for drilled shafts of 1-m diameter in sand (Concrete strength 3,000 psi, 1-m length cylindrical anomaly at 11-m depth).

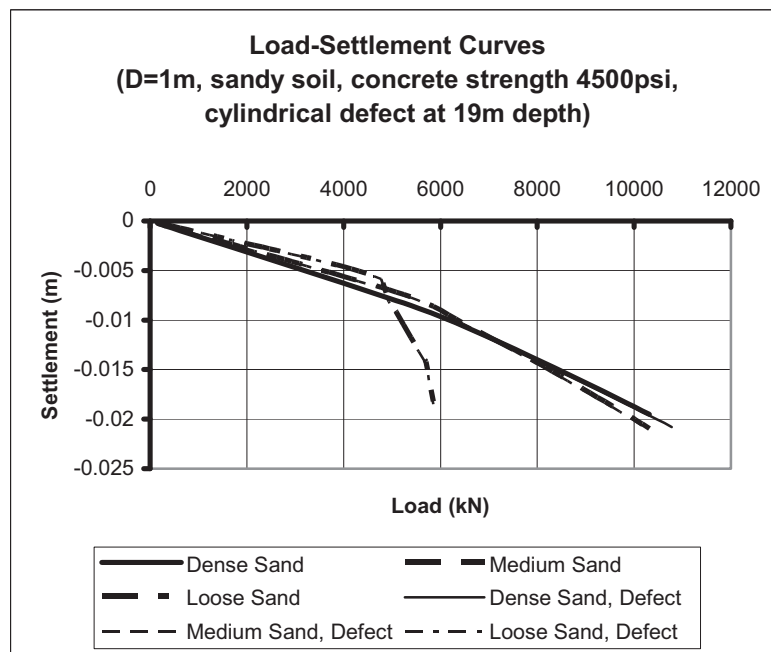


Figure 113. Load-settlement curves for drilled shafts of 1-m diameter in sand (Concrete strength 4,500 psi, 1-m length cylindrical anomaly at 11-m depth).

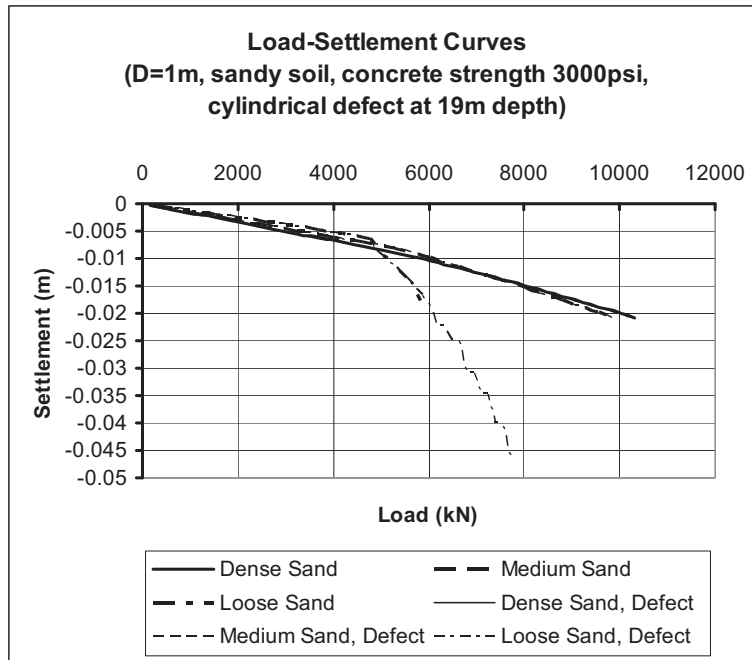


Figure 114. Load-settlement curves for drilled shafts of 1-m diameter in sand (Concrete strength 3,000 psi, 1.2-m length cylindrical anomaly at 19-m depth).

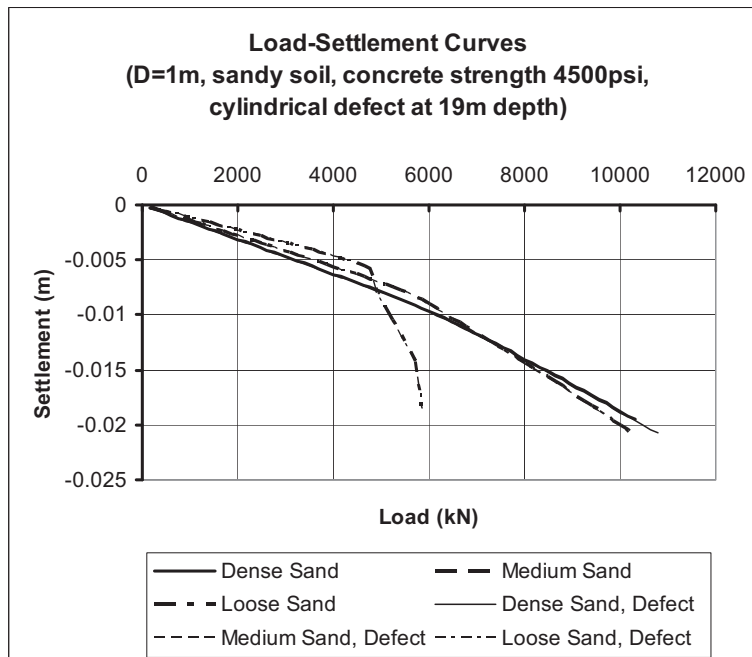


Figure 115. Load-settlement curves for drilled shafts of 1-m diameter in sand (Concrete strength 4,500 psi, 1.2-m length cylindrical anomaly at 19-m depth).

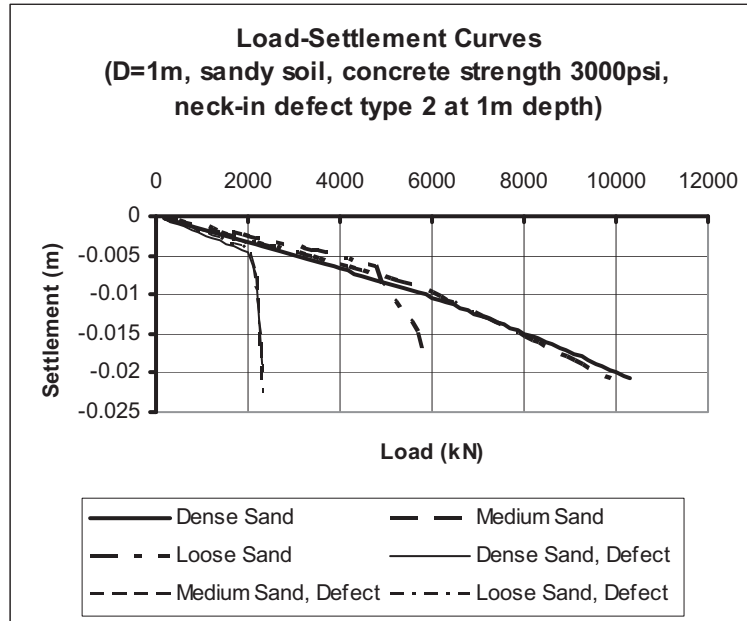


Figure 116. Load-settlement curves for drilled shafts of 1-m diameter in sand (Concrete strength 3,000 psi, 1-m length neck-in anomaly type 2 at 1-m depth).

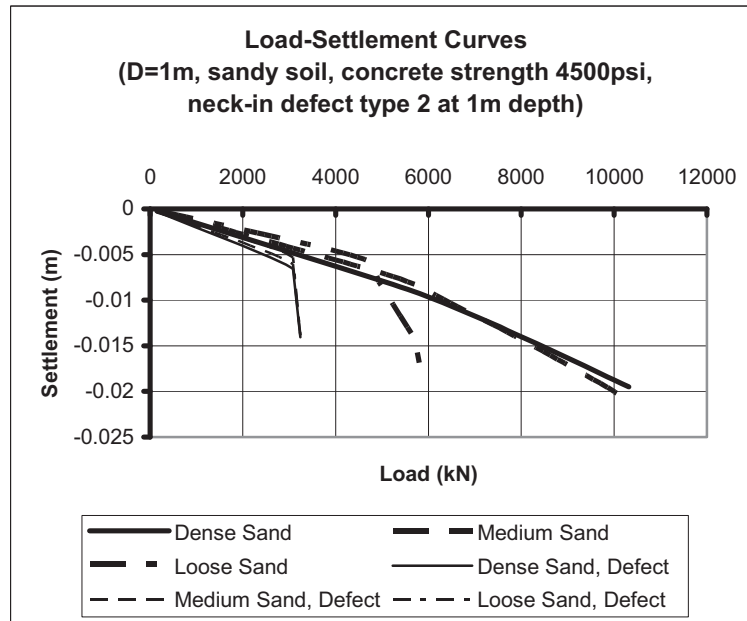


Figure 117. Load-settlement curves for drilled shafts of 1-m diameter in sand (Concrete strength 4,500 psi, 1-m length neck-in anomaly type 2 at 1-m depth).

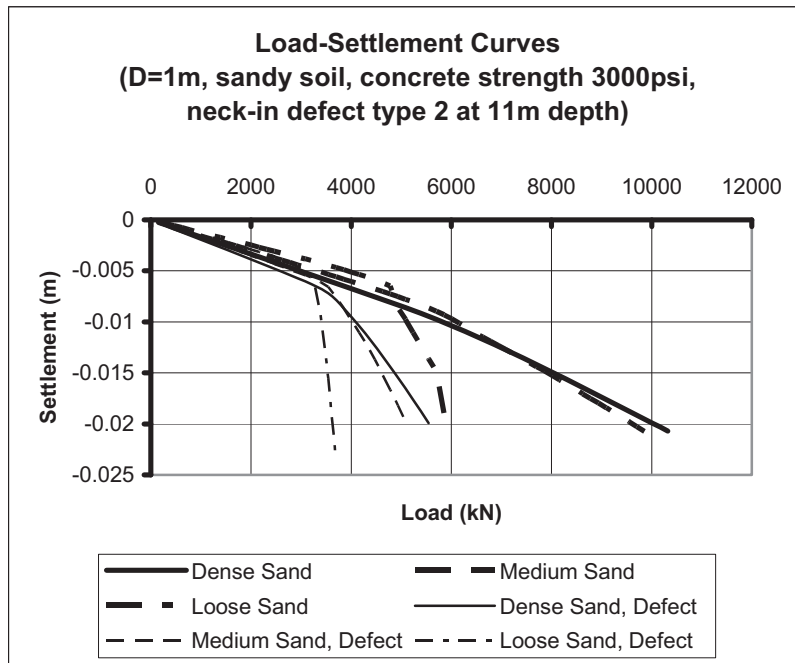


Figure 118. Load-settlement curves for drilled shafts of 1-m diameter in sand (Concrete strength 3,000 psi, 1-m length neck-in anomaly type 2 at 11-m depth).

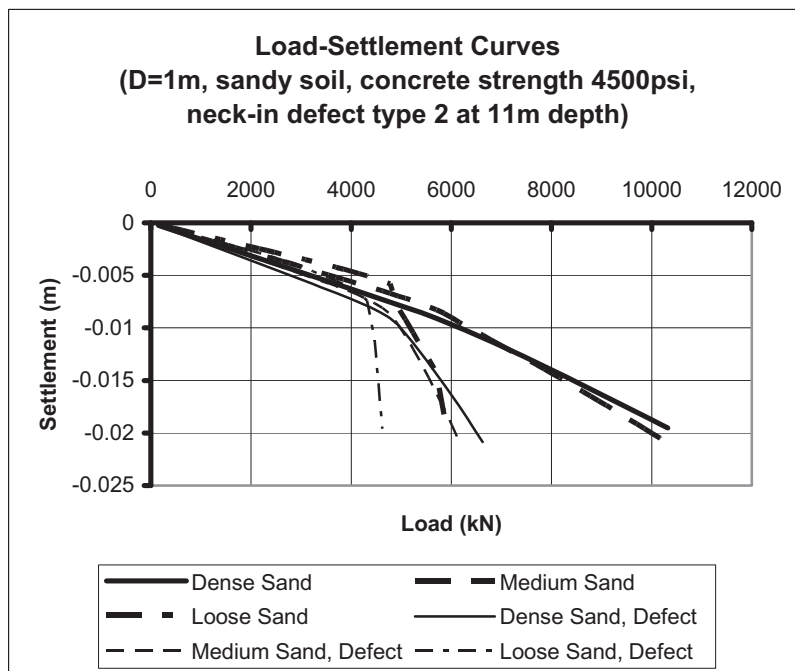


Figure 119. Load-settlement curves for drilled shafts of 1-m diameter in sand (Concrete strength 4,500 psi, 1-m length neck-in anomaly type 2 at 11-m depth).

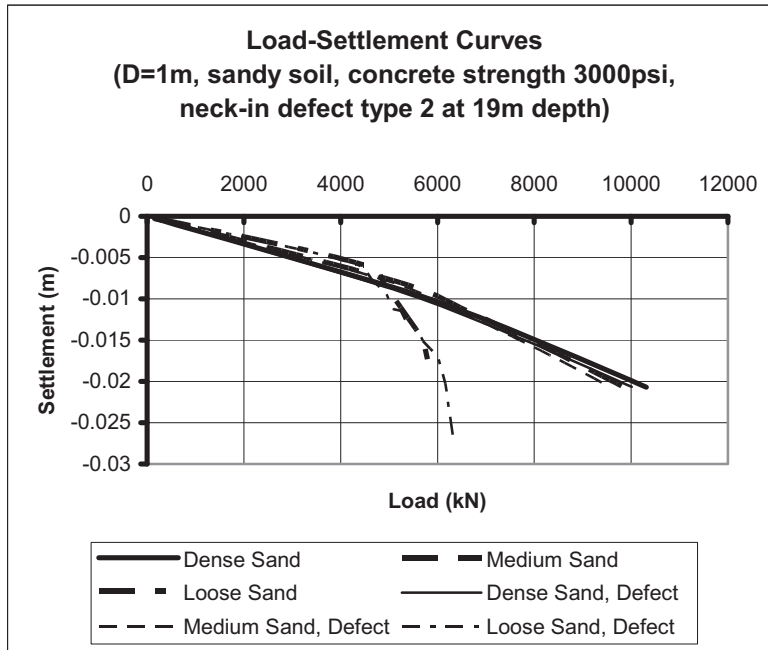


Figure 120. Load-settlement curves for drilled shafts of 1-m diameter in sand (Concrete strength 3,000 psi, 1.2-m length neck-in anomaly type 2 at 19-m depth).

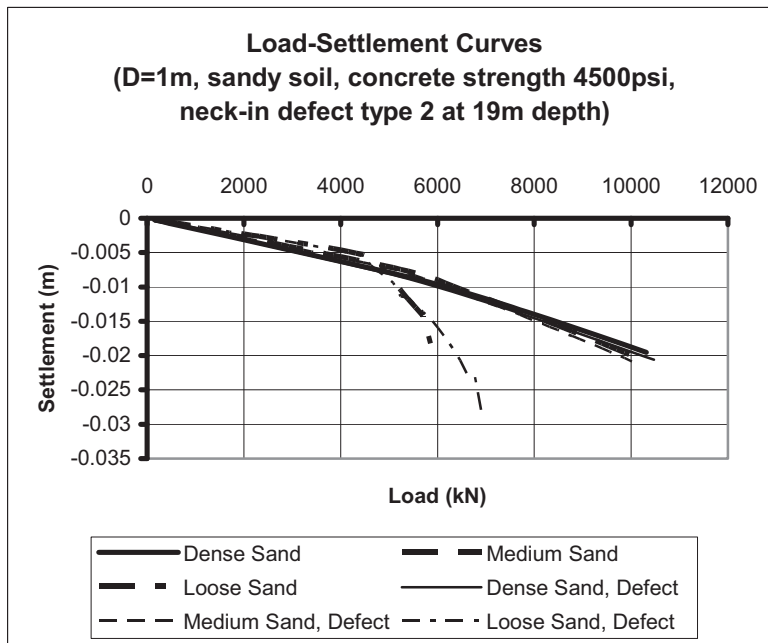


Figure 121. Load-settlement curves for drilled shafts of 1-m diameter in sand (Concrete strength 4,500 psi, 1.2-m length neck-in anomaly type 2 at 19-m depth).

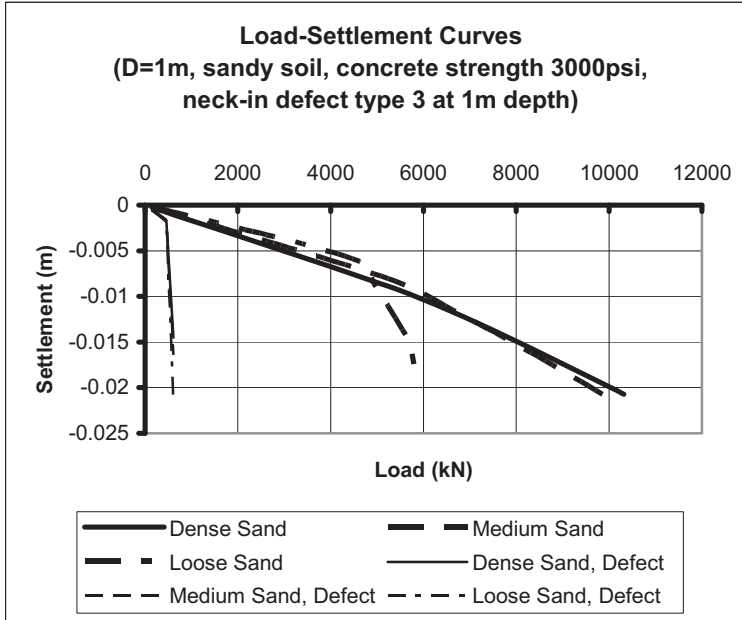


Figure 122. Load-settlement curves for drilled shafts of 1-m diameter in sand (Concrete strength 3,000 psi, 1-m length neck-in anomaly type 3 at 1-m depth).

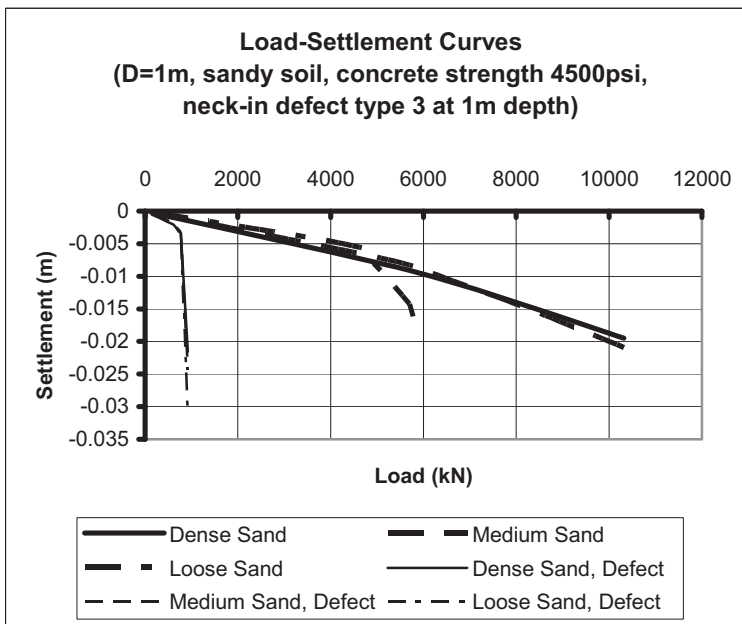


Figure 123. Load-settlement curves for drilled shafts of 1-m diameter in sand (Concrete strength 4,500 psi, 1-m length neck-in anomaly type 3 at 1-m depth).

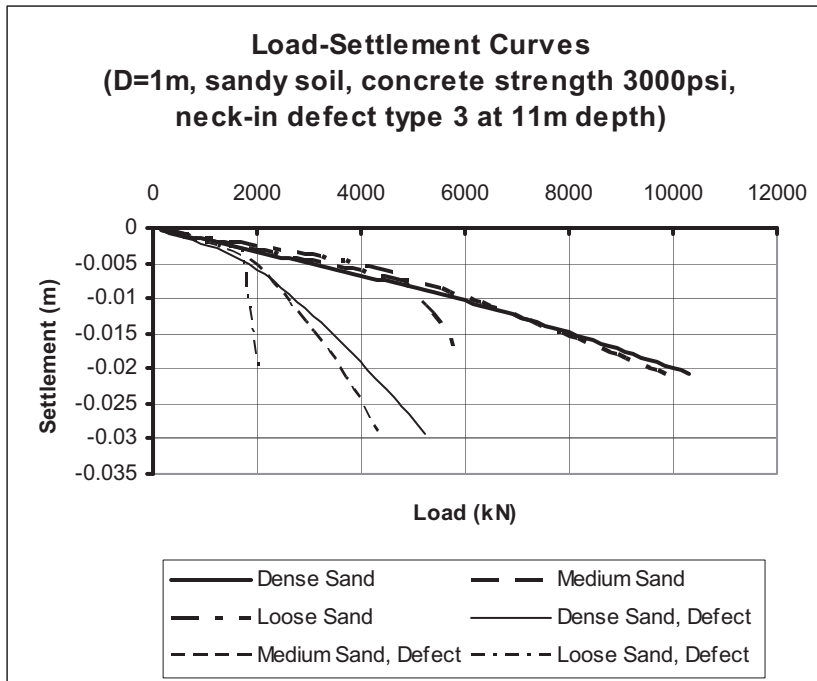


Figure 124. Load-settlement curves for drilled shafts of 1-m diameter in sand (Concrete strength 3,000 psi, 1-m length neck-in anomaly type 3 at 11-m depth).

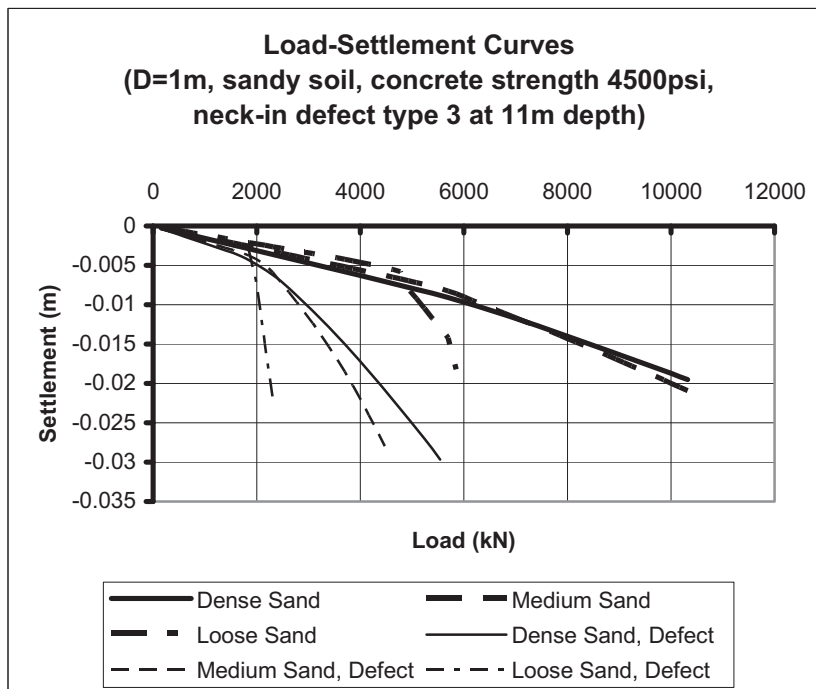


Figure 125. Load-settlement curves for drilled shafts of 1-m diameter in sand (Concrete strength 4,500 psi, 1-m length neck-in anomaly type 3 at 11-m depth).

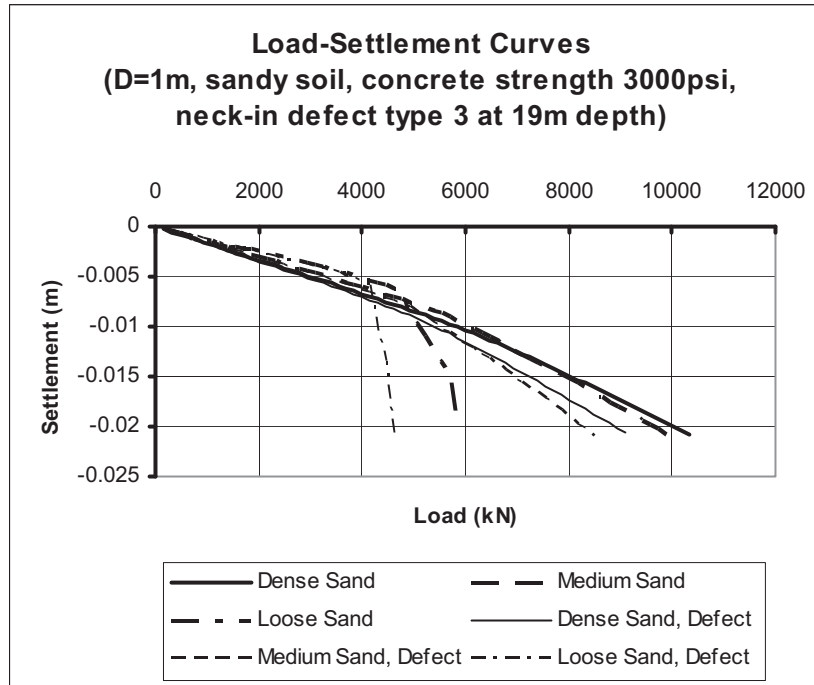


Figure 126. Load-settlement curves for drilled shafts of 1-m diameter in sand (Concrete strength 3,000 psi, 1.2-m length neck-in anomaly type 3 at 19-m depth).

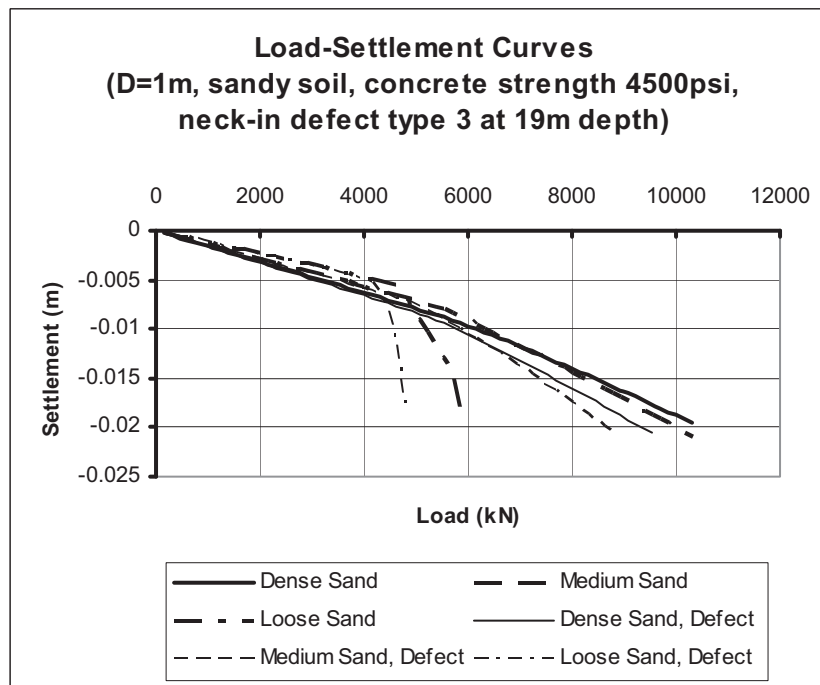


Figure 127. Load-settlement curves for drilled shafts of 1-m diameter in sand (Concrete strength 4,500 psi, 1.2-m length neck-in anomaly type 3 at 19-m depth).

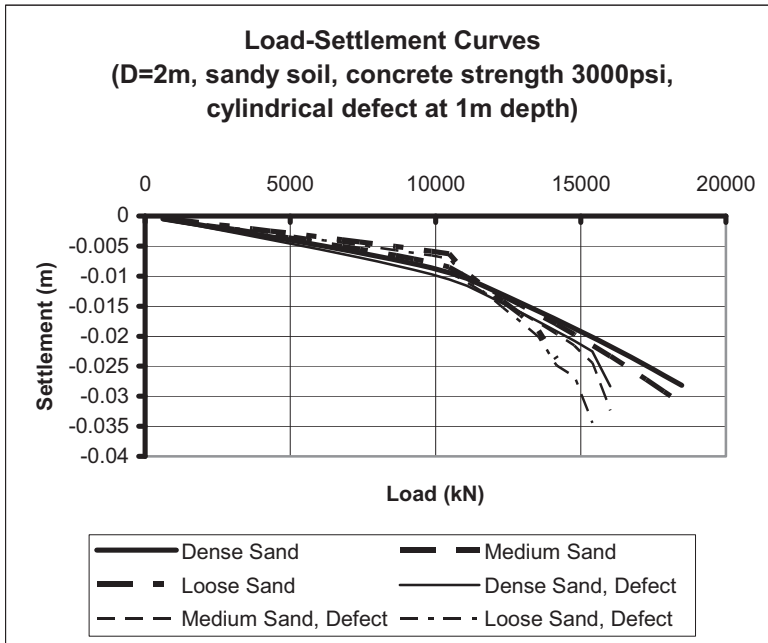


Figure 128. Load-settlement curves for drilled shafts of 2-m diameter in sand (Concrete strength 3,000 psi, 1-m length cylindrical anomaly at 1-m depth).

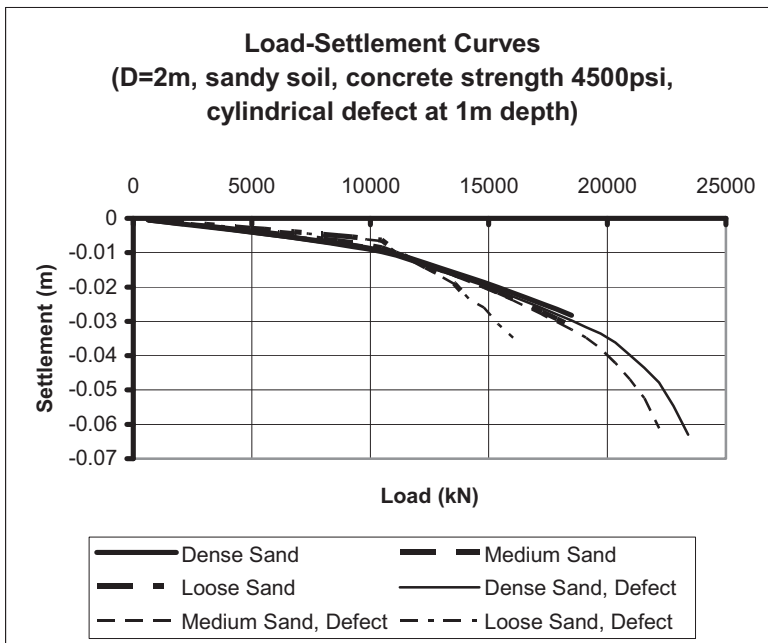


Figure 129. Load-settlement curves for drilled shafts of 2-m diameter in sand (Concrete strength 4,500 psi, 1-m length cylindrical anomaly at 1-m depth).

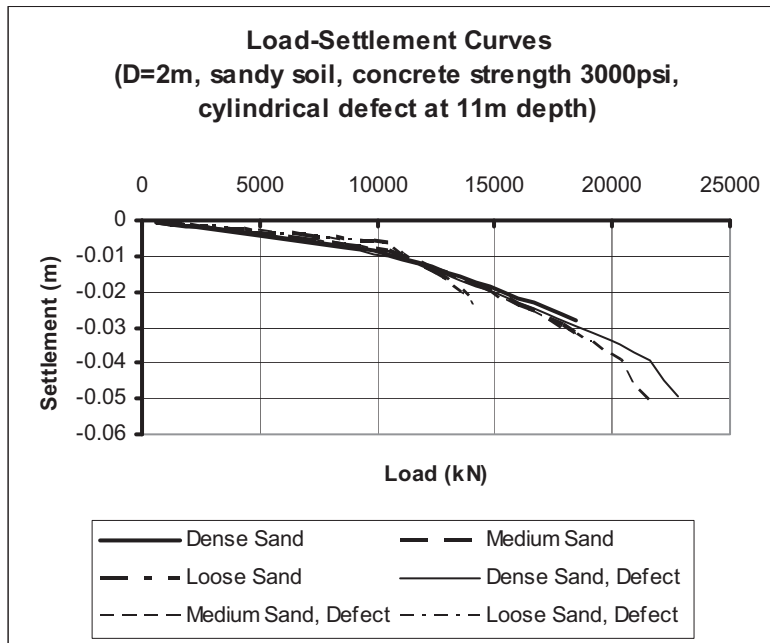


Figure 130. Load-settlement curves for drilled shafts of 2-m diameter in sand (Concrete strength 3,000 psi, 1-m length cylindrical anomaly at 11-m depth).

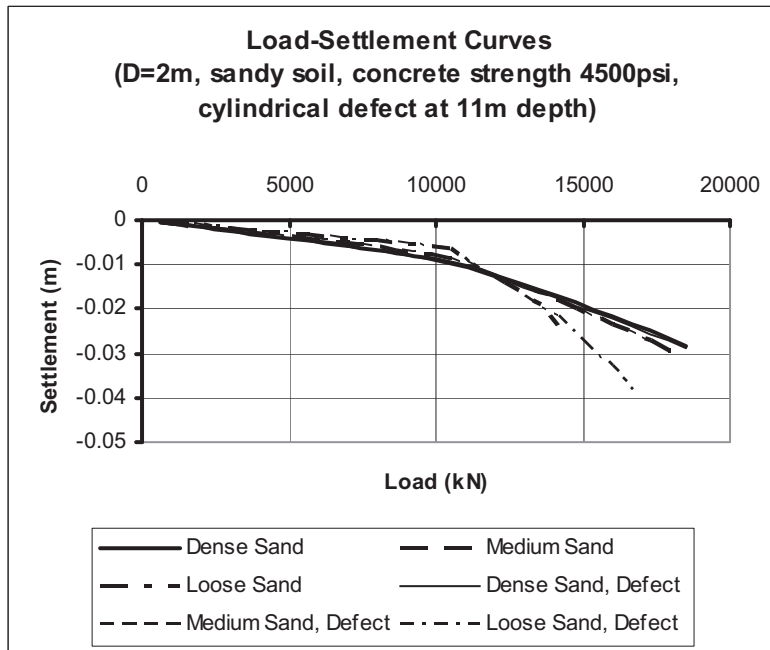


Figure 131. Load-settlement curves for drilled shafts of 2-m diameter in sand (Concrete strength 4,500 psi, 1-m length cylindrical anomaly at 11-m depth).

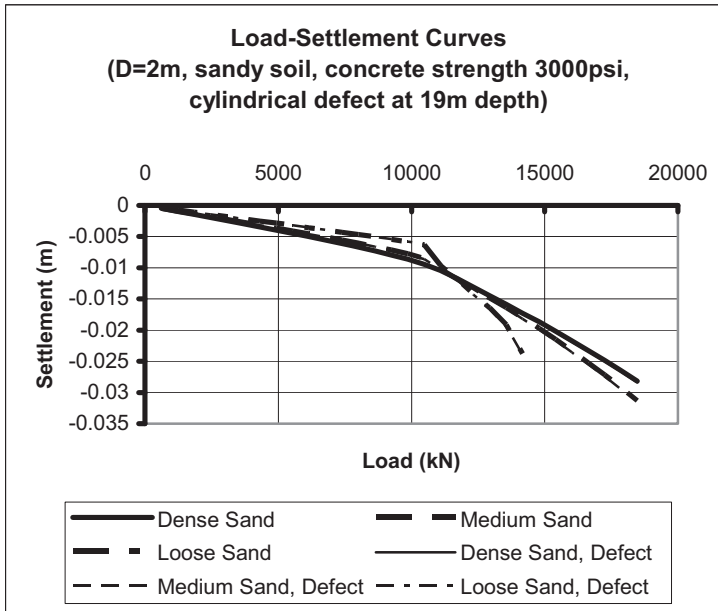


Figure 132. Load-settlement curves for drilled shafts of 2-m diameter in sand (Concrete strength 3,000 psi, 1.2-m length cylindrical anomaly at 19-m depth).

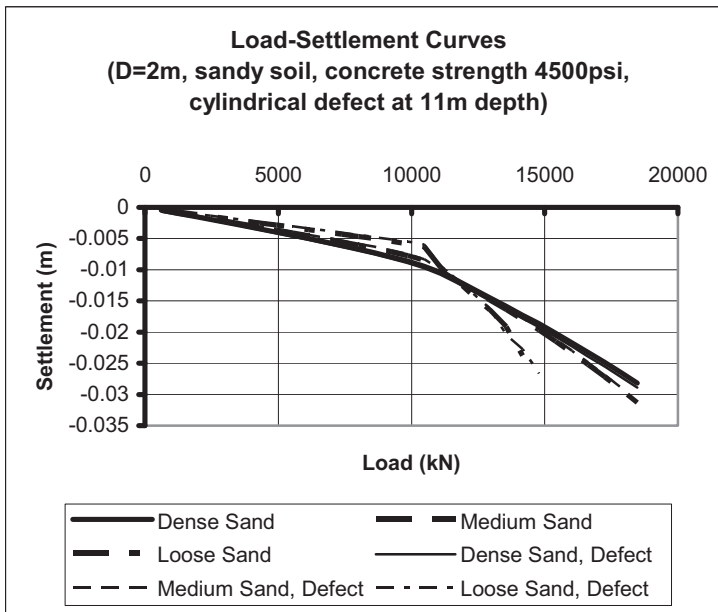


Figure 133. Load-settlement curves for drilled shafts of 2-m diameter in sand (Concrete strength 4,500 psi, 1.2-m length cylindrical anomaly at 19-m depth).

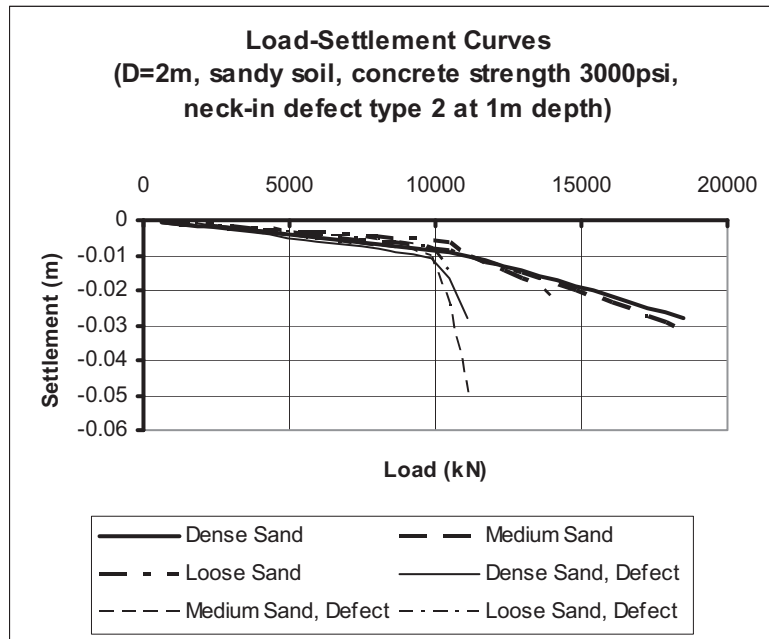


Figure 134. Load-settlement curves for drilled shafts of 2-m diameter in sand (Concrete strength 3,000 psi, 1-m length neck-in anomaly type 2 at 1-m depth).

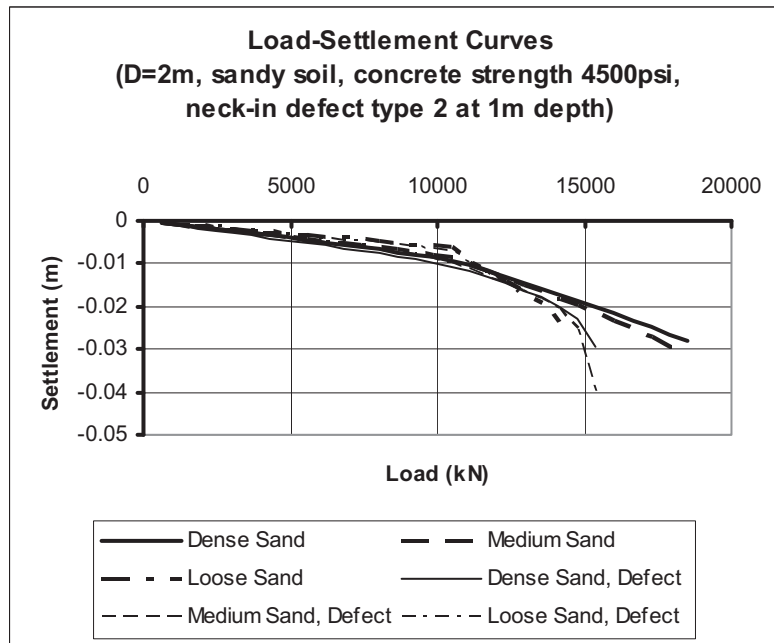


Figure 135. Load-settlement curves for drilled shafts of 2-m diameter in sand (Concrete strength 4,500 psi, 1-m length neck-in anomaly type 2 at 1-m depth).

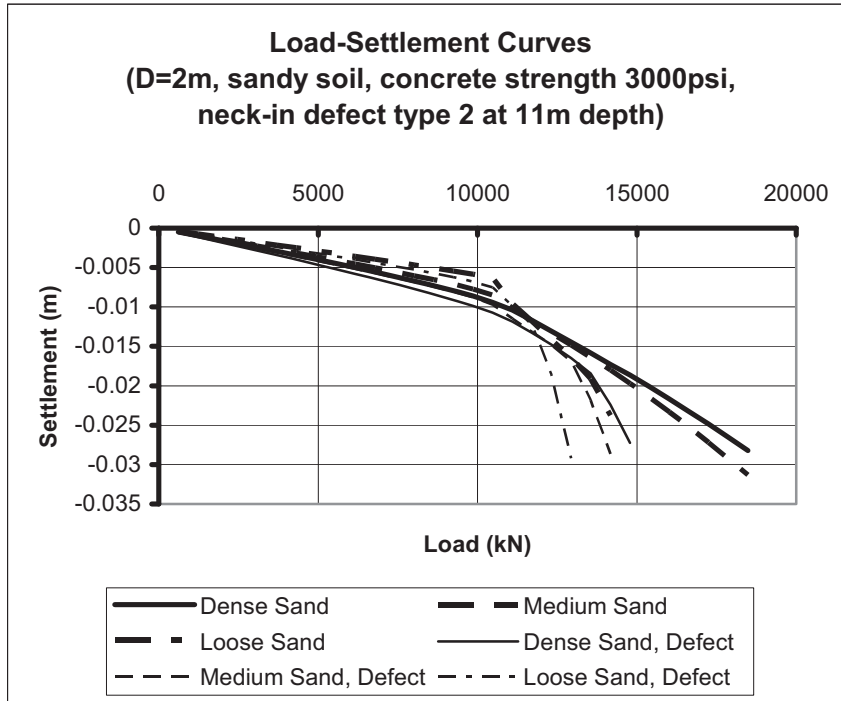


Figure 136. Load-settlement curves for drilled shafts of 2-m diameter in sand (Concrete strength 3,000 psi, 1-m length neck-in anomaly type 2 at 11-m depth).

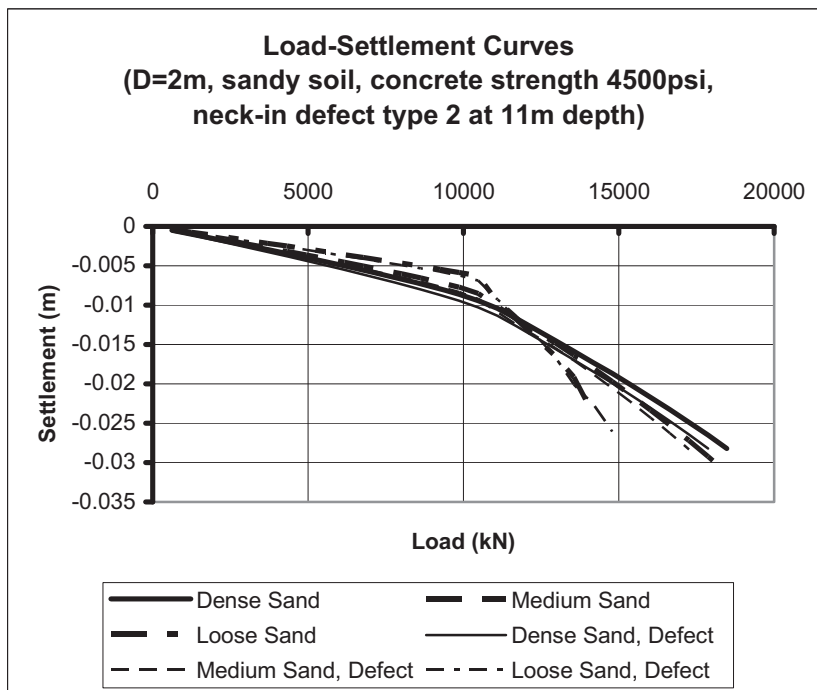


Figure 137. Load-settlement curves for drilled shafts of 2-m diameter in sand (Concrete strength 4,500 psi, 1-m length neck-in anomaly type 2 at 11-m depth).

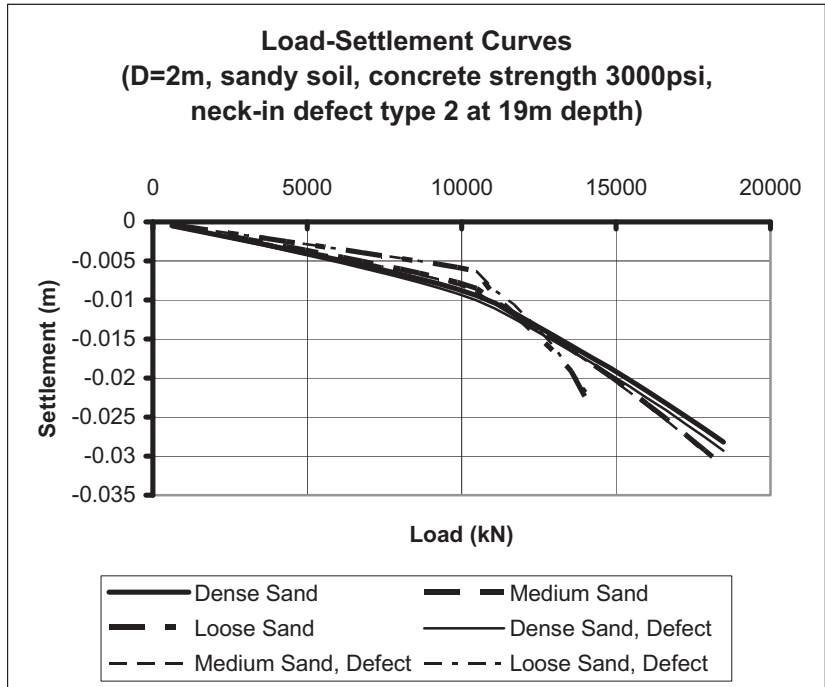


Figure 138. Load-settlement curves for drilled shafts of 2-m diameter in sand (Concrete strength 3,000 psi, 1-m length neck-in anomaly type 2 at 19-m depth).

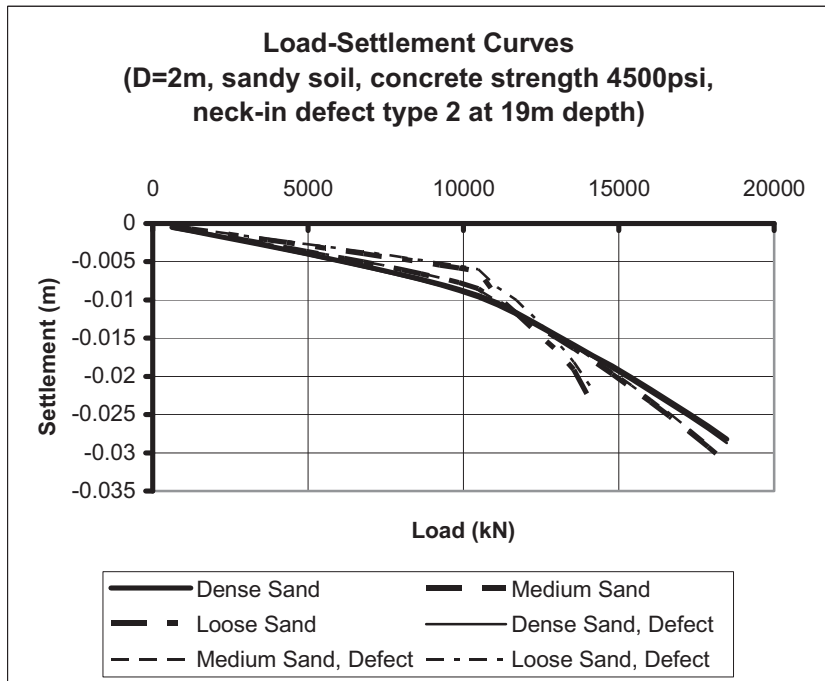


Figure 139. Load-settlement curves for drilled shafts of 2-m diameter in sand (Concrete strength 4,500 psi, 1-m length neck-in anomaly type 2 at 19-m depth).

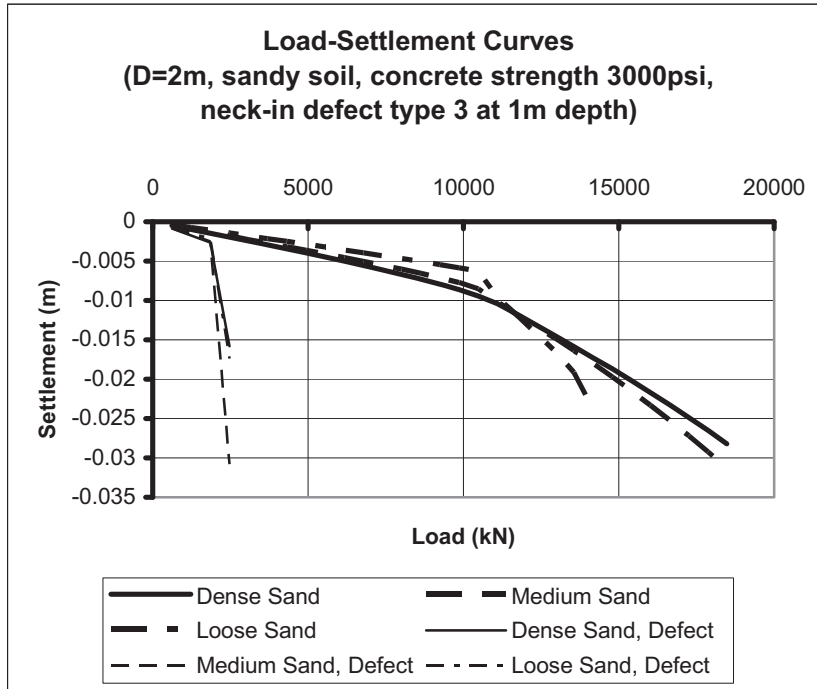


Figure 140. Load-settlement curves for drilled shafts of 2-m diameter in sand (Concrete strength 3,000 psi, 1-m length neck-in anomaly type 3 at 1-m depth).

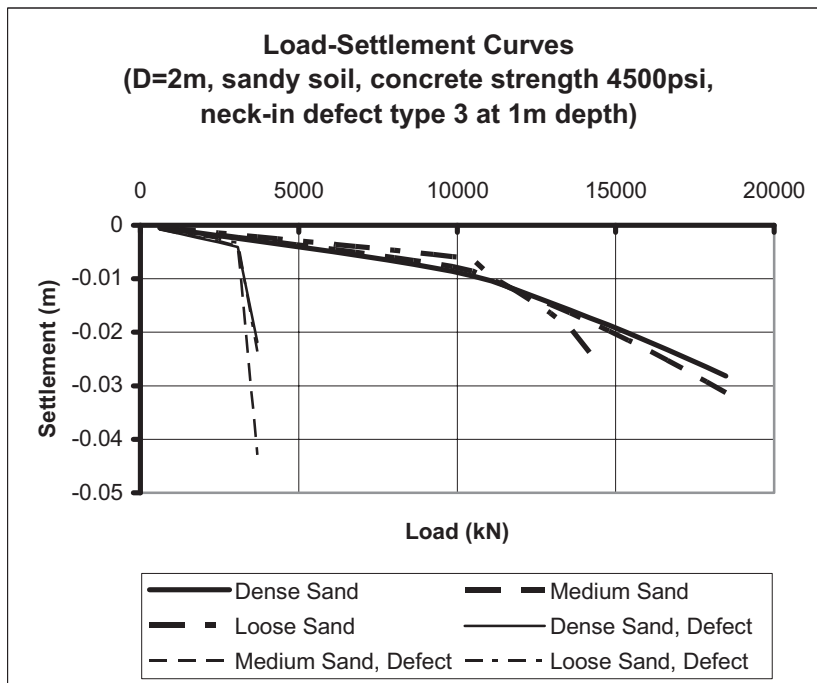


Figure 141. Load-settlement curves for drilled shafts of 2-m diameter in sand (Concrete strength 4,500 psi, 1-m length neck-in anomaly type 3 at 1-m depth).

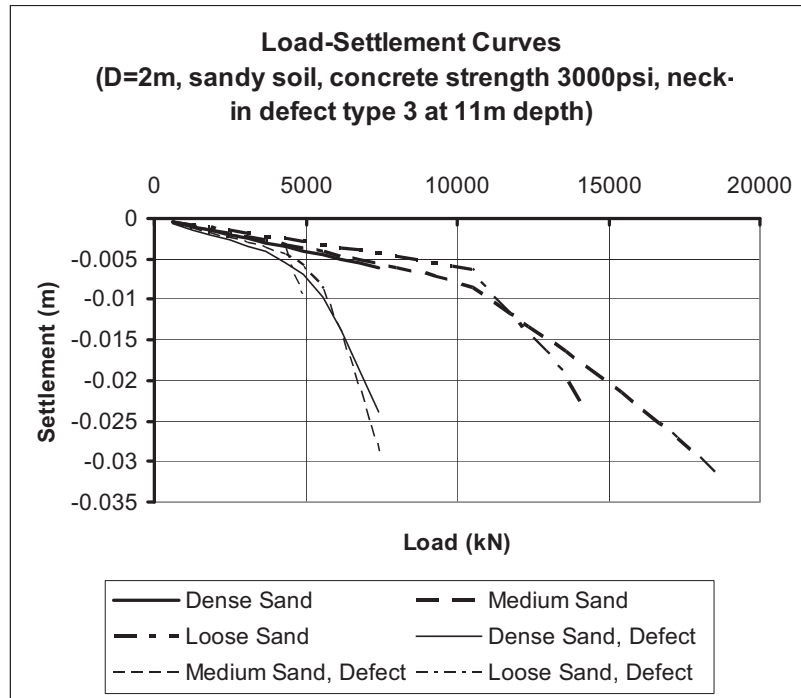


Figure 142. Load-settlement curves for drilled shafts of 2-m diameter in sand (Concrete strength 3,000 psi, 1-m length neck-in anomaly type 3 at 11-m depth).

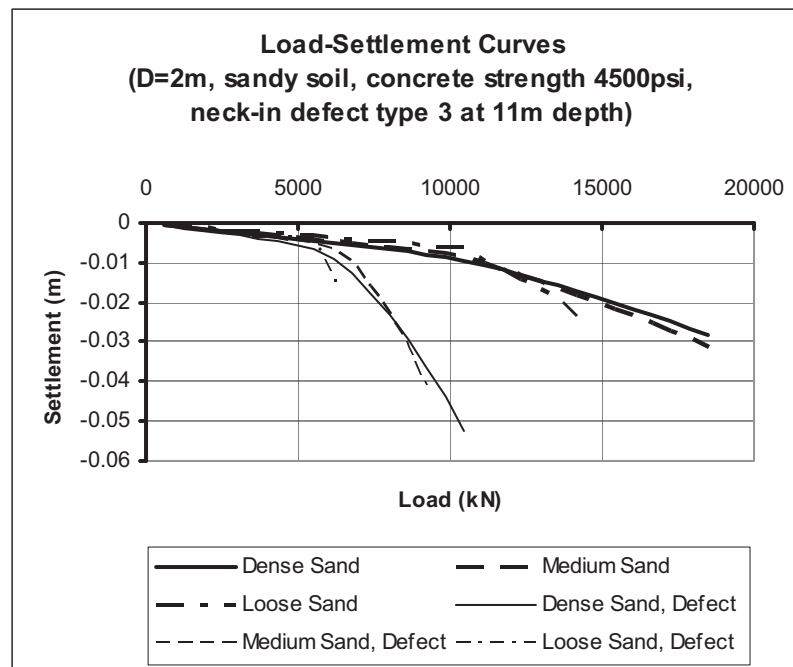


Figure 143. Load-settlement curves for drilled shafts of 2-m diameter in sand (Concrete strength 4,500 psi, 1-m length neck-in anomaly type 3 at 11-m depth).

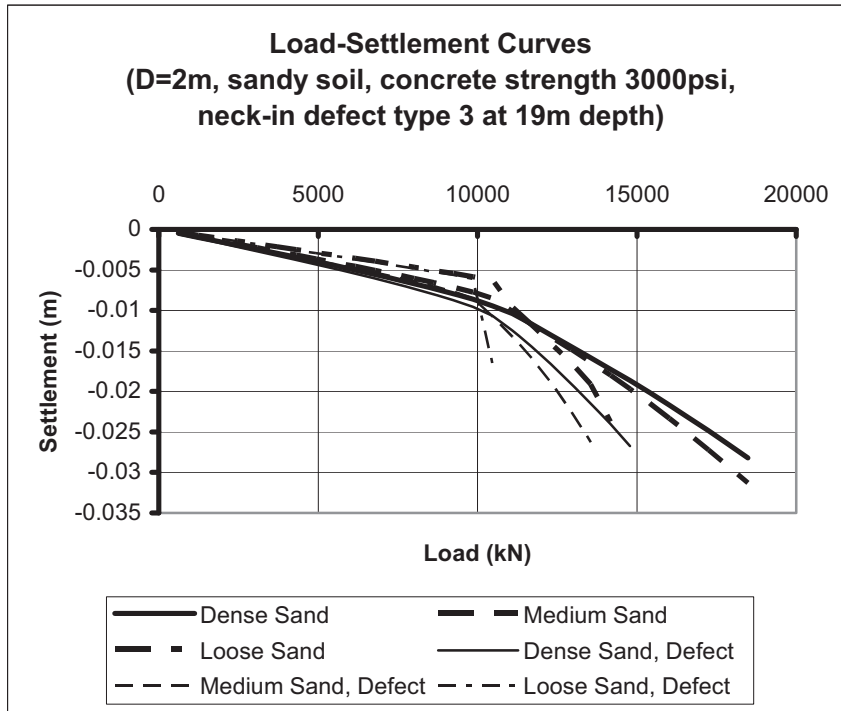


Figure 144. Load-settlement curves for drilled shafts of 2-m diameter in sand (Concrete strength 3,000 psi, 1-m length neck-in anomaly type 3 at 19-m depth).

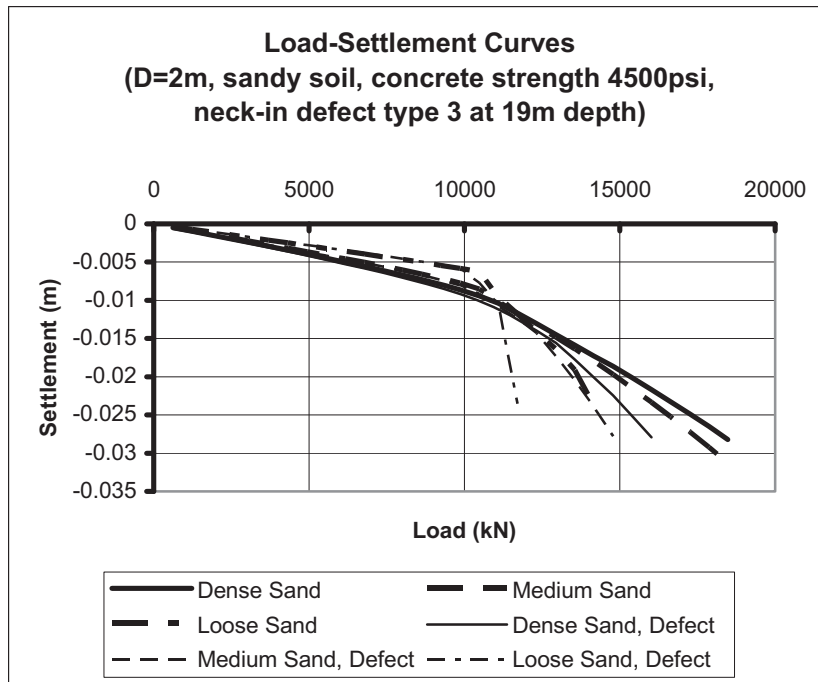


Figure 145. Load-settlement curves for drilled shafts of 2-m diameter in sand (Concrete strength 4,500 psi, 1-m length neck-in anomaly type 3 at 19-m depth).

REFERENCES

ACI 318-05 Building Code Requirements for Structural Concrete and Commentary. American Concrete Institute.

API (1993). *Recommended practice for planning, designing and constructing fixed offshore platforms Working stress design*. 20th Edition, American Petroleum Institute, Washington, DC.

Bolton M. D. (1986), *The strength and dilatancy of sands*. Geotechnique, Vol. 36, No. 1, pp 65-78

Chen, W. F., and Mizuno, E., (1990). *Nonlinear Analysis in Soil Mechanics. Theory and Implementation*. Developments in Geotechnical Engineering 53, Elsevier.

DiMaggio J. A., (2008). *Defining and Applying Quality in Drilled Deep Foundations and Earth Retaining Structures*. Keynote Address, ADSC Faculty Workshop, 2008

Desai, C. S., and Siriwardane, H. J., (1984). *Constitutive laws for engineering materials with emphasis on geologic materials*. Prentice Hall, Inc, Englewood Cliffs, New Jersey.

Duncan J.M., and Chang C.Y. (1970), *Nonlinear analysis of stress and strain in soils*. *Journal of the Soil Mechanics and Foundation Division*, ASCE, Vol. 96, pp 1629-1653.

Fahey M., and Carter J.P. (1993), *A Finite element Study of the Pressuremeter Test in Sand using a Nonlinear Elastic Plastic Model*. *Can. Geotech. J.*, Vol. 30, pp 348-362.

Guo W.D., and Randolph M.F. (1997), *Vertically Loaded Piles in Non-Homogeneous Media*. *Int. Journal for Numerical and Analytical Method in Geomechanics*, Vol. 21, pp 507-532.

Haramy K. Y. (2006), *Structural Capacity Evaluation of Drilled Shaft Foundations with Defects*, MS thesis, University of Colorado Denver.

Haramy K. Y., Chang N. Y., Rock A. (2007a), *Temperature, Velocity, Density, and Moisture in Drilled Shafts*, Proceedings, 32nd Annual Conference on Deep Foundations, Colorado Springs, CO, October, 2007, pp 473-492.

Haramy K. Y., Rock A., Chang N. Y., (2007b), [*Numerical Analysis of Load Bearing Capacity of Drilled Shafts with Defects*](#), Proceedings, 32nd Annual Conference on Deep Foundations, Colorado Springs, CO, October, 2007.

Hardin B.O., and Drnevich V.P. (1972), *Shear Modulus and Damping in Soils: Design Equation and Curves*. *Journal of the Soil Mechanics and Foundations Division*, ASCE, Vol. 98, No. SM7, pp. 667-692.

-
- Harraz A.M., Houston W.N., Walsh K.D., Perry C.R., and Houston S.L. (2005), *Comparison of Measured and Predicted Skin Friction Values for Axially Loaded Shaft Foundations in Gravelly Soils*. Advances in Deep Foundations, ASCE.
- Iskander M., Roy D., Kelly S., and Early C. (2003), *Drilled Shaft Defects: Detection, and Effects on Capacity in Varved Clay*. Journal of Geotechnical and Geoenvironmental Engineering, Vol. 129, No. 12, pp. 1128-1137.
- Jung G., Kwon, Jung S.J., and Kim (2006), *Evaluation of Full-Sized Cast-in-Place Pile Capacity with Artificial Defects*. Journal of the Transportation Research Board, No. 1975, TRB, Washington D.C.
- Kulhawy, F.H. (1991), *Drilled Shaft Foundations. Foundation Engineering*. Handbook, 2nd ed. Edited by H.Y. Fang, Van Nostrand Reinhold, New York, NY.
- MacGregor J.G., and Wight J.K. (2005), *Reinforced Concrete: Mechanics and Design*. 4th Ed., Pearson Prentice Hall, Upper Saddle River, New Jersey 07458.
- Meyerhoff G.C. (1976), *Bearing Capacity and Settlement of Pile Foundations*. Journal of the Geotechnical Engineering Division, Vol. 102, No. GT3, pp 197-228.
- O'Neill M., and Reese L.C. (1999), *Drilled Shafts: Construction Procedure and Design Methods*. Publication No. FHWA-IF-99-05.
- Mullins G., and Ashmawy A. K., *Factor Affecting Anomaly Formation in Drilled Shafts*. Final Report, FDOT, Mar. 2005.
- O'Neill M., Tabsh S.W., and Sarhan H. (2003), *Response of Drilled Shafts with Minor Flaws to Axial and Lateral Loads*. Engineering Structures, Elsevier, Vol. 25, pp 47-56.
- Petek K., Felice C.W., and Holtz R.D. (2002), *Capacity analysis of Drilled Shaft with Defects*. Geotechnical Special Publication 116, International Deep Foundations Congress, Orlando, Fla., ASCE , pp 1120-1135.
- Rollins K.M., Clayton R.J., Mikesell R.C., and Blaise B.C. (2005), *Drilled Shaft Side Friction in Gravelly Soils*. Journal of Geotechnical and Geoenvironmental Engineering, Vol. 131, No. 8, pp. 987-1003.
- Sarhan, H.A., O'Neill, M.W., and Tabsh S.W. (2004), *Structural Capacity Reduction for Drilled Shafts with Minor Flaws*. ACI Structural Journal, May-June.
- Tomlinson M.J. (2001), *Foundation Design and Construction*. 7th ed., Prentice Hall, London.
- Wightman, W.E., Jalinoos, F., Hanna, K. (2003), *Application of Geophysical Methods to Highway Related Problems*, Publication No. FHWA-IF-04-021.

